

2015-04-22

Design, Construction, and Calibration of a Vibrating Tube Densimeter for Volumetric Measurements of Acid Gas Fluids

Deering, Connor Edward

Deering, C. E. (2015). Design, Construction, and Calibration of a Vibrating Tube Densimeter for Volumetric Measurements of Acid Gas Fluids (Master's thesis, University of Calgary, Calgary, Canada). Retrieved from <https://prism.ucalgary.ca>. doi:10.11575/PRISM/25578

<http://hdl.handle.net/11023/2155>

Downloaded from PRISM Repository, University of Calgary

UNIVERSITY OF CALGARY

Design, Construction, and Calibration of a Vibrating Tube Densimeter for Volumetric
Measurements of Acid Gas Fluids

by

Connor Edward Deering

A THESIS

SUBMITTED TO THE FACULTY OF GRADUATE STUDIES
IN PARTIAL FULFILMENT OF THE REQUIREMENTS FOR THE
DEGREE OF MASTER OF SCIENCE

GRADUATE PROGRAM IN CHEMISTRY

CALGARY, ALBERTA

FEBRUARY, 2015

© Connor Edward Deering 2015

Abstract

Volumetric changes are vital to understanding the high-pressure chemical thermodynamics within acid gas injection processes. In this study, a vibrating tube densimeter was constructed and calibrated in order to perform volumetric measurements on acid gas fluids where previous literature were sparse. The densimeter uses an optically coupled feedback loop in order to maintain a fluid filled vibrating tube at its harmonic frequency. The densimeter is capable of measuring densities at temperatures between $T = 25$ and 150 °C and pressures up to $p = 35$ MPa (5076 psia).

Densities of pure carbon dioxide and water dissolved in carbon dioxide at low concentrations were measured and used to calculate partial molar volumes at temperatures between $T = 45$ and 120 °C and pressures up to $p = 35$ MPa for use in equilibrium or fugacity calculations. The Krichevskii parameter for water's influence on carbon dioxide's critical behaviour was determined using the partial molar volume measurements.

Acknowledgements

I am incredibly grateful for the opportunity and support provided by my supervisor, Dr. Robert Marriott. He was always understanding and willing to share his vast knowledge. It was easy to find inspiration in Rob's ideas and work ethic as without his advisement this thesis would not have been possible. I am glad that our relationship went beyond student-supervisor and can be equally considered a friendship.

Many thanks must go out to Senior Electronics Technician, Edward Cairns, Science Workshop Technician (CNC), Jay McIsaac, and Science Workshop Manager, Andy Read at the University of Calgary for their technical labours and expertise in designing this instrument. Without their services and knowledge in electronics and machining, the densimeter could not have been built to the standard it is at today.

I am also grateful to Dr. Yujun Shi and Dr. Simon Trudel for their continued support as members of my supervisory committee.

My appreciation goes out to Matt Saunders for his help with data collection in the laboratory during a busy 2014 summer and I wish him all the best in his future.

I would also like to recognize the help provided by the knowledgeable staff at Alberta Sulphur Research Ltd. (ASRL). In particular, Francis Bernard and Kevin Lesage for sharing their expertise in high-pressure experimental design and analytical techniques as

well as post doctoral researcher, Dr. Payman Pirzadeh, for his tireless help in refining and reviewing my written and presented works.

This thesis was also funded by several sources:

Dr. Marriott`s NSERC ASRL Industrial Research Chair in Applied Sulfur Chemistry, the University of Calgary, the Alberta Learning Information Service (ALIS) Queen Elizabeth II Scholarship Program (all 2012-2014), and ALIS Graduate Student Scholarship (2013). Through funding provided again by Dr. Marriott, the University of Calgary Travel Award, and the Faculty of Graduate Studies (FGS) Travel Award (2014) I presented my work at the 2014 International Conference of Chemical Thermodynamics (ICCT) held in Durban, South Africa.

My sincere appreciation to the late Bonnie King, Janice Crawford and the rest of the graduate program support staff along with Patricia Alegre of ASRL for their guidance on university requirements and practices.

Thanks to my parents, Lorne and Patsy, and brothers, Stephen and Joe, for their moral support and whose continual reminders of life outside of the program during weekly phone conversations preserved a positive frame-of-mind even through frustrating times.

Finally, thanks to all of my friends, both inside the university and out, for providing refreshing breaks from study in order to maintain consistent motivation and work ethic over the course of my program here at the University of Calgary.

To my parents, Lorne and Patsy

Table of Contents

Abstract	ii
Acknowledgements	iii
Dedication	v
Table of Contents	vi
List of Tables	viii
List of Figures	ix
List of Symbols, Abbreviations and Nomenclature	xii
Chapter One: Introduction	1
1.1 Outline.....	1
1.2 Natural Gas Processing and Acid Gas Injection	3
1.2.1 Typical Process Scheme for Western Canada	3
1.2.2 Using Volumetric Data to Avoid Potential Processing Problems	6
1.2.3 The Range of Acid Gas Conditions	8
1.3 Densimetry	12
1.3.1 Choice of Densimeter	12
1.3.2 Vibrating Tube Densimetry	13
Chapter Two: Vibrating Tube Densimeter Design	15
2.1 Measurement Cell	15
2.1.1 Selection of Tube for Measurement Cell	15
2.1.2 Measurement Cell Design.....	21
2.1.3 Measurement Blocks and Measurement Cell Housing	28
2.2 Interfacing the Densimeter to a Computer	32
2.2.1 LabVIEW	32
2.2.2 COM Communication and Device Controls.....	33
2.3.2 Data Collection Configuration.....	37
Chapter Three: Calibration and Measurement Procedures	39
3.1 Temperature Calibration	39
3.1.1 The International Temperature Scale of 1990	39
3.1.2 Apparatus and Materials	41

3.1.3 Primary Temperature Calibration Method.....	42
3.1.4 Secondary Temperature Calibration Method.....	43
3.1.5 Results & Discussion.....	43
3.2 Pressure Calibration.....	48
3.2.1 Deadweight Piston Gauges/Testers.....	48
3.2.2 Experimental Methods.....	50
3.2.3 Results and Discussion.....	52
3.3 Vibrating Tube Densimeter Calibration.....	56
3.4 Density Measurement.....	61
3.5 Chemicals.....	63
Chapter Four: Volumetric Measurements of Water in Carbon Dioxide.....	64
4.1 Calculation of Volumetric Properties and the Krichevskii Parameter.....	64
4.2 Results and Discussion.....	67
4.2.1 Relative Density Measurements.....	67
4.2.2 Partial Molar Volumes of Water in Carbon Dioxide.....	85
4.2.3 Krichevskii Parameter.....	92
Chapter Five: Conclusions and Future Directions.....	100
Appendix A: H₂S Synthesis.....	103
References.....	110

List of Tables

Table 1. Effect of a high-vacuum atmosphere on the stability (standard deviation, σ) of the time period of the vibrating tube's oscillation at $T = 50$ °C.....	29
Table 2. Effect of thermostating the pressure transducer electronics to $T = 26.00$ °C (± 0.05 °C) on measurement stability (A), as well as the frequency counter and signal electronics on the standard deviation of the vibrating tube's time period (B).....	31
Table 3. The experimentally measured melting points of indium (primary calibration point), H ₂ O (primary calibration point) and the benzoic acid (calibration accuracy control) with their corresponding experimental errors.	45
Table 4. Calibration equation parameters for the four PRTs.	47
Table 5. Relevant parameters for deadweight calibration.....	53
Table 6. Relevant mass and pressures for the deadweight calibration.....	53
Table 7. Relative density measurements for CO ₂ at from $T = 45$ to 120 °C and $p = 2.5$ to 35 MPa.....	68
Table 8. Relative density measurements and partial molar volumes of H ₂ O in CO ₂ from $T = 45$ to 120 °C and $p = 2.5$ to 35 MPa.....	72
Table 9. Near-critical data (approximately within 200 kg·m ⁻³ of the solvent's critical density) selected for Krichevskii parameter determination.	95
Table 10. Comparison of Krichevskii parameters for several solutes dissolved in CO ₂	99
Table 11. Concentrations of the impurities in the synthesized H ₂ S and commercial H ₂ S as measured by GC-TCD with their respective errors listed at 95% confidence.....	108

List of Figures

Figure 1. Schematic of a typical amine treatment plant where red lines represent a flow containing acid gas components, blue lines show the flow of lean aqueous amine and green lines show the flow of the sweetened gas.	4
Figure 2. Cumulative acid gas injection rates (left) and masses (right) in Western Canada between 1989 and 2003, taken from Bachu and Gunter.....	5
Figure 3. <i>In-situ</i> Western Canadian reservoir conditions where acid gas injection operations are in place: A. Temperature and pressure conditions along with the vapour lines and critical points of CO ₂ and H ₂ S; B. Injected gas composition	9
Figure 4. Available literature density data for H ₂ O - CO ₂ binary mixtures.....	11
Figure 5. Sensitivity ratio for different dimensions of 316L stainless steel tubing in 30 cm lengths.	17
Figure 6. Plot of the pressure rating against the sensitivity ratio for various sizes of stainless steel tubing.	19
Figure 7. Determining the sensitivity ratio, m_0/V_{00} , by plotting the normalized time period versus a range of densities at $T = 50$ °C.	20
Figure 8. A simplified schematic diagram of the vibrating tube densimeter.....	22
Figure 9. A computer-aided drafting (CAD) depiction of the vibrating tube densimeter measurement cell	23
Figure 10. Alignment configurations of the vibrating tube operating under case (i) where the path length of the vibration is less than the radius of the window.....	26
Figure 11. Representation of the phase and shape of drive signal (dashed line) with respect to the detector signal (solid line) and the motion of the tube (arrows) over time. 27	
Figure 12. Full LabVIEW front control panel for operating the vibrating tube densimeter:	33
Figure 13. Transducer settings tab in LabVIEW control panel.	34
Figure 14. Syringe pump “A” controls in LabVIEW panel.	36
Figure 15. Data configuration settings tab in LabVIEW panel.....	37
Figure 16. Live-update pressure plot with measurement indicators in the LabVIEW panel	38
Figure 17. Representative plot of the temperature, measured by the PRT, over time during the heating of indium past its melting point temperature (156.5985 °C).....	44

Figure 18. Primary calibration plot of the measured temperature, T_{meas} , against the accepted literature temperature, T_{lit} , in determining equation 3-1 for a PRT using the melting point of indium (156.5985 °C) and H ₂ O (0.000 °C) as reference points according to the ITS-90 guidelines.....	46
Figure 19. Secondary calibration plot for comparing the temperature measurements of three additional PRTs (T_{meas}) against the temperature measured by the primary calibrated probe (T_{cal}) between $T = 0$ °C and 155 °C.	46
Figure 20. Pressurements deadweight tester used for pressure calibration.....	51
Figure 21. Deadweight primary calibration plot of the calculated applied reference pressures (p_{corr}) between $p = 3$ MPa and 68 MPa and their corresponding transducer measurements (p_{meas}).	56
Figure 22. Pressure dependence of the calibration constant, $k_{T,p}$, with their respective linear regressions over the experimental pressure range up to $p = 35$ MPa using H ₂ O and N ₂ as the calibration fluids at different temperatures.....	58
Figure 23. Comparison of the total calibration time required for completing density measurements at temperatures of $T = 45, 50, 75, 100,$ and 125 °C for the densimeter outlined in this work assuming one hour for pressure stabilization and measurement time and four hours for thermal equilibrium to be reached after a temperature change.	60
Figure 24. Calculated density difference between 0.2839% (0.06468 mol·kg ⁻¹) H ₂ O in CO ₂ and pure CO ₂ at temperatures between $T = 50$ and 125 °C and pressures up to $p = 35$ MPa.....	65
Figure 25. Measured CO ₂ densities at experimental temperatures and pressures.	82
Figure 26. Measured densities for H ₂ O dissolved in CO ₂ at experimental temperatures and pressures.	83
Figure 27. Relative deviation plot comparing measured densities against calculated equation-of-state densities at experimental temperatures and pressures.	84
Figure 28. Partial molar volumes of H ₂ O in CO ₂ , with figure inset showing the full plot, at $T = 45.130$ °C and $m = 0.05325$ mol·kg ⁻¹	86
Figure 29. Partial molar volumes of H ₂ O in CO ₂ , with figure inset showing the full plot, at $T = 49.754$ °C and $m = 0.06468$ mol·kg ⁻¹	87
Figure 30. Partial molar volumes of H ₂ O in CO ₂ , with figure inset showing the full plot, at $T = 73.086$ °C and $m = 0.06468$ mol·kg ⁻¹	88
Figure 31. The effect of concentration on partial molar volumes of H ₂ O in CO ₂	89

Figure 32. Overlaid partial molar volumes of H ₂ O in CO ₂ for the experimental pressure range at different temperatures.	91
Figure 33. A plot of $(\partial p/\partial x_{H_2O})$ against the solvent density for H ₂ O in CO ₂ using all of the data in this work and literature data below concentrations of $x_{H_2O} = 0.2$	93
Figure 34. Plot of the $(\partial p/\partial x_{H_2O})$ derivatives against their corresponding pure CO ₂ densities near the critical density to determine the Krichevskii parameter.	97
Figure 35. Simplified schematic of the reaction apparatus for the generation of H ₂ S...	105
Figure 36. Comparison of contaminants in the synthesized H ₂ S and the commercial H ₂ S with their respective 95% confidence intervals as measured by GC-TCD.....	109

List of Symbols, Abbreviations and Nomenclature

Symbol	Definition
$2A$	Peak-to-peak amplitude of the tube vibration
A	Slope of the temperature calibration
a_0	Effective area of the piston at ambient pressure and reference temperature
A_{cs}	Cross-sectional area
A_e	Constant temperature effective area
A_{Kr}	Krichevskii parameter
A_p	Temperature-corrected true effective area
$A_{T,p}$	Linear density equation slope
B	Intercept of the temperature calibration
b_d	Pressure distortion coefficient
$B_{T,p}$	Linear density equation intercept
CAD	Computer-assisted drafting
CG	Copper gasket
CH ₄	Methane
CO ₂	Carbon dioxide
COM	Data communication line
COS	Carbonyl Sulfide
DC	Electromagnetic drive coil
DLC	Data logging computer
E	Young`s Modulus
F	Force
FC	Frequency counter
f_i	Fugacity of species i
FO	Fiber optic cables
F_z	Force of the cantilever vibration
g	Gravitational constant
GC	Gas chromatography

g_l	Local gravitational constant
h	Thickness of a vibrating cantilever
H ₂ S	Hydrogen sulfide
HCl	Hydrochloric acid
ID	Inner diameter
IT	Iron tab
ITS-90	International Temperature Scale of 1990
IV	Inlet valve
K	Equilibrium constant
k	Spring constant of the vibrating tube
K_{pi}	Equilibrium constant at pressure $p = p_i$
$k_{T,p}$	Calibration constant of vibrating tube densimeter
k_z	Cantilever spring constant
L	Length of a vibrating cantilever
LED	Light emitting diode
LS	Light emitting diode source
m	Molality
m_0	Mass of the vibrating tube while evacuated
MB1	First measurement block
MB2	Second measurement block
M_i	Molar mass of species i
m_i	Masses used in deadweight pressure calibration
m_{t+f}	Mass of vibrating tube and fluid contained within
N ₂	Nitrogen
Na ₂ S·9H ₂ O	Sodium sulfide nonahydrate
n_i	Moles of species i
NIST	National Institute of Standards and Technology
OD	Outer diameter
OS	Oscilloscope
OV	Outlet valve

p	Pressure
P_2O_5	Phosphorus pentoxide
p_{corr}	Corrected deadweight pressure
PD	Photodiode detector and signal electronics
PRT	Platinum resistance thermometer
PT	Pressure transducer
R	Gas constant
r	Radius of the fiber optic pickup window
REFPROP	Reference Fluid Thermodynamic and Transport Properties software
S_{00}	Geometric sensitivity factor
$SmCo_5$	Samarium-cobalt magnet
SP	High-pressure syringe pump
T	Temperature
t	Time
T_{cal}	Measured reference temperature from a calibrated thermometer
TCD	Thermal conductivity detector
T_{lit}	Literature phase transition reference temperature
T_{meas}	Measured reference temperature
TZ	Temperature controlled zone
UT	Vibrating U-tube (measurement cell)
V	Total volume
V_{00}	Inner volume of the vibrating tube at reference conditions
VC	High-vacuum chamber
VF	DN63 conflat vacuum flanges
\bar{V}	Total molar volume
\bar{V}_2^∞	Partial molar volume of solute at infinite dilution
\bar{V}_i	Partial molar volume of species i
$\bar{V}_{\phi,i}$	Apparent molar volume of species i
w	Width of a vibrating cantilever
x_i	Mole fraction of species i

z	Vertical displacement at the end of a vibrating cantilever
α_c	Coefficient of thermal expansion for the cylinder
α_p	Coefficient of thermal expansion for the piston
α_V	Temperature response coefficient of the tube volume
β_V	Pressure response coefficient of the tube volume
β_τ	Pressure response coefficient of the spring constant
δ	Denotes error of a variable
Δh	Height difference between transducer and deadweight piston
δ_m	Direct measurement error
$\Delta_r \bar{V}$	Molar volume change of the reaction
δ_{TP}	Error caused by temperature and pressure deviations
ε_{τ_1}	Linear temperature response coefficient
ε_{τ_2}	Quadratic temperature response coefficient
$\kappa_{T,1}$	Isothermal compressibility of the solvent
ρ	Density
ρ^*	Density of pure solvent
ρ_{air}	Density of air
ρ_c	Critical point density
ρ_{EOS}	Density calculated by an equation-of-state
ρ_{fluid}	Density of deadweight hydraulic fluid
ρ_i	Density of mixture containing solute i
ρ_m	Density of the vibrating tube material
ρ_{mass}	Density of deadweight masses
ρ_{ref}	Density of reference fluid
σ	Standard deviation
τ	Time period of the vibrating tube's oscillation
τ_0	Time period of the vibrating tube's oscillation with reference fluid
τ_{00}	Time period of evacuated tube's oscillation at reference temperature
τ_{ref}	Time period of the vibrating tube's oscillation with reference fluid
ν_i	Stoichiometric coefficient of species i

Chapter One: Introduction

1.1 Outline

Any system at equilibrium has intrinsic thermodynamic properties that can be measured and studied in order to understand (i) its chemical behaviour and (ii) any deviations resulting from changes in the temperature, pressure, or composition. In many cases, it is much more efficient to determine thermodynamic relationships using core thermodynamic properties versus measuring each possible perturbation to a chemical system. The goal of this thesis was to design, construct and calibrate an instrument to collect data for characterizing the volumetric properties in high-pressure acid gas fluid systems. The instrument designed was a vibrating tube densimeter which will be used to measure the density differences between acid gas mixtures and their pure components. Initial studies reported here have involved comparing pure carbon dioxide (CO_2) to water (H_2O) dissolved in CO_2 near infinite dilution, where the change in partial molar volume provides the pressure dependence for equilibrium.

The thesis has been organized into five chapters. The first chapter introduces the underlying scientific fundamentals and concepts behind the research and goals to be accomplished in the scope of this study.

The second chapter presents the design and construction of the vibrating tube densimeter, the instrument later used to collect experimental data. The measurement cell containing the vibrating tube is described in detail along with the measurement cell housing and the

interfacing LabVIEW software code used for control and performance monitoring. All measurement devices and their specifications are listed in chapter two.

The third chapter discusses the calibration and measurement procedures required for obtaining relative density data with the densimeter. Also, the vital calibration procedures for the pressure transducer and platinum resistance thermometers (PRTs) were provided in this chapter.

The fourth chapter presents the density measurements of pure CO₂ and dilute mixtures of H₂O dissolved in CO₂. These measurements were then extended to the calculation of apparent and partial molar volumes at infinite dilution and, further on, to the determination of the Krichevskii parameter in order to describe the volumetric properties and critical-region behaviour of the H₂O - CO₂ system at low H₂O concentrations.

Finally, the fifth chapter summarizes the trends and insights observed in the measured densities and the calculated thermodynamic parameters. Potential future research directions such as improvements to the instrument design and future volumetric studies that could be undertaken with the vibrating tube densimeter are suggested in concluding this chapter.

1.2 Natural Gas Processing and Acid Gas Injection

1.2.1 Typical Process Scheme for Western Canada

Natural gas has played a significant role in the world energy market for a number of years and continues to rise in demand.¹ A considerable amount of the known natural gas reserves worldwide contain what is characterized as sour gas. A sour gas refers to a natural gas stream that contains CO₂ and/or hydrogen sulfide (H₂S) impurities. The concentration of the sour species in gas reservoirs varies widely between reservoirs, but must be reduced before the natural gas is moved downstream for sale. Regulatory bodies mandate strict specifications for sales gas which must be met by the gas producer; typically about 2% and 23 mg·m⁻³ (2 ppm) for CO₂ and H₂S respectively in North America.² The removal of the sour components is commonly completed in gas treatment facilities using an amine sweetening technique (schematically shown in Figure 1), where sour gas is passed into large contactors charged with counter-flowing aqueous amine. The amine selectively absorbs the sour components while allowing the remaining hydrocarbons to pass through to the sales stream after dehydration. The removed CO₂ and H₂S are significantly more concentrated after being removed from the hydrocarbons and is collectively referred to as acid gas.

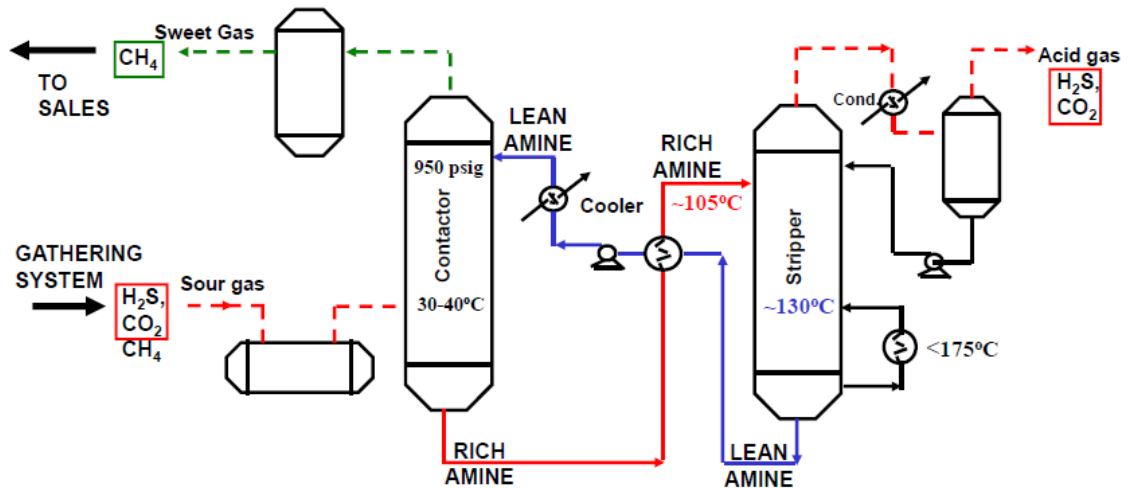


Figure 1. Schematic of a typical amine treatment plant where red lines represent a flow containing acid gas components, blue lines show the flow of lean aqueous amine and green lines show the flow of the sweetened gas.³

The absorbed acid gas and amine, rich amine, then flows through a regeneration stripper where the acid gas is boiled off at temperatures up to $T = 130\text{ }^{\circ}\text{C}$.³ The lean amine is recycled back into the acid gas contactor, while the removed acid gas is prepared for sulfur recovery or acid gas injection. Depending on the initial reservoir conditions and selectivity of the amine being used, the removed acid gas composition is often between 90% CO_2 to 80% H_2S in Western Canada.⁶ Also, because the amine is an aqueous solution, the acid gas is saturated with H_2O .

Dealing with the removed acid gas fluids in a safe and economical manner requires consideration of the gas composition, volumes, local regulations, capital costs, and operational costs. There are a number of options for producers handling acid gas fluids including sulfur recovery units (conversion to elemental sulfur), acid gas flaring, acid gas injection or some combination thereof.^{3,4,5} Acid gas injection has been increasingly

utilized as a sulfur and carbon management technique in Western Canada since its introduction in 1989, increasing from four active injection sites in 1994 to 25 sites in 1998,⁵ and up to 46 within most recent survey in 2011.^{6,7} Not surprisingly, both the total amount of acid gas injected and the rate of injection have increased significantly over this time as shown in Figure 2.5

With an acid gas compression scheme, the final sand-face (well-bottom) pressure of an injection well must match or exceed the *in-situ* reservoir pressure while taking into account the static head pressure and frictional pressure losses that occur in transport of the acid gas into the reservoir. Typical *in-situ* pressures range from $p = 5$ to 30 MPa in the Western Canadian acid gas injection wells, as shown in Figure 3A. The removed acid gas from an amine plant is typically just above atmospheric pressure, meaning compressors are needed to pressurize the fluid to an injectable level for storage.

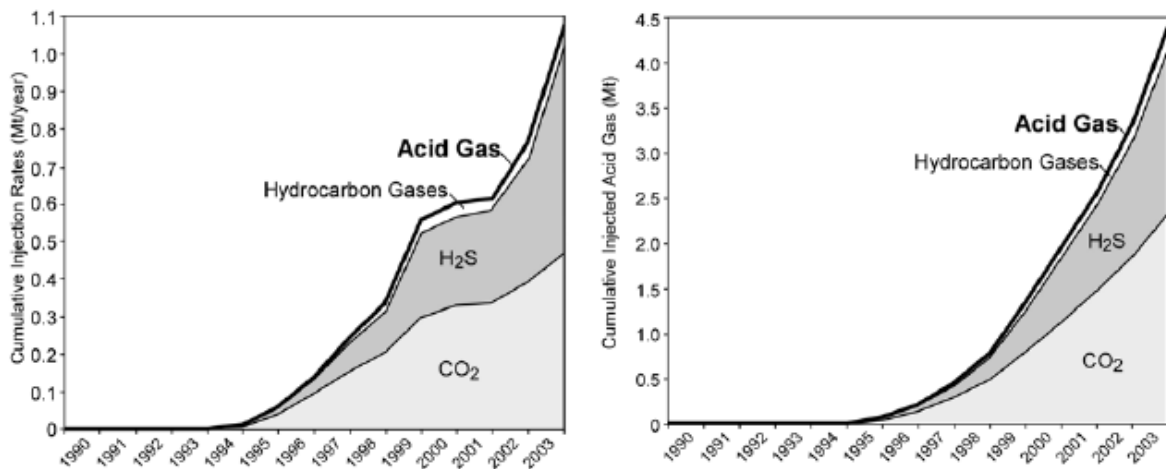


Figure 2. Cumulative acid gas injection rates (left) and masses (right) in Western Canada between 1989 and 2003, taken from Bachu and Gunter.⁵

1.2.2 Using Volumetric Data to Avoid Potential Processing Problems

With acid gas fluids experiencing such diverse conditions following their separation from the sweetened gas, it becomes very important to understand their behaviour over a wide range of temperatures and pressures. For example, the CO₂, H₂S and H₂O present in an acid gas stream will produce some amount of carbonyl sulfide (COS) through the condensation reaction (commonly referred to as a reverse hydrolysis) equilibrium:



Compositional changes can occur as the stream cools down or reaches larger pressures. These chemical changes need to be understood before the fluid comes into contact with the reservoir. As injection into a reservoir proceeds over time, the composition and pressure within the reservoir will change, potentially affecting the solubility of minerals in the surrounding geological formation. Therefore, knowledge of chemical acid gas equilibria across the operational conditions allows for an increased understanding of what will occur in the reservoir leading to optimized production.

An equilibrium constant, K , has a dependence on both the temperature and pressure of the system. While the temperature dependence of K can be experimentally determined using heat capacity and enthalpy changes, the pressure dependence is determined through the change in partial molar volume, $\Delta_r \bar{V}$:⁵⁷

$$\ln K_{p_2} - \ln K_{p_1} = -\frac{1}{RT} \int_{p_1}^{p_2} \Delta_r \bar{V} dp, \quad (1-2)$$

where $\Delta_r \bar{V}$ is the sum of each chemical species' partial molar volume, \bar{V}_i , with their stoichiometric coefficients, ν_i :

$$\Delta_r \bar{V} = \sum_i \nu_i \bar{V}_i ; \quad (1-3)$$

For the COS hydrolysis example, the change in equilibrium constant would be

$$\ln K_{p_2} - \ln K_{p_1} = -\frac{1}{RT} \left(\int_{p_1}^{p_2} \bar{V}_{CO_2} dp + \int_{p_1}^{p_2} \bar{V}_{H_2S} dp - \int_{p_1}^{p_2} \bar{V}_{COS} dp - \int_{p_1}^{p_2} \bar{V}_{H_2O} dp \right), \quad (1-4)$$

with similar equations resulting from any equilibria involving surrounding reservoir minerals. The partial molar volumes needed for equilibrium calculations involving fluids are readily obtained through the density measurements of the mixture containing solute i , ρ_i , and pure solvent, ρ^* , by using the apparent molar volume, $\bar{V}_{\phi,i}$:

$$\bar{V}_i = n_i \left(\frac{\partial \bar{V}_{\phi,i}}{\partial n_i} \right)_{T,p,n_j} + \bar{V}_{\phi,i}, \quad (1-5)$$

where:

$$\bar{V}_{\phi,i} = \frac{M_i}{\rho_i} - \frac{1000(\rho_i - \rho^*)}{m\rho_i\rho^*}. \quad (1-6)$$

The calculation of partial molar volumes from the density measurements are straightforward at infinite dilution as n_i in equation 1-5 approximates zero and the partial molar volume equals the apparent molar volume. This will be discussed in more detail in chapter 4 of this thesis.

The above equilibrium can also be described using a fugacity based model for more complex mixtures involving multiple phases. When the components of two phases are in equilibrium, the fugacities of each component, f_i' and f_i'' , must be equal. A component's fugacity at some higher pressure, p_2 , can be determined from the pressure dependence of

the partial molar volume and knowledge of the components fugacity at some lower reference pressure, p_i :⁵⁷

$$\int_{p_1}^{p_2} V_i dp = RT \ln \left(\frac{f_{i,p_2}}{f_{i,p_1}} \right). \quad (1-7)$$

In the context of acid gas injection, knowledge of the acid gas' phase behaviour is also extremely important. Not only could a saturated H₂O phase lead to hydrate formation and pipeline flow assurance issues, but could also accelerate pipeline corrosion.⁵ Thus, the dew-point of H₂O and/or hydrate must be well-defined to optimally dehydrate the acid gas stream for transportation to the injection well. The dew-point calculation requires the fugacity of H₂O in the acid gas phase which can be obtained through volumetric measurements.

1.2.3 The Range of Acid Gas Conditions

As shown in Figure 3, there is a wide range of reservoir conditions for acid gas injection sites, even when only considering Western Canadian operations. Reservoir temperatures are between $T = 30$ °C and 110 °C with acid gas fluids experiencing temperatures up to $T = 130$ °C in the amine regeneration process.³

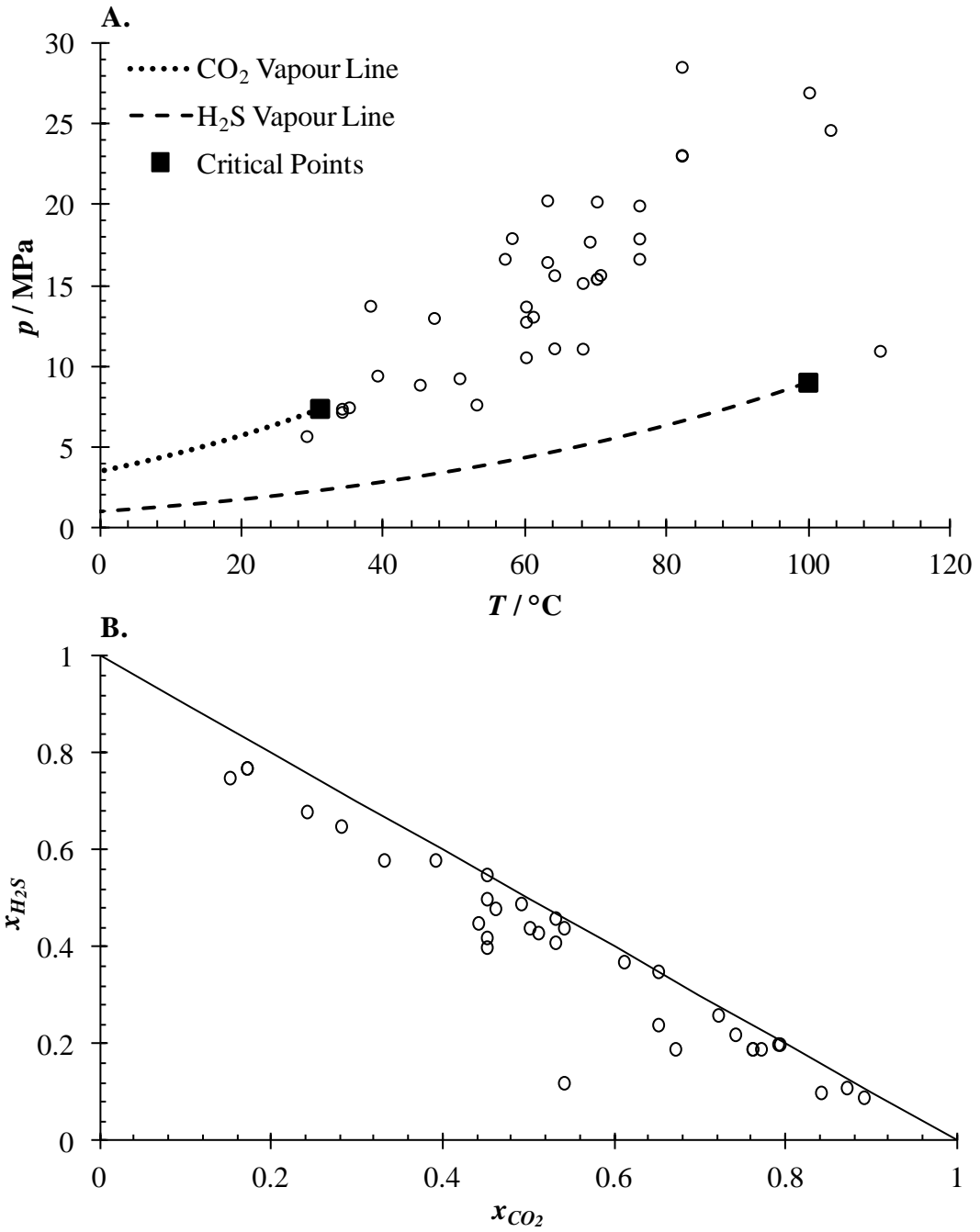


Figure 3. *In-situ* Western Canadian reservoir conditions⁶ where acid gas injection operations are in place: A. Temperature and pressure conditions along with the vapour lines and critical points of CO₂⁸ and H₂S⁹; B. Injected gas composition with the solid line representing an acid gas entirely made up of CO₂ and H₂S.

Across Western Canada, reservoirs can have a wide range of pressures ($p < 35$ MPa), and compositions anywhere between 90% CO₂ to 80% H₂S. Considering the diverse conditions for acid gas disposal, a large data set is required to comprehensively understand the behaviour. Density measurements available in literature for the H₂O – CO₂ binary mixtures are predominantly focused on the H₂O rich phase ($x_{H_2O} > 0.5$) as shown in Figure 4, with a few other datasets existing at temperatures below $T = 40$ °C at low CO₂ concentrations.^{10,11,12} The only available CO₂ rich measurements were made by Fenghour and Wakeham (1996)²⁰ and Seitz and Blencoe (1999)²⁵ at $T > 200$ °C; Zawisza and Malesińska (1981),¹³ who looked at total molar volumes at $p < 3.5$ MPa and $T = 100$ and 200 °C in mixtures between $x_{H_2O} = 0.12$ to 0.93 ; and Zhang (2002),¹⁴ who measured densities for low H₂O concentrations at $T = 35$ °C and $p < 15$ MPa. There remains a large region below $T = 200$ °C and above $p = 3.5$ MPa needing experimental volumetric measurements where H₂O is sparingly soluble in CO₂.

Considering other acid gas mixtures with CO₂, there are a limited number of density measurements reported for binary mixtures of CO₂ with H₂S and for CO₂ and COS.^{15,25} With acid gases often experiencing temperatures from ambient up to $T = 130$ °C and pressures up to $p = 35$ MPa (5076 psia) at various compositions, there is a large body of work to be completed with immediate and practical applications. This work focuses on CO₂ mixtures with low H₂O concentrations ($x_{H_2O} < 0.01$) at temperatures between $T = 45$ and 120 °C and pressures up to $p = 35$ MPa.

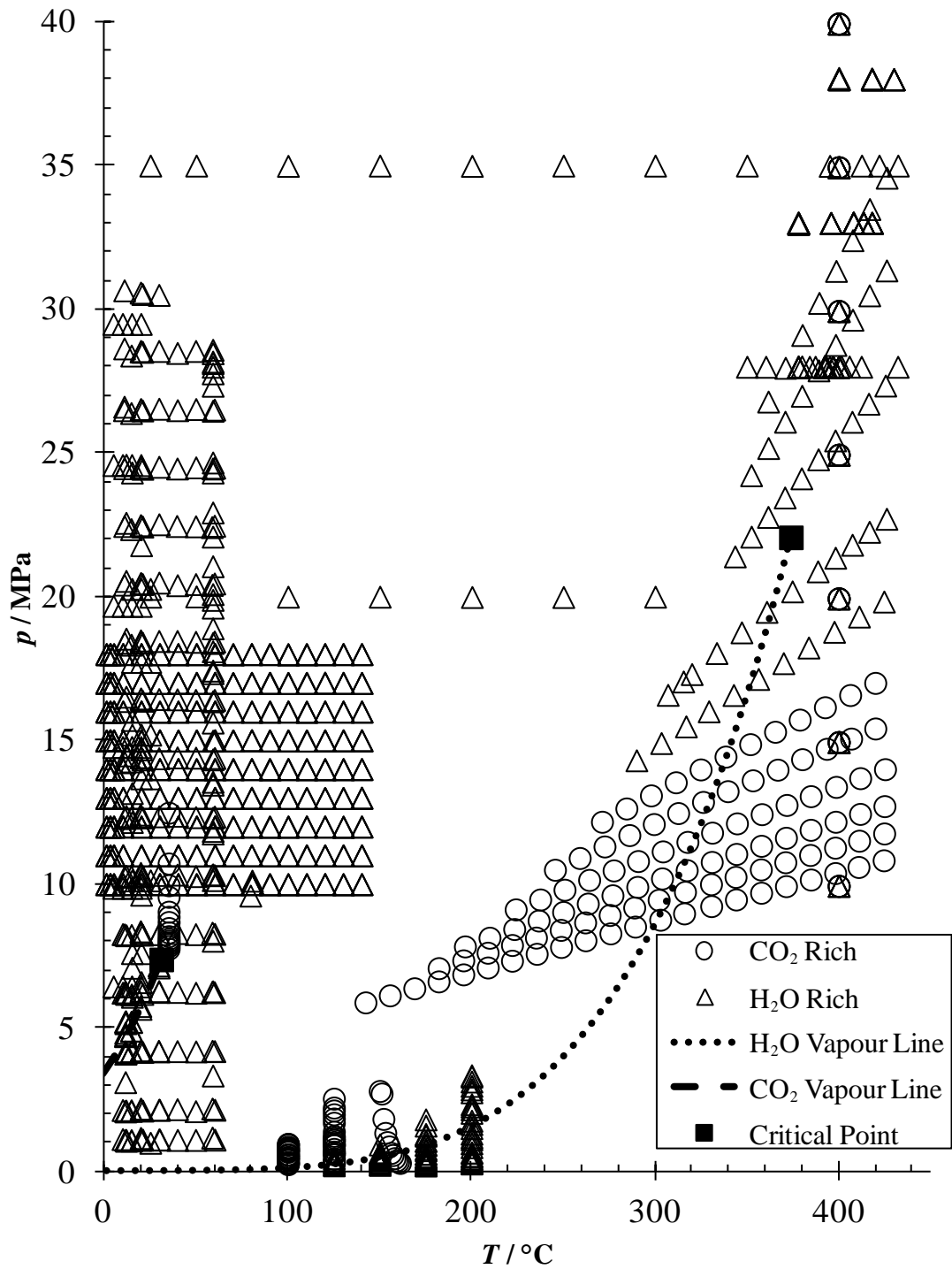


Figure 4. Available literature density data for H₂O - CO₂ binary mixtures.
8,13,14,16,17,18,19,20,21,22,23,24,25,36

1.3 Densimetry

1.3.1 Choice of Densimeter

There are several common techniques commonly used to measure densities of fluids at pressures up to $p = 35$ MPa and temperatures up to $T = 150$ °C: (1) magnetically coupled hydrostatic balances (sinker methods), (2) isochoric methods, and (3) vibrating tube densimetry. The toxicity and corrosive nature of acid gas fluids would prompt one to favour instruments with low-volume and rapid measurement.

Although known to produce accurate measurements,²⁶ sinker type densimeters are not ideal when working with acid gas fluids. There are several internal working parts (*i.e.*, the magnet attached to the float) in sinker densimeters, increasing the type of materials which must come into contact with sample fluids and adding to potential corrosion considerations. Also, different floats may need to be used if a large density range is to be studied, as would be the case for acid gas fluids over the conditions discussed in sub-section 1.2.3. Thus an operator would need to safely purge the toxic gases from within the instrument during the experiment. This can be a lengthy, hazardous process and should be performed as seldom as possible.

Isochoric density measurements are suitable for working with acid gas fluids;^{15,20} however isothermal measurements aren't readily made for determining the pressure dependence of volumetric properties (see sub-sections 1.2.2 and 4.1).

A vibrating tube densimeter allows for the fast measurement of acid gas fluids in comparison to the two previously mentioned methods. Also, vibrating tube densimeters are able to operate across the desired pressure and temperature range mentioned above and can be easily designed with corrosion-resistant materials. Finally, the volume of fluid required for density measurements in a vibrating tube densimeter is much less than that needed for a sinker or isochoric densimeter which can require tens or even hundreds of cubic centimeters of sample fluid. This presents safety concerns considering the toxic nature of acid gas species (*i.e.*, H₂S). Due to these features, a vibrating tube densimeter has been chosen as the instrument completing the volumetric measurements in this work.

1.3.2 Vibrating Tube Densimetry

The initial design of a vibrating tube to measure densities was developed by Kratky *et al.*²⁷ in 1969 for use by Anton Paar, who still sell commercial vibrating tube densimeters to this day. Picker *et al.*²⁸ improved on this design in 1974, providing the basis for future models. Vibrating tube densimeters operate based on the mechanical oscillations of a hollow “U” or “V” shaped tube that can be filled with sample fluid. In principle, the vibrating tube acts as a simple harmonic oscillator. The total mass of the tube and the fluid, m_{t+f} , contained within can be related to the time period of the tube’s oscillation, τ , through the tube’s spring constant, k , using an extension of Hooke’s law to give

$$\sqrt{\frac{k}{m_{t+f}}} = \frac{2\pi}{\tau}. \quad (1-8)$$

Assuming that the tube volume is constant, the square of the time period is then directly proportional to the density of the fluid, ρ , contained in the vibrating tube. However, the fluid density cannot be directly obtained from the time period measurement without being related to a reference density first. This is done using the classic relative density equation.^{29,30,31,48}

$$\rho - \rho_{\text{ref}} = k_{T,p} (\tau^2 - \tau_{\text{ref}}^2), \quad (1-9)$$

The calibration constant, $k_{T,p}$, incorporates physical parameters of the vibrating tube such as the spring constant of the vibrating tube, the mass of the empty tube, and the inner volume of the tube. While the assumption of a constant tube mass is fair, assuming a constant inner tube volume is certainly not robust, as one can expect expansion of the volume at higher temperatures and pressures.³² This can be accounted for by measuring the calibration constant at each experimental temperature and pressure.

The calibration constant for a particular temperature and pressure can be obtained by measuring the time period of the vibrating tube's oscillation for two different reference fluids with well-known densities at that condition. Using a calibrated tube, the time period of the sample fluid and the time period of a reference fluid, the unknown density of that sample fluid at the temperature and pressure can be determined. The calibration and measurement procedures are described in sections 3.3 and 3.4, respectively.

Chapter Two: Vibrating Tube Densimeter Design

2.1 Measurement Cell

Many acid gas contaminants (*i.e.*, water) have limited solubility; therefore, this densimeter is aimed at high-sensitivity measurements. Commercially available vibrating tube densimeters that operate at high-pressures have internal volumes of approximately 2 cm³, with a measurement error of $\pm 0.1 \text{ kg}\cdot\text{m}^{-3}$ at best, and temperature control to $\pm 0.05 \text{ }^\circ\text{C}$.⁵² These specifications can be improved upon through the tailored design and in-house construction of a novel vibrating tube densimeter to achieve the precision desired for measuring the small density differences in acid gas fluids, described later in Chapter 4.

2.1.1 Selection of Tube for Measurement Cell

The material properties of the vibrating tube chosen for the densimeter are important because they relate to the sensitivity and operating pressure of the instrument. The sensitivity can be estimated using the density of the vibrating tube material, ρ_m , tube radius, and wall thickness to calculate the inner volume and mass of the tube as described by May *et al.*³² whose extended vibrating tube density model is based on seven physical parameters: (1) the geometric sensitivity factor, S_{00} ; (2) time period of evacuated tube's oscillation at reference temperature, τ_{00} ; (3) linear temperature response coefficient, ε_{τ_1} ; (4) quadratic temperature response coefficient, ε_{τ_2} ; (5) pressure response coefficient of the spring constant, β_τ ; (6) temperature response coefficient of the tube volume, α_V ; and (7) pressure response coefficient of the tube volume, β_V :

$$\rho = \frac{(\rho_m / S_{00})}{(1 + \alpha_v T + \beta_v p)} \left(\left(\frac{\tau}{\tau_{00}(1 + \varepsilon_{\tau 1} T + \varepsilon_{\tau 2} T^2)} \right)^2 (1 + \beta_{\tau} p) - 1 \right). \quad (2-1)$$

As shown in equation 2-1, the density, ρ , is related to the time period of the tube's oscillation, τ , through a number of temperature and pressure dependant variables in addition to the sensitivity ratio, ρ_m / S_{00} , which also is equivalent to m_0 / V_{00} , where m_0 is the mass of the evacuated tube and V_{00} is the inner tube volume under reference conditions. This ρ_m / S_{00} ratio is calculated *via* the slope of a time period-density plot. A smaller slope shows a larger difference in the time period's response for a given density change making for a more sensitive instrument. Figure 5 compares the sensitivity ratios for various 316L stainless steel tube dimensions^{32,33} and shows that 0.635 cm outer diameter (OD) tubing can provide the best sensitivities. Larger outer tubing diameters provide better sensitivities, because, although there is an increased mass, the internal volume gain is much larger and more fluid is present for each measurement.

Since this densimeter is also being designed for highly toxic fluids, the volume must be kept to a minimum as a safety precaution. In this regard, the volume per unit length of a 0.635 cm OD by 0.229 cm inner diameter (ID) tube is *ca.* 18 times greater than the volume of a 0.159 cm OD by 0.054 cm ID tube even though both have similar sensitivity ratios/pressure ratings of 1.2 g·mL⁻¹/35.1 MPa and 1.7 g·mL⁻¹/38.6 MPa, respectively.

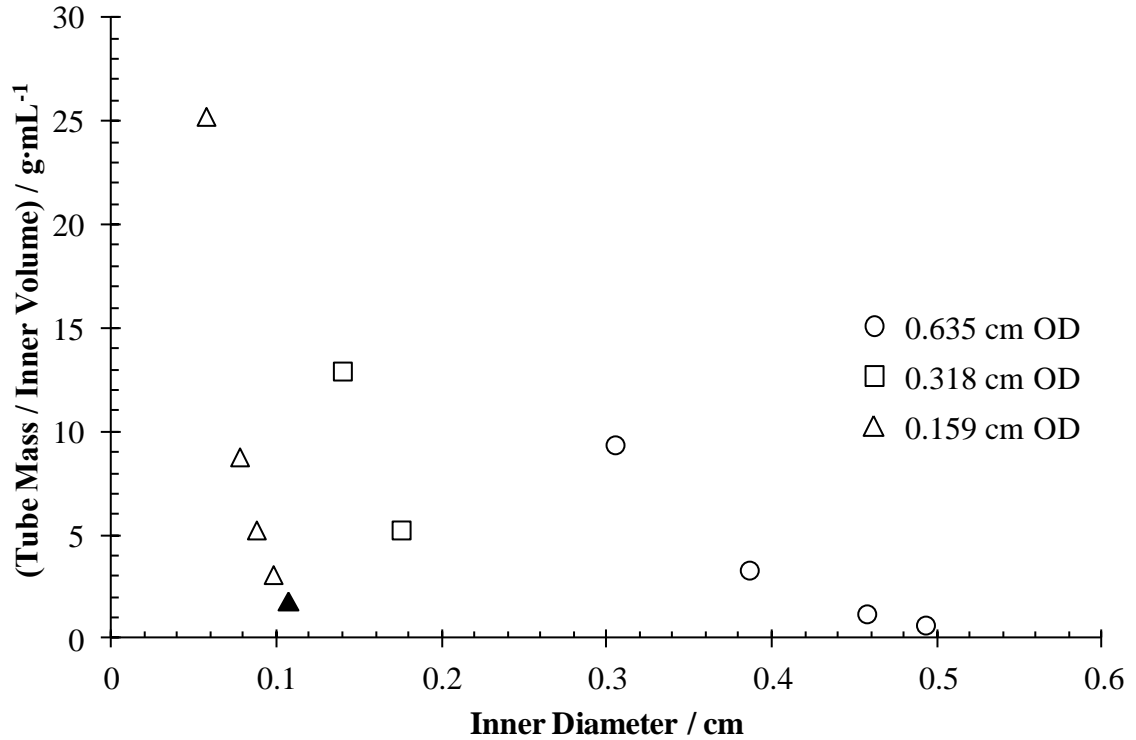


Figure 5. Sensitivity ratio for different dimensions of 316L stainless steel tubing in 30 cm lengths. ▲, tube dimensions similar to those used in the densimeter for this work.

Another factor for consideration is that the mechanical properties of a larger diameter tubes may not be necessarily ideal for the design of a vibrating tube densimeter. Assuming a rectangular cantilever of width w , thickness h , length L , and Young's modulus, E , the equation for the vertical displacement at the end of a cantilever spring, z is^{34,35}

$$z = \frac{4F_z L^3}{Ewh^3}, \quad (2-2)$$

and can be rearranged for the cantilever spring constant, k_z , using the force of the vibration, F_z , yielding

$$k_z = \frac{F_z}{z} = \frac{Ewh^3}{4L^3}. \quad (2-3)$$

Altering the shape of the cantilever from a rectangular cross-section will change the moment of inertia; however, this only changes the coefficient (1/4 in this case) and the spring constant will remain exponentially proportional to the thickness of the cantilever. Therefore, the effect of the thickness of the spring on the spring constant is maintained and increasing the thickness will exponentially increase the constant.³⁵ This means that a 0.635 cm OD tube with a larger spring constant requires a much larger driving force than a 0.159 cm OD tube, *i.e.*, heavier electronics are needed to handle the voltage increase so that enough current passes through the drive coil to create the vibrating tube's oscillation.

Plotting the pressure ratings³³ (working pressures) for tubes of varying inner and outer diameters (see Figure 6) reveals a correlation between the pressure rating of the tube and the sensitivity ratio whereby in order to maintain the best sensitivity, it is best not to go beyond the desired pressure rating for the densimeter. No longer considering 0.635 cm OD diameter tubing, a 0.159 cm diameter 316L stainless steel tube with an inner diameter of 0.11 cm would meet the desired 35 MPa pressure requirement while maintaining a good sensitivity ratio.

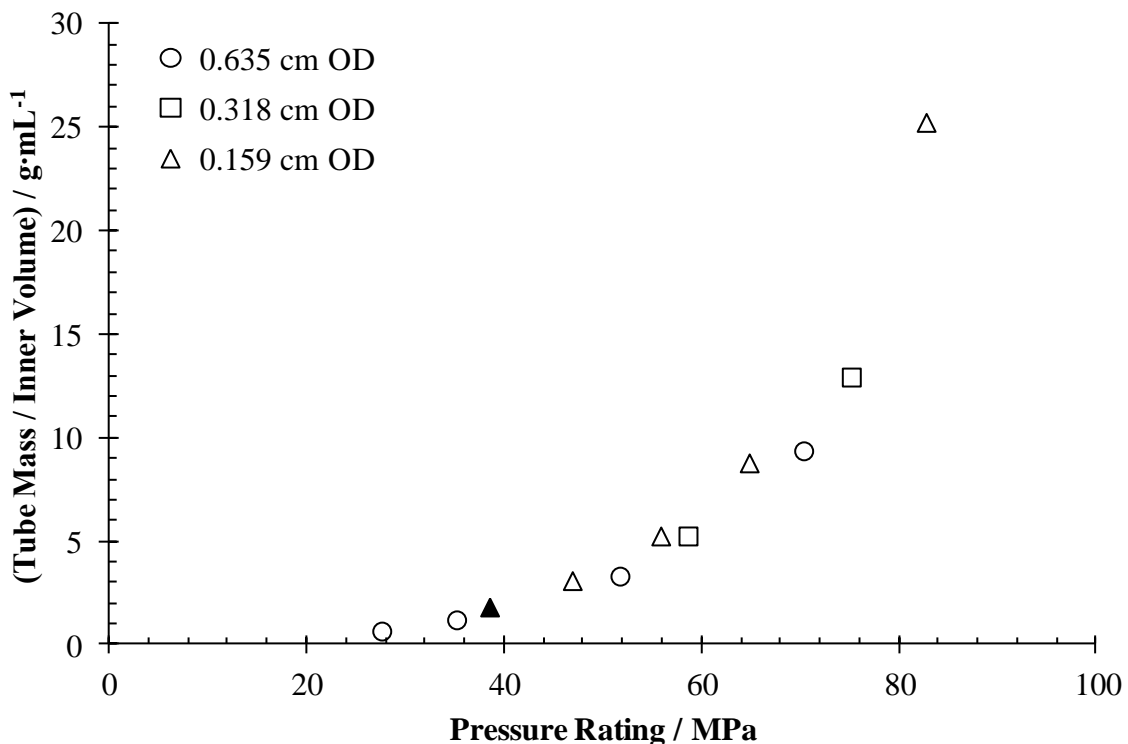


Figure 6. Plot of the pressure rating against the sensitivity ratio for various sizes of stainless steel tubing. \blacktriangle indicates tube dimensions similar to those used in the densimeter for this work.³³

As a result of the above discussion, the chosen vibrating tube for the densimeter was a 1.6 mm OD Hastelloy C276 (1.0 mm ID) bent into a U-shape and securely soldered to a stainless steel block to reduce any damping effects. The internal volume of the vibrating tube densimeter was measured to be $1.77 \pm 0.05 \text{ cm}^3$.

Figure 7 shows the normalized oscillation time period of the vibrating tube by using the time period of the evacuated tube and plotting it against calculated densities for high-pressure H_2O ,³⁶ CO_2 ,⁸ and He .³⁷ All equation-of-state calculations completed in this work were carried out using the Reference Fluid Thermodynamic and Transport Properties

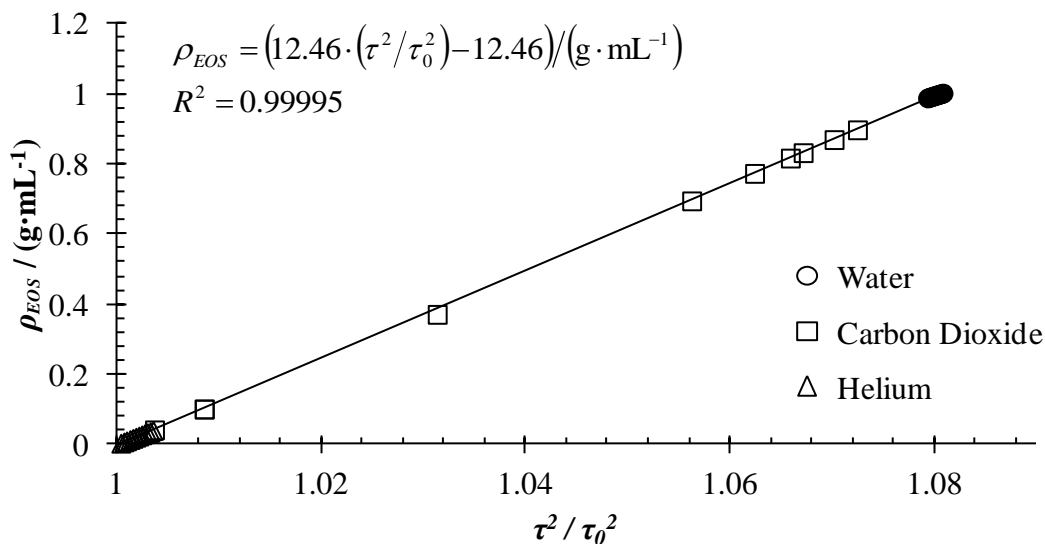


Figure 7. Determining the sensitivity ratio, m_0/V_{00} , by plotting the normalized time period versus a range of densities at $T = 50 \text{ }^\circ\text{C}$. The time period is normalized using τ_0 as the time period of the vibrating tube, evacuated to $p = 2 \times 10^{-6} \text{ bar}$ at $T = 50 \text{ }^\circ\text{C}$.^{36,37}

(REFPROP) software provided by the National Institute of Standards and Technology (NIST).³⁸ A linear least squares regression shows the densimeter in this work has sensitivity ratio, m_0 / V_{00} , of $12.46 \text{ g} \cdot \text{mL}^{-1}$ and has the expected linear relationship between the time period squared and the density ($R^2 = 0.99995$), independent of fluid type. Commercial high-pressure vibrating tube densimeters made by Anton Paar have sensitivity ratios ranging between 5.5 and $16.4 \text{ g} \cdot \text{mL}^{-1}$ depending on their design,³² with smaller slopes indicating a more sensitive densimeter due to a larger change in the time period for the same density change. This densimeter falls within the range of sensitivities typically observed in commercial instruments while maintaining a smaller internal volume⁵² for safety considerations.

2.1.2 Measurement Cell Design

A schematic diagram showing all of the components of the vibrating tube densimeter has been shown in Figure 8 with a more detailed computer-aided drafting (CAD) depiction of the measuring cell has been shown in Figure 9. The tube is excited into a resonance vibrational mode using electromagnetic forces. A small iron tab tacked onto the apex of the tube (see Figure 9), propagates the magnetic field, provided by a samarium cobalt magnet, onto the tube itself while reducing the amount of extraneous mass added to the tube. This magnetic field then interacts with the alternating field produced by the drive coil that is situated perpendicular to the plane of the tube; therefore, generating attractive and repulsive forces to drive the tube vibration. The vibration is then optically detected using fiber optic cables to deliver the light signal from the light emitting diode (LED) source. The fiber optic cables were custom manufactured by IAC & Associates Inc. and an LED source was chosen for its ability to provide a stable, high-intensity light over several years of lifetime.³⁹

The vibrating tube passes through a gap between the two fiber optic cables and light is partially impeded from reaching the detector in proportion to the tube's position. The oscillating light signal coming from the detecting fiber optic cable is converted into a voltage *via* a photodiode detector before being processed by the feedback amplifier electronics (built in the Chemistry Electronics Workshop by Edward Cairns). The voltage from the detector typically has a maximum amplitude of less than 0.5 V (0.45 V while evacuated at $T = 50$ °C). Within the feedback electronics, the voltage signal from the detector is transformed into a square wave and amplified to 13.75 V before being fed

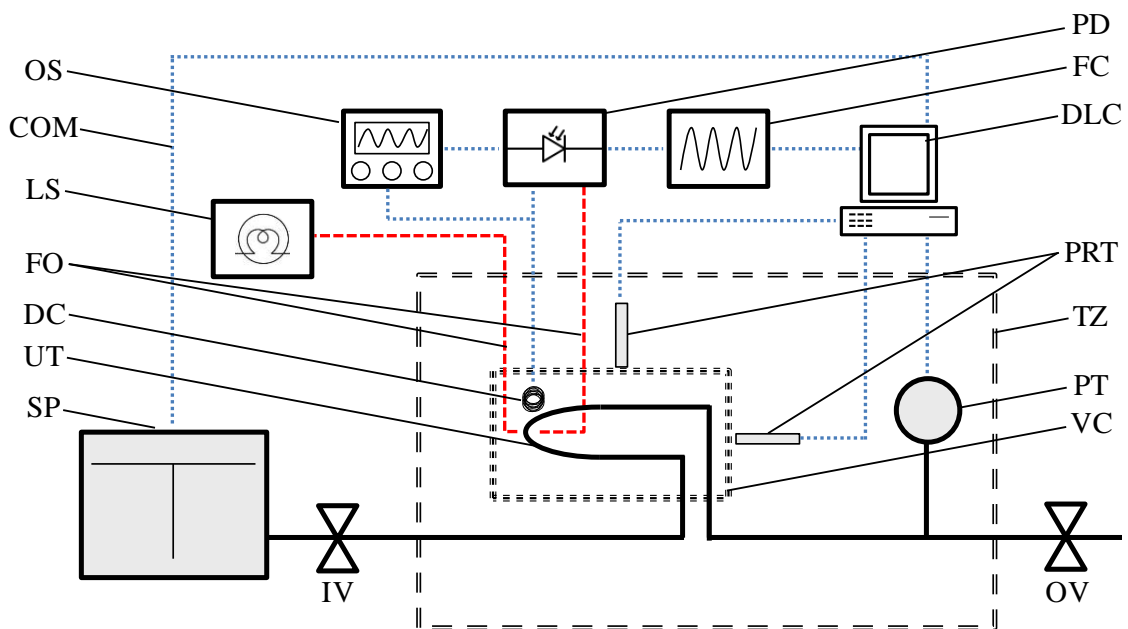


Figure 8. A simplified schematic diagram of the vibrating tube densimeter: OS, oscilloscope; LS, light emitting diode light source; COM, data communication line; FO, fiber optic cables; DC, electromagnetic drive coil; UT, vibrating U-tube (measurement cell); SP, high-pressure syringe pump; PD, photodiode detector and feedback drive signal, (feedback electronics); FC, frequency counter; DLC, data logging computer; PRT, 100 Ω , four-wire platinum resistance thermometer; PT, pressure transducer; VC, high vacuum chamber; TZ, temperature controlled zone; IV, inlet valve; OV, outlet valve.

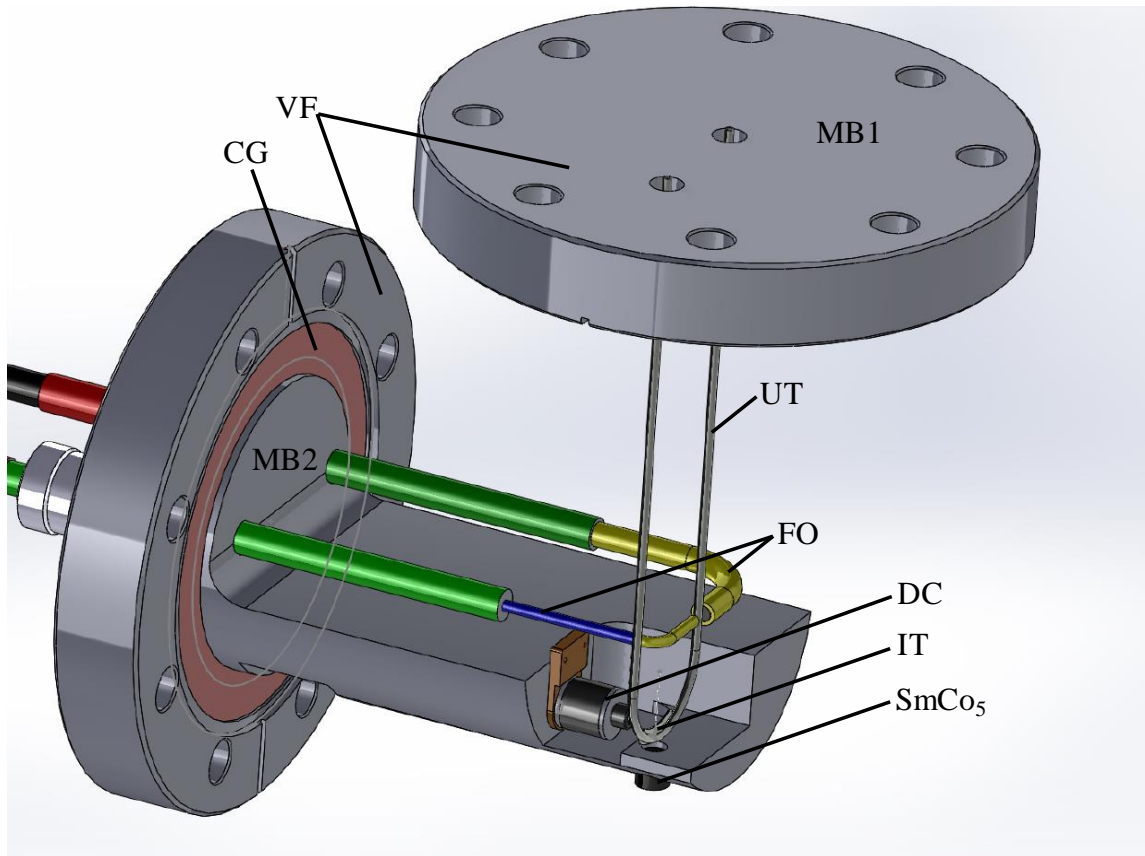


Figure 9. A computer-aided drafting (CAD) depiction of the vibrating tube densimeter measurement cell: VF, DN63 conflat vacuum flanges; CG, copper gasket; UT, vibrating U-tube; FO, fiber optic cables; DC, electromagnetic drive coil; IT, iron tab; SmCo₅, samarium cobalt magnet; MB1, first measurement block; MB2, second measurement block.

back to the drive coil as the drive signal. As such, this allows for a clean and nearly direct feedback response to focus the vibration of the tube on its mass-dependent harmonic frequency.

When the detector signal reaches its mid-point (inflection point), the electronics are triggered to switch the sign of the square drive voltage between ± 13.75 V. The shape and amplitude of the detector and drive signals are monitored using a Tektronix TDS 2012 oscilloscope while the time period of the detector signal is measured by a BNC Model 1105 frequency counter with a resolution of 40 ps.

Due to the optical motion detection, proper alignment between the window of the detecting fiber optic cable and the vibrating tube is crucial in achieving steady, sinusoidal motion and a corresponding linear drive to maintain the periodic motion. A side view of a tube passing through the light beam (fixed pick-up window) is shown in Figure 10. Based on the total distance covered by the tube during vibration ($2A$) and the radius of the light-beam (r), there are three possible scenarios: (i) $2A \leq r$ [Figure 10], (ii) $2A > 2r$, and (iii) $r < 2A < 2r$.

In case (i), where $2A \leq r$, five possible alignment configurations exist as outlined in Figure 10. If the tube crosses the perimeter of the light (Figure 10A) or asymmetrically across the mid-line (Figure 10D) before returning, deformities in the detector response voltage occur at the maximum and minimum respectively. Thus, the tube must be aligned so that either the entire path of vibration is within the same half of the light (Figure 10B

and Figure 10C) or the vibration occurs evenly across the midline (Figure 10E) of the beam. In the latter case, the tube will try to vibrate at its second harmonic frequency because the drive signal will have twice the number of maxima and minima.

In case (ii), where $2A > 2r$, a flattening of the detector response voltage occurs at both the maximum and minimum similar to that shown in Figure 10A. There is no possible alignment that can correct this and the densimeter would either need to be modified to either decrease the amplitude of the vibration or increase the detection area. Modification of the electronics could reduce the driving force provided by the drive coil in order to reduce the vibration amplitude, *e.g.*, reducing the detector signal amplification to the drive signal, while using a fiber optic cable with a larger light beam would provide a larger detection area to follow a wider range of motion during the tube vibration.

In the final case (iii), where $r < 2A < 2r$, modes B and C in Figure 10 are not possible, as they must be either modes A or D; therefore, driving at the second harmonic with mode E (driving at the twice the harmonic frequency) is the only way to achieve fluid motion.

This vibrating tube was found to operate under case (i) as deformities in the detector signal were not occurring in the maxima or minima simultaneously and eventually a smooth sinusoidal signal was obtained meaning cases (ii) and (iii) respectively were not occurring. Additionally, because a smooth signal was obtained, configurations A and D (outlined in Figure 10) also are not occurring. Configuration E can be ignored for the

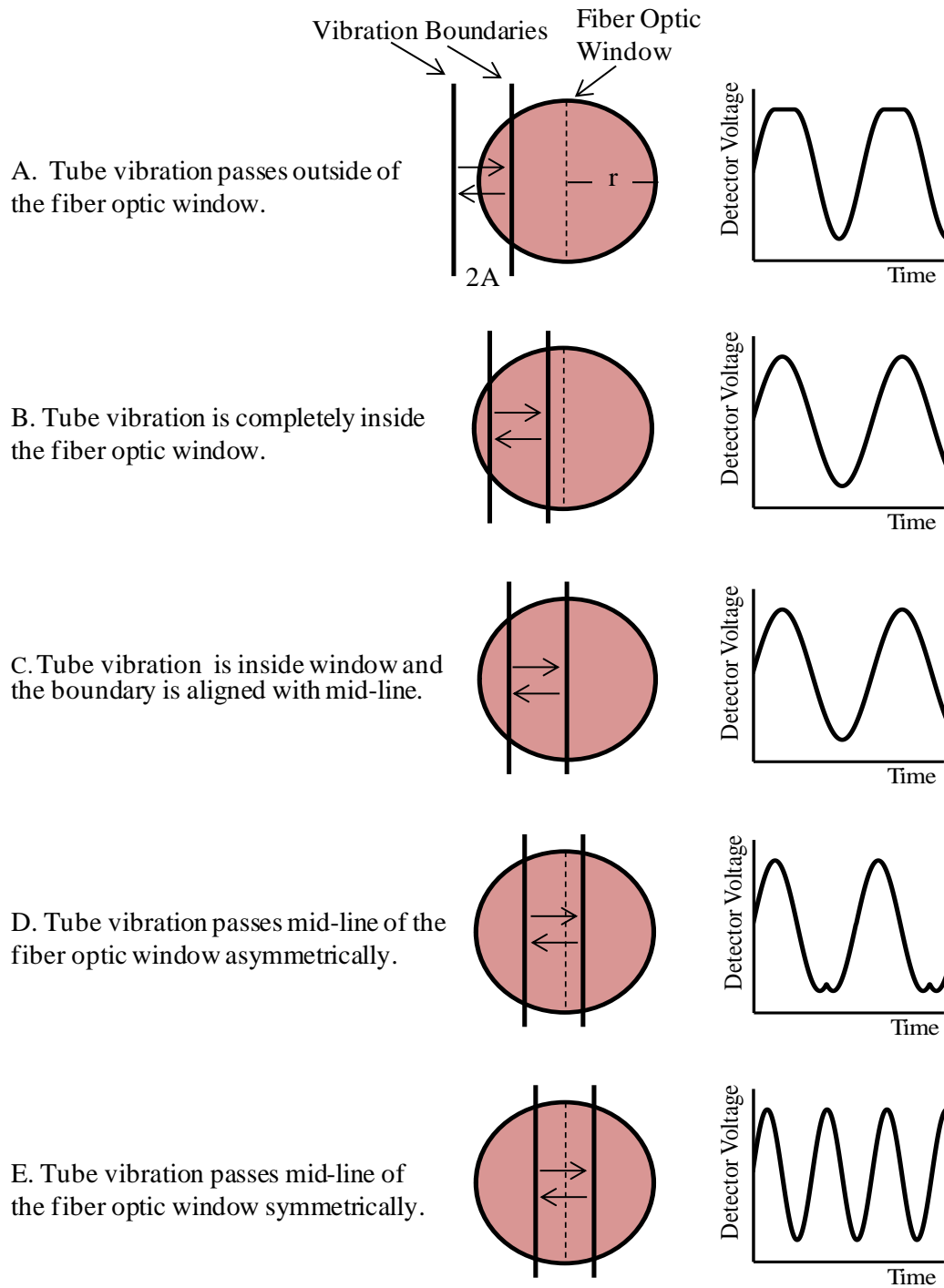


Figure 10. Alignment configurations of the vibrating tube operating under case (i) where the path length of the vibration is less than the radius of the window.

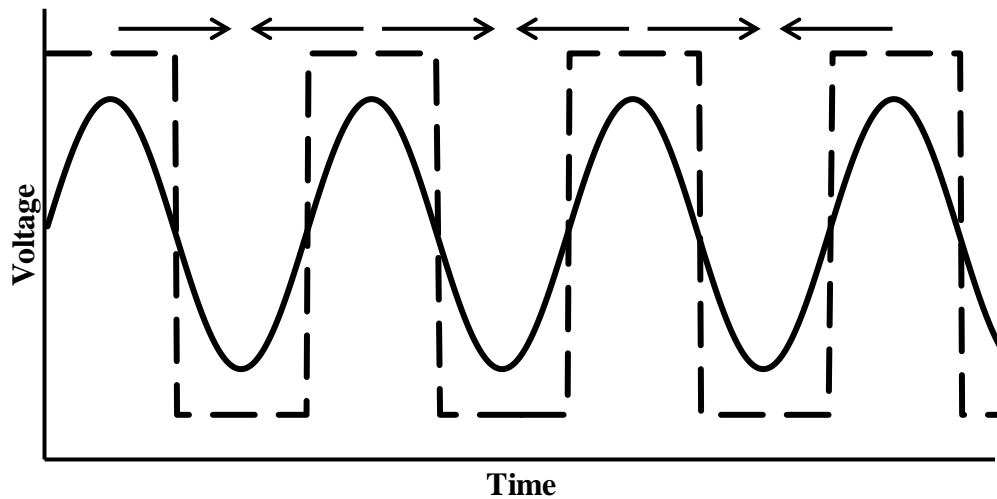


Figure 11. Representation of the phase and shape of drive signal (dashed line) with respect to the detector signal (solid line) and the motion of the tube (arrows) over time.

densimeter alignment, because the time period measurement of the vibrating tube's oscillation was not observed at twice the frequency.³² That leaves the densimeter operating under case (i) under either configuration B or C with the only difference between the two being a small amplitude change in the detector signal. Because the signal is amplified to a constant drive voltage; this small amplitude difference in the detector signal has no effect on the operation of the densimeter.

When the tube is at its maximum amplitudes, the detector signal will be at a corresponding maximum or minimum value in a case (i) configuration of B/C. The detector signal will be at its minimum value when the tube is at its closest point to the mid-line of the fiber optic pickup window within the vibration path (right boundary line in Figure 10B/C), because it is blocking the most light from going into the window at this point. When the detector signal is at its maximum, the tube is closest to the perimeter of

the beam (left boundary in Figure 10B/C), blocking the least amount of light. Thus, the tube is moving from the perimeter of the window towards the mid-line after a maximum in the detector signal and before reaching the minimum (see Figure 11). After the minimum in the detector signal, the tube then travels back towards the perimeter before another maximum is reached, allowing the complete motion of the tube to be followed.

2.1.3 Measurement Blocks and Measurement Cell Housing

The measurement cell of the vibrating tube densimeter is divided onto two machined stainless steel blocks (built by Jay McIssac of the Science Workshop), labelled MB1 and MB2 in Figure 9; MB1 anchors the vibrating tube itself while MB2 secures the drive/detection components. Both blocks are fixed at right angles in a DN63 (11.43 cm ID) conflat vacuum four-way cross (housing). Having two anchoring blocks presents several advantages over earlier prototypes which were mounted on a single block. First, it relieves crowding around the vacuum feedthroughs so that tighter machining and soldering work could be completed. Second, the presence of two blocks reduces damping and any potential effects caused by external vibrations. Any extraneous vibration of the fiber optic cables will be on the other block (MB2) and should not be measured in the tube vibration signal as it would also occur perpendicular to the tube vibration. The third advantage is that a second block allows for the fiber optic probes to be positioned perpendicular with respect to the tube's motion allowing for a wider range of adjustment in getting the strongest and most linear signal from the detector.

The measurement blocks are connected to two of the arms on a high-vacuum four-way cross fitting using conflat flange seals with copper gaskets designed for use with ultra high-vacuum systems. The third arm of the vacuum cross leads to a window to help with the optical alignment process described earlier while the remaining arm is in communication with a Turbo-V 81 TPS Compact turbomolecular vacuum pump system (Agilent) which can evacuate the measurement cell to pressures on the order of $p = 10^{-9}$ mbar. Typically the vacuum inside the housing cross is close to $p = 10^{-4}$ mbar. Having a vacuum atmosphere surrounding the vibrating tube maintains a more constant environment than ambient conditions, making for a more stable drag force acting on the tube due to a consistent atmospheric density.⁴⁰ Table 1 shows the effect of the vacuum on the short-term stability of the time period measurement, resulting in a standard deviation reduction of at least an order of magnitude when the vacuum is on compared to the measurement cell in communication with ambient air. A vacuum atmosphere also has the added benefit of reducing the long term drifts due to slight changes in the tube mass caused by metal oxidation or outer surface adsorption due to atmospheric species such as H₂O.

Table 1. Effect of a high-vacuum atmosphere on the stability (standard deviation, σ) of the time period of the vibrating tube's oscillation at $T = 50$ °C.

	σ , Tube Evacuated	σ , 32.5 MPa H ₂ O
Turbomolecular Pump OFF	147×10^{-10} s	86×10^{-10} s
Turbomolecular Pump ON	10×10^{-10} s	3×10^{-10} s

The vacuum cross containing the measurement cell is contained within a modified Hewlett-Packard 5890 gas chromatography oven to control the temperature. The temperature was monitored using four-wire 100 Ω platinum resistance thermometers with a PT-104 temperature data logger (Pico Technologies). The PRTs were calibrated according to the ITS-90 with an accuracy of ± 0.005 °C detailed later in section 3.1.

Fluids were delivered to the vibrating tube using two high-pressure syringe pumps (Teledyne ISCO Model 260D) and a supercritical CO₂ chromatography pump (Chrom Tech Model SFC-24) controlling the pressure to deviations better than $\delta p = \pm 0.005$ MPa. One syringe pump was used to deliver H₂O into the densimeter for the calibration procedure while the other pumps delivered sample fluid for density measurements. When the fluid is sealed into the densimeter using the inlet valve (see Figure 8), the pressure fluctuation was less than $\delta p = \pm 0.003$ MPa, because the isochoric fluid is isolated from the constant adjustments from the syringe pumps and temperature fluctuations in the laboratory space.

The pressure inside the densimeter was measured using a Paroscientific 410KR Digiquartz pressure transducer calibrated to an accuracy of $\pm 0.0052\%$ using a deadweight test (see section 3.2). It was found that thermostating the electronics of the transducer with a PolyScience PP07R-40 circulator bath to $T = 26.00 \pm 0.05$ °C helped the stability of the pressure reading, shown in Table 2, as it minimized the effect of room temperature fluctuations on the piezoelectric measuring crystal inside the transducer.

Table 2. Effect of thermostating the pressure transducer electronics to $T = 26.00\text{ }^{\circ}\text{C}$ ($\pm 0.05\text{ }^{\circ}\text{C}$) on measurement stability (A), as well as the frequency counter and signal electronics on the standard deviation of the vibrating tube's time period (B).

A. Pressure Measurement

Temperature	50 °C		75 °C	
Pressure	Evacuated	9.3 MPa N ₂	Evacuated	9.4 MPa N ₂
Bath On	$\pm 0.0003\text{ MPa}$	$\pm 0.0008\text{ MPa}$	$\pm 0.0005\text{ MPa}$	$\pm 0.0007\text{ MPa}$
Bath Off	$\pm 0.0020\text{ MPa}$	$\pm 0.0014\text{ MPa}$	$\pm 0.0025\text{ MPa}$	$\pm 0.0025\text{ MPa}$

B. Period Measurement

Temperature	50 °C		75 °C	
Pressure	Evacuated	9.3 MPa N ₂	Evacuated	9.4 MPa N ₂
Bath On	$1.0 \times 10^{-10}\text{ s}$	$1.5 \times 10^{-10}\text{ s}$	$5.6 \times 10^{-10}\text{ s}$	$11.8 \times 10^{-10}\text{ s}$
Bath Off	$1.2 \times 10^{-10}\text{ s}$	$1.7 \times 10^{-10}\text{ s}$	$33.8 \times 10^{-10}\text{ s}$	$27.4 \times 10^{-10}\text{ s}$

Similar thermostating of the feedback circuit and the frequency counter provided no significant improvement to the stability of the vibrating tube's time period when the oven was at $T = 50\text{ }^{\circ}\text{C}$. However, improvements were noticed at $T = 75\text{ }^{\circ}\text{C}$ so the thermostating was left in place.

When used in conjunction with different inlet and outlet valve orientations, the fluid delivery pumps could perform with different measurements schemes: (i) having both valves closed after initially loading the tube with fluid allows for maximum thermal isolation of the fluid, (ii) keeping the inlet valve open allows for isothermal or isobaric static measurements, and (iii) opening both valves allows for isothermal or isobaric flow measurements. In this work, measurements are carried out under the isothermal static mode, because achieving a hydrostatic equilibrium in the apparatus was found to be faster than achieving a thermal equilibrium. Also, static measurements require much less fluid to operate which is ideal when working with toxic fluids. Automating the syringe pumps

through a LabVIEW interface significantly reduced the involvement (physical presence) required by the operator in running the instrument. The same LabVIEW interface was also used to log the temperatures, pressures and time period measurements. These were logged into a tab delimited .DAT file for further analysis and processing.

2.2 Interfacing the Densimeter to a Computer

2.2.1 LabVIEW

LabVIEW is a graphical programming language designed for those working with measurement and control systems. Instead of using many different measurement modules and their individual softwares to monitor and control an instrument, LabVIEW provides a platform to integrate all of the components into a single control panel. This allows for interaction and event timing between the modules where it was not previously possible, making it ideal for instrument control. The LabVIEW platform comes with a “front panel” where controls and displays can be accessed and changed by the user while the program is running and a “block diagram” in the background that contains the actual programming language used by the front panel. Once the program has been started, the block diagram cannot be edited again until the program stops. As shown in Figure 12, the LabVIEW front panel has consolidated the instrument controls and data collection for the PRTs, pressure transducer, frequency counter, the circulator bath and the syringe pumps used with the vibrating tube densimeter. All coding was developed for this thesis work.

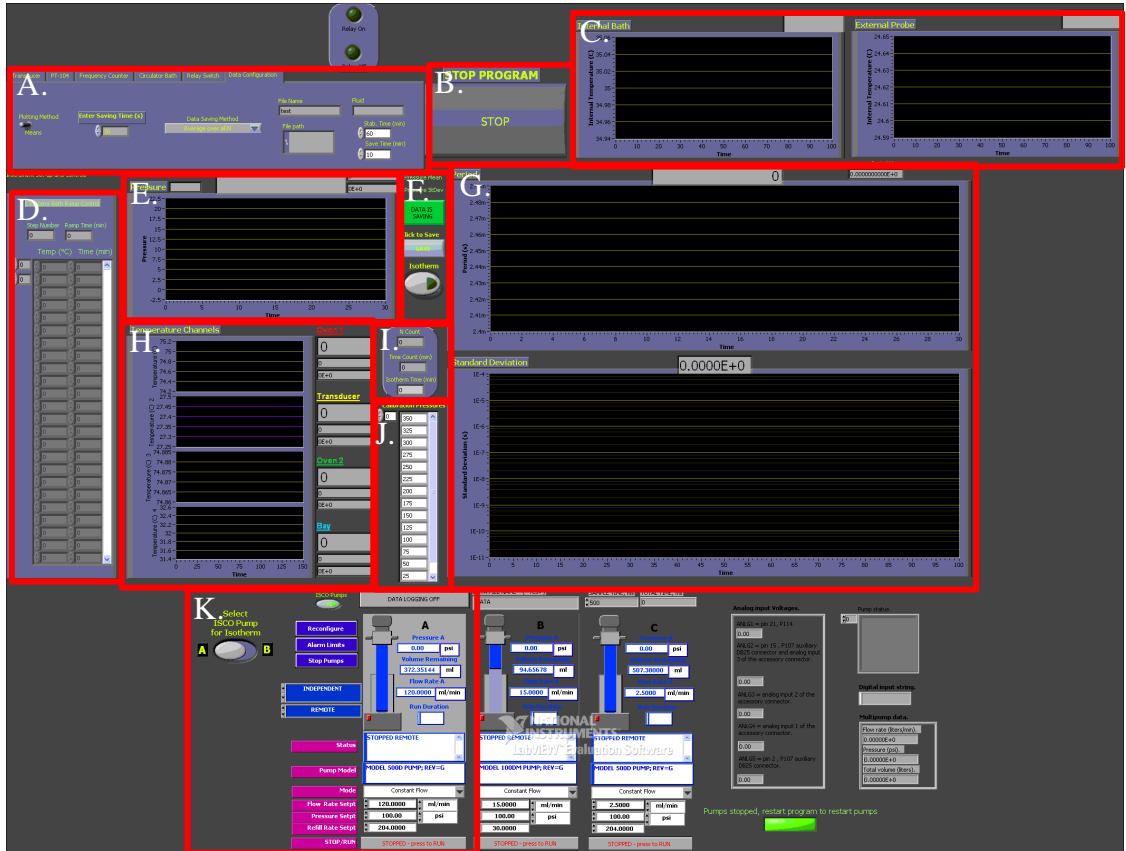


Figure 12. Full LabVIEW front control panel for operating the vibrating tube densimeter: A, tabbed controls for setting up device communication and configuration of data collection (see Figures 13 and 15); B, program shut-off button; C, live-update circulator bath plots for internal bath temperature and the external probe if connected; D, circulator bath temperature ramp control; E, live-update plot of pressure measurement from transducer (see Figure 16); F, manual data saving control, data saving indicator, and automated pressure set point procedure control; G, live-update plots of time period measurement and time period standard deviation from frequency counter; H, live-update plots for each connected temperature probe; I, time count (elapsed), “N” count, and time of automated pressure procedure indicators; J, set point list for automated pressure procedure; K, syringe pump controls (see Figure 14).

2.2.2 COM Communication and Device Controls

Figure 13 shows the tabbed controls developed for setting up the communication protocol for the transducer. The COM port through which the transducer is connected to the PC is

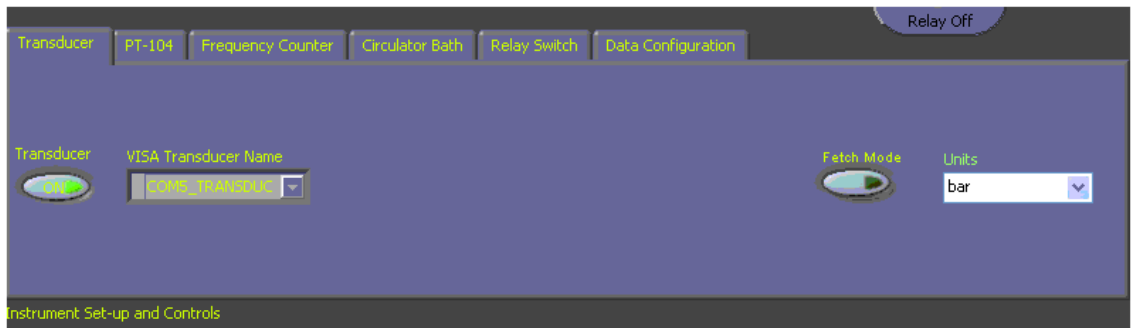


Figure 13. Transducer settings tab in LabVIEW control panel.

chosen out of the drop down list, with the baud rate, data bits, parity bit and stop bits already being defined in the block diagram (not shown) to meet the device’s communication specifications. The user is able to control the units that the transducer measurement is displayed in, and the data measurement process by either collecting a ‘read on command’ or ‘continuously’ (fetch mode) while only sending the latest value when called upon. The COM ports are set up in the same way for the other connected devices with only the COM port number needing to be chosen. The PT-104 data logger control allows the user to choose which types of PRT is connected to each channel or if the channel is not in use. Both the arm time over which the frequency counter makes its measurement and the number of counter measurements (N) to average before giving a value can be adjusted by the user (see Figure 15). The current “N Count” value being measured is displayed in an indicator next to the top left of the temperature plot, just above the “Time Count” displaying how long the program has been running (Figure 12I).

Although not being used, there is a relay switch control which had originally been put into place to control an air operated solenoid valve to reduce the pressure automatically

over a period of time. This and other features were used during the instrument development and PRT calibrations.

The controls for the syringe pumps are separate from the other devices (in the tabbed settings) as they are often changed when the program is running (controlling of up to three pumps simultaneously when the program is running). Typically there are two pumps connected as “Independent”. While operating independently, each pump can operate in “Constant Pressure”, “Constant Flow”, or “Refill” modes in addition to different types of pressure and flow rate gradients. The parameters for the pumps can be adjusted either remotely (through LabVIEW) or locally (from the pump controller module).

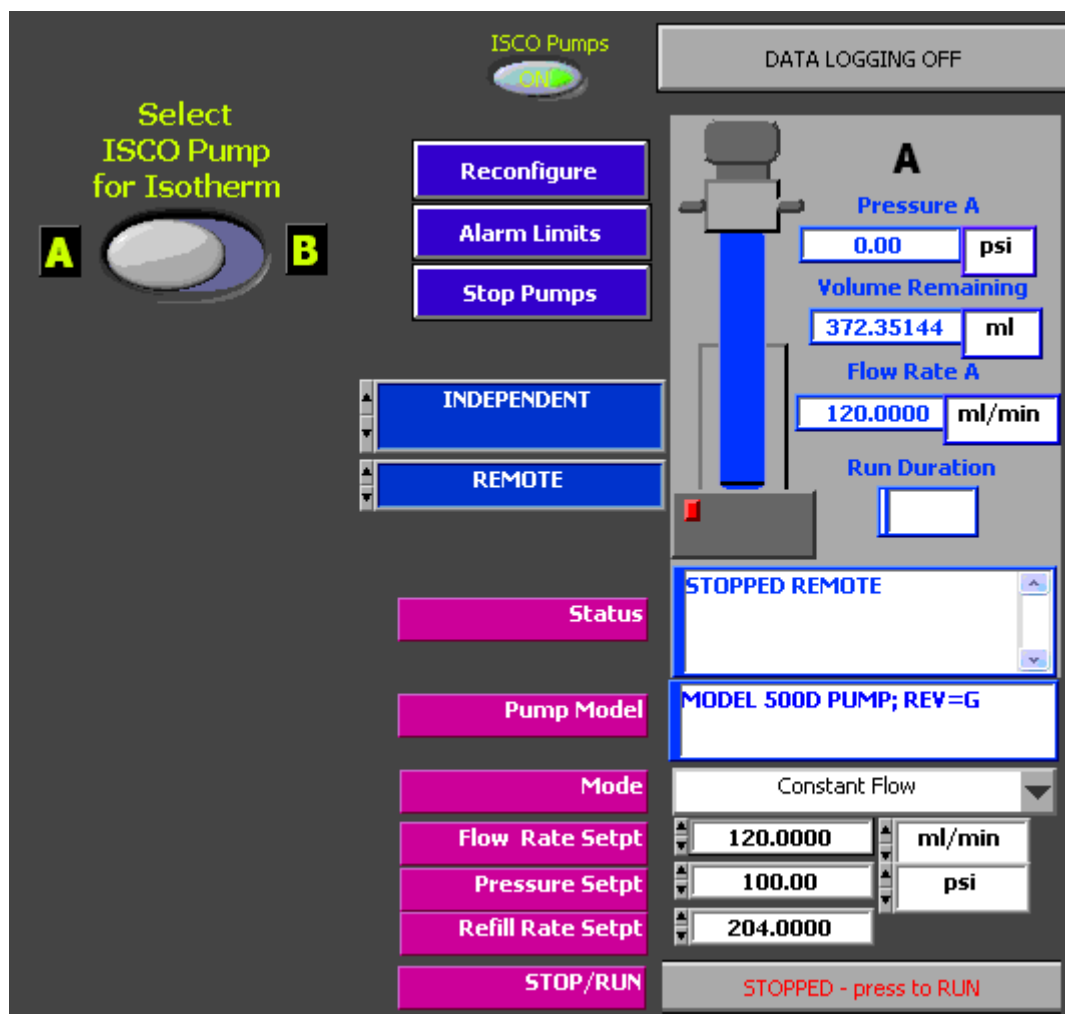


Figure 14. Syringe pump “A” controls in LabVIEW panel. Pumps “B” and “C” have identical panels.

An automated pressure set-point procedure can be started using the “Isotherm” control (Figure 12F) and can be used for either pump *via* the “Select ISCO Pump for Isotherm” (Figure 14). Each desired pressure set point is entered into the “Calibration Pressures” list (Figure 12J) with the first value being sent to the selected syringe pump upon pressing the “Isotherm” control (Figure 12F). The procedure then waits for the “Stabilization Time” before saving the data over the “Saving Time” (Figure 15). After the data is saved

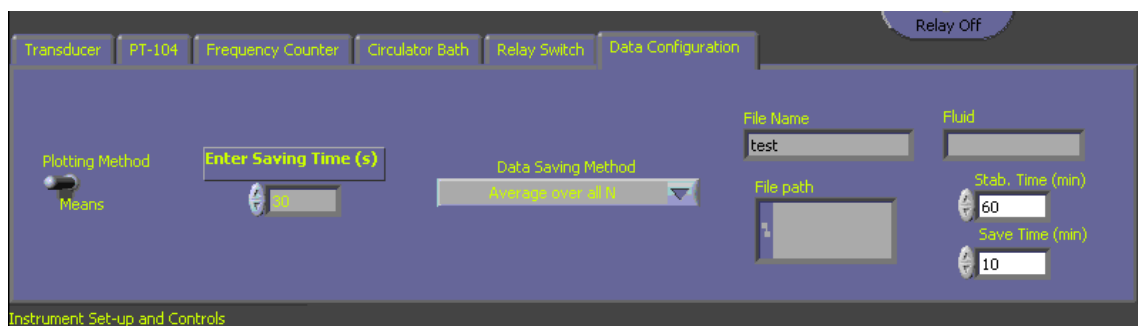


Figure 15. Data configuration settings tab in LabVIEW panel.

over the “Saving Time”, the second set point is sent to the pump and the procedure repeats itself until all the set points in the list have all been completed. The “Isotherm Time” indicator (Figure 12I) displays the time elapsed for the current stabilization or saving.

2.3.2 Data Collection Configuration

Data collection (Figure 15) can be done over a pre-set time interval (“Enter Saving Time (s)”) or over the time that the frequency counter is making its measurement (arm time multiplied by N) through the “Data Saving Method” control. The data collection takes place manually when the “Click to Save” button (Figure 12F) is depressed, turning the “Data Saving” indicator immediately above the button, green. Pressing the button again, will reset the button, stop recording data and turn the indicator red. In both cases, while the data is being saved, the data is averaged over the interval before being compiled into a .DAT file which can then be opened with applications such as Microsoft Excel for further analysis. The standard deviation for each averaged datum is also collected in this

file for use in determining the measurement error. The user enters the desired file name into the “File Name” string control as well as the fluid being measured in the “Fluid” control before starting the program, so it can be identified in the data collection folder in the C:// drive of the computer. Using the “Plotting Method” control, either the averaged values or individual measurements of the four temperature probes, pressure, time period, and time period standard deviation are sent to live update plots in the center portion of the control panel over a user determined amount of time so they can be monitored. The plots for each measurement device have an indicator readout to provide the last numerical value that was recorded, shown in Figure 16 for the pressure transducer.

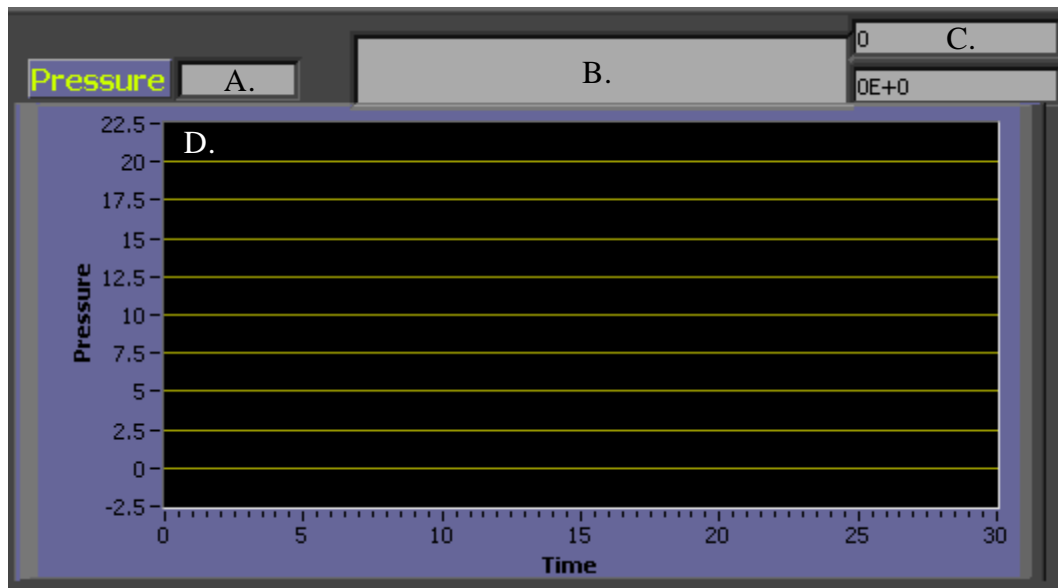


Figure 16. Live-update pressure plot with measurement indicators in the LabVIEW panel: A. units of pressure measurement; B. last measured pressure value; C. average and standard deviation for the last set of pressures measured; D. live-update plot of the pressure over the last user-defined time interval.

Chapter Three: Calibration and Measurement Procedures

In order to properly operate a vibrating tube densimeter, a number of procedures must be developed. Firstly, a calibration procedure must be determined in order to relate the time period of the tube's vibration to a density measurement. A second procedure must be developed to deliver the fluids of interest into the densimeter so that the time period of the vibrating tube can be measured and converted into a density by using the calibration. Ideally, both the fluid measurement and calibration procedure should be designed to maximize accuracy and precision while minimizing measurement times and computational effort. Like any p - V - T measurement, the temperature and pressure must be measured accurately and thus require independent calibrations. This chapter outlines the calibration and measurement procedures for the densimeter as well as the calibration procedures for PRTs and pressure transducer.

3.1 Temperature Calibration

3.1.1 The International Temperature Scale of 1990

The International Committee of Weights and Measures adopted the International Temperature Scale of 1990 (ITS-90), which provides the latest definition of thermodynamic temperature in units of Kelvin.⁴¹ The ITS-90 provides a temperature scale from 0.65 K up to any measurable temperature using sets of standardized ranges and sub-ranges each defined by primary reference points or the Planck radiation law. These fixed references are used to apply an accurate primary calibration to a thermometer. A combination of consecutive overlapping ranges and reference points may

also be used in order to calibrate the thermometer over a wider temperature region. The reference points can consist of either phase-change transitions or triple point temperatures of various pure species. The measured transition is fixed with the accepted literature value provided in the ITS-90 to create a calibration equation for the thermometer being tested. PRTs respond linearly to temperature within the range of this instrument (25 to 150 °C); therefore, two or more reference points allows for a linear calibration.

Provided a primary calibration has already been completed for one thermometer, secondary temperature calibrations may then be completed for subsequent thermometers through comparison. Keeping the thermometers within an isothermal region or in thermal contact with each other allows for a correlation between the temperature measurements of the calibrated device with those being calibrated. Any number of temperature values can be used for this type of calibration, with one, two or more points allowing for constant, linear, or higher order calibration equations respectively.

The ITS-90 also provides a number of secondary reference points whose temperatures have also been accurately determined using the primary references.⁴² They can be used in creating a primary calibration for a thermometer in place of the primary standards; however, typical issues with these secondary references arise due to the purity of the material, reproducibility of the reference temperature, the agreement of literature values, or some combination thereof. Secondary reference points such as the melting point of benzoic acid are useful in filling any large gaps between primary reference points in

certain temperature ranges or for checking the accuracy of the calibration equation following the primary calibration procedure.

3.1.2 Apparatus and Materials

The temperature range of interest for the vibrating tube densimeter spans from $T = 25$ to $150\text{ }^{\circ}\text{C}$ (298 K to 423 K). ITS-90 recommends that within that region, thermometers are to be calibrated using the triple point of H_2O at $T = 0.010\text{ }^{\circ}\text{C}$ and the melting point of indium at $T = 156.5985\text{ }^{\circ}\text{C}$. If a somewhat larger temperature calibration range is desired, the melting points of mercury ($-38.8344\text{ }^{\circ}\text{C}$), tin ($231.928\text{ }^{\circ}\text{C}$), zinc ($419.527\text{ }^{\circ}\text{C}$) or aluminum ($660.323\text{ }^{\circ}\text{C}$) can be used.⁴¹ The melting point of benzoic acid, a secondary calibration point, at $T = 122.352\text{ }^{\circ}\text{C}$ was used in this work to check the accuracy of the primary calibration equation.

There were four 100 ohm , four-wire PRTs which were calibrated for this instrument (one primary and three secondary). Temperature control was achieved using a PolyScience PP07R-40 circulating bath with an accuracy of $\delta T = \pm 0.005\text{ }^{\circ}\text{C}$ using 50:50 ethylene glycol:water as the circulating fluid for temperatures below $T = 100\text{ }^{\circ}\text{C}$ and Inland 200 silicone oil for temperatures above $T = 100\text{ }^{\circ}\text{C}$. Indium ($\geq 99.999\%$) and the calibration standard benzoic acid were purchased from Sigma-Aldrich and used without further purification. H_2O was purified using an EMD Millipore Milli-Q water treating system to a resistance of $18\text{ ohm}\cdot\text{m}^{-1}$ followed by degassing for several hours under vacuum just before use. The three reference standards were each contained within 13 cm long 316L

stainless steel vessels of 1.27 cm OD, and a 0.64 cm opening at the top so that the PRT could be inserted down into the bulk. The vessels were filled approximately half full of each reference standard, using about 20 g of indium, 15 cm³ of H₂O and 8 g of benzoic acid before being immersed in the circulating bath. Temperatures were only recorded for the melting temperature due to obstruction of the true freezing point temperature caused by irreproducible super-cooling of the liquid before the freezing occurred.

3.1.3 Primary Temperature Calibration Method

The solid indium metal was first melted at $T = 160$ °C in the circulator bath, and then the probe was inserted into the liquid metal. The metal was then cooled to $T = 150$ °C for solidification around the probe and left for four hours to form a stable solid. Following this relaxation time, the indium was then continuously heated back to $T = 160$ °C over $t = 40$ minutes to obtain the melting point temperature at 156.5985 °C.⁴¹ This cycle was repeated a total of five times to ensure reproducibility.

To measure the melting point of ice as the second point in the primary calibration, the H₂O was first cooled to a temperature of $T = 5$ °C before inserting the probe. The system was then further cooled to form solid ice at a temperature of $T = -10$ °C and left for four hours to anneal before continuously heating it back up to $T = 5$ °C over 60 minutes to obtain the melting point temperature of $T = 0.000$ °C.⁴¹ Again, the measurement was repeated for a total of five times.

To check the accuracy of the calibration points, the benzoic acid was first melted at $T = 130\text{ }^{\circ}\text{C}$ before the probe was inserted into the liquid. The benzoic acid with the probe was then cooled down to $T = 105\text{ }^{\circ}\text{C}$ to solidify and then left to anneal for four hours. Finally, the benzoic acid was heated back up to $T = 130\text{ }^{\circ}\text{C}$ over 60 minutes, and the melting point at $T = 122.352\text{ }^{\circ}\text{C}$ was recorded.⁴¹ The cycle was repeated a total of three times.

3.1.4 Secondary Temperature Calibration Method

To calibrate the remaining three PRTs against the newly calibrated primary PRT, the four probes were put in very close proximity within the circulator bath. Once the bath reached a thermal equilibrium, data were collected for two minutes before changing to the next temperature. Ten stable temperatures were used from $T = 0.01$ to $156.60\text{ }^{\circ}\text{C}$.

3.1.5 Results & Discussion

Both the indium and the H_2O are fixed reference points as outlined by the ITS-90 and were used in creating a calibration for one of the PRT. While the melting point of H_2O is only a secondary reference, it is much more attainable than the triple point primary reference as the PRT probe does not need to be sealed within the measurement chamber to hold vacuum. In order to make each of the phase transitions as isothermal as possible, the heating rate of the circulator bath had to be optimized. It was observed that two requirements were needed for a good first-order phase transition: (i) a sharp, identifiable

initial inflection in the measured temperature, and (ii) a stable, constant temperature while the transition is occurring. If the heating rate is too slow, the temperature inflection at the start of the transition will not be readily apparent; on the other hand, if the heating rate is too fast, then the temperature of the newly formed phase may increase to match the still increasing bath temperature, affecting the area adjacent to the platinum resistance probe resulting in an unstable measurement. A heating rate of $0.25\text{ }^{\circ}\text{C}\cdot\text{min}^{-1}$ through the transition temperature was found to reasonably satisfy both of these conditions; however, the transition temperature did tend to drift upwards after an initial plateau, during which the measurements were taken as shown in Figure 17. As a result, the first 15 sample points were used in determining the transition temperature, where each point represents the average of the data collected for the five seconds prior to it.

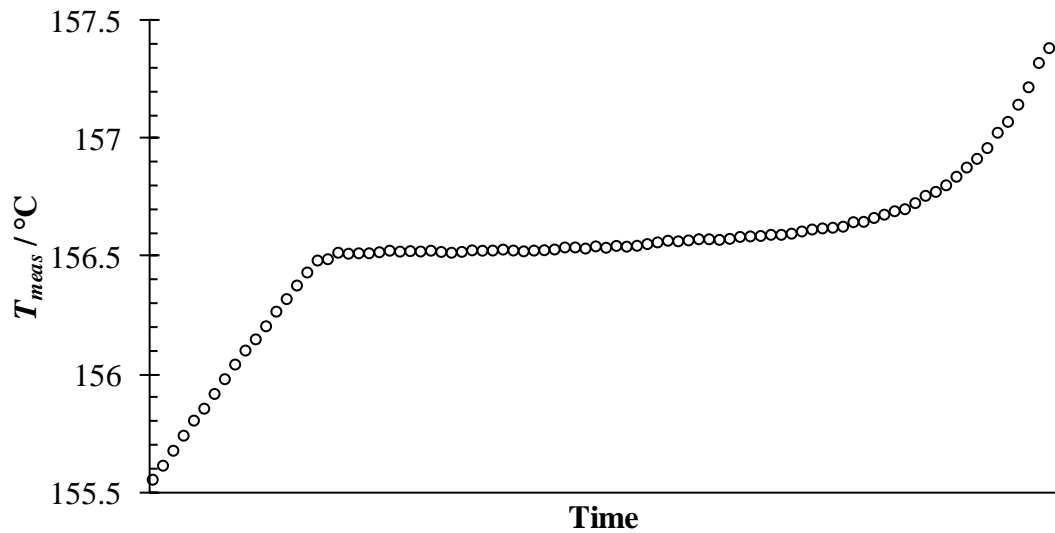


Figure 17. Representative plot of the temperature, measured by the PRT, over time during the heating of indium past its melting point temperature ($156.5985\text{ }^{\circ}\text{C}$).

The measured phase transition temperatures were then plotted against their respective literature values, as shown in Figure 18, with the calibration equation for the PRT being given by a linear regression of the form:

$$T_{lit} = AT_{meas} + B, \quad (3-1)$$

where A and B are the calibration slope and intercept, respectively. The values of A and B , representing the calibration equations for the four PRTs are summarized in Table 4. Using each of the five runs for both H₂O and indium in calculating equation 3-1 allows for the determination of the error in both the slope and intercept by least squares analysis (see Table 4). At $T = 156$ °C, the error in the slope results in a temperature deviation of $\delta T = \pm 0.0016$ °C, which results in an overall error less than the actual temperature deviation for individual measurements. Thus the error in the equation was considered to be a result of the deviations in each individual measurement.

Table 3. The experimentally measured melting points of indium (primary calibration point), H₂O (primary calibration point) and the benzoic acid (calibration accuracy control) with their corresponding experimental errors.

Run	Indium		H ₂ O		Benzoic Acid	$\frac{T}{\text{°C}}$	$\frac{\delta T}{\text{°C}}$
	$\frac{T}{\text{°C}}$	$\frac{\delta T}{\text{°C}}$	$\frac{T}{\text{°C}}$	$\frac{\delta T}{\text{°C}}$			
1	156.523	± 0.005	-0.038	± 0.004	Measured	122.278	± 0.005
2	156.528	± 0.006	-0.041	± 0.006	Calibrated	122.343	± 0.005
3	156.527	± 0.006	-0.037	± 0.003	Literature	122.352	± 0.007
4	156.526	± 0.006	-0.040	± 0.004			
5	156.530	± 0.006	-0.043	± 0.006			
Average	156.527	± 0.006	-0.040	± 0.005	$T_{lit} - T_{cal}$	0.009	± 0.012
σ	0.003		0.003				

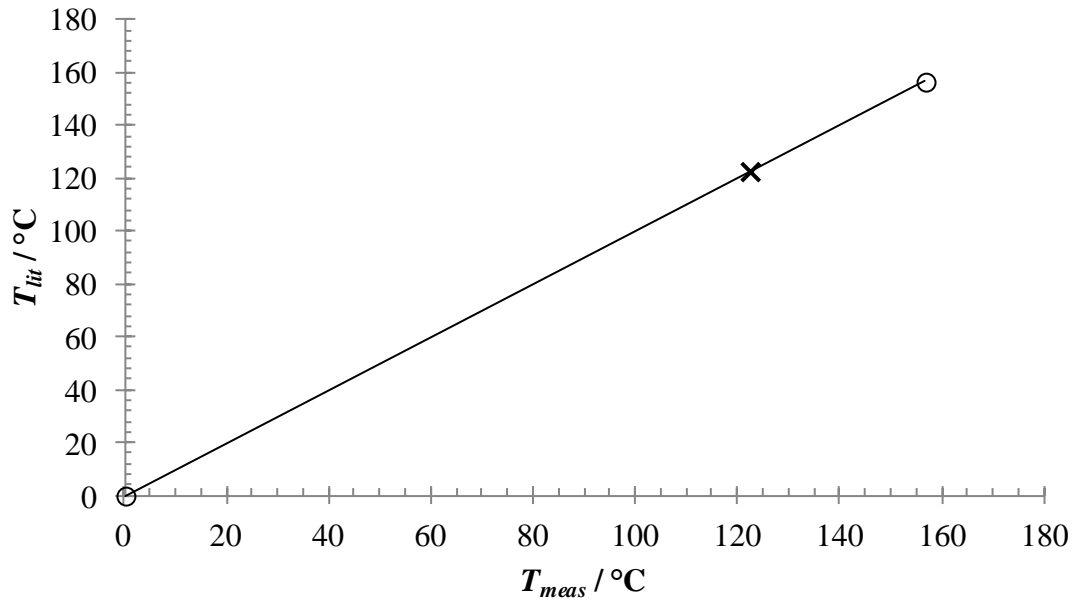


Figure 18. Primary calibration plot of the measured temperature, T_{meas} , against the accepted literature temperature, T_{lit} , in determining equation 3-1 for a PRT using the melting point of indium (156.5985 °C) and H₂O (0.000 °C) as reference points according to the ITS-90 guidelines.⁴¹ (x) denotes the melting point of benzoic acid (122.352 °C) used to check the accuracy of the calibration.⁴²

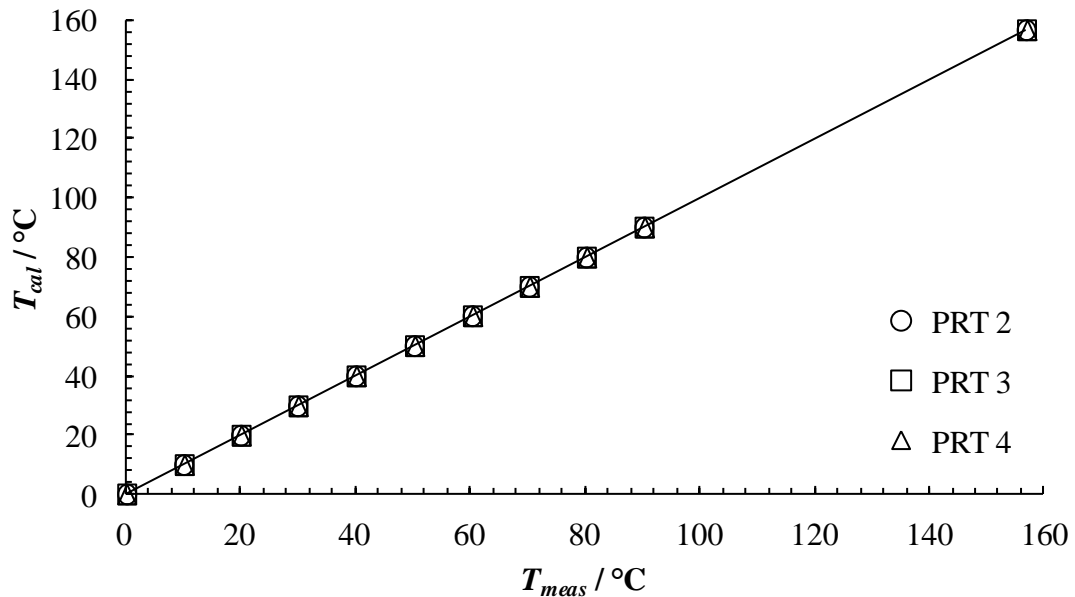


Figure 19. Secondary calibration plot for comparing the temperature measurements of three additional PRTs (T_{meas}) against the temperature measured by the primary calibrated probe (T_{cal}) between $T = 0$ °C and 155 °C.

The secondary calibrations of another three PRTs were carried out through a comparison against the primarily calibrated thermometer. As shown in Figure 19, the temperature measured by each of the platinum probes, T_{meas} , was plotted against the temperature of the calibrated probe, T_{cal} , and fitted with a linear regression, giving a secondary calibration equation the form:

$$T_{cal} = AT_{meas} + B. \quad (3-2)$$

Again, A and B are the calibration slope and intercept, respectively, and can be found in Table 4.

Table 4. Calibration equation parameters for the four PRTs. The superscript “s” denotes a secondary calibration.

Calibration Parameter	A	δA	$\frac{B}{^{\circ}\text{C}}$	$\frac{\delta B}{^{\circ}\text{C}}$
Primary PRT	1.00020	0.00001	0.040	0.001
PRT 2 ^s	0.99967	0.00012	-0.030	0.008
PRT 3 ^s	1.00003	0.00016	-0.121	0.011
PRT 4 ^s	0.99946	0.00011	-0.157	0.007

3.2 Pressure Calibration

3.2.1 Deadweight Piston Gauges/Testers

Deadweight piston gauges provide a good primary pressure calibration for any above ambient pressure measuring device because the accuracy depends on a separately measured quantity, mass. By mounting a well-known mass to the head of a piston assembly on the tester, the induced pressure is then transferred along the fluid column into a gauge to be calibrated. Ideally, the pressure, p , is given by^{43,44}

$$p = \frac{F}{A_{cs}} = \frac{\sum_i m_i g}{A_{cs}}, \quad (3-3)$$

where F is the force acting on the piston assembly over a cross-sectional area, A_{cs} . The force is then given by the sum of the mass mounted on the piston, $\sum m_i$, multiplied by the acceleration constant due to gravity, g . To ensure an accurate calibration, the applied force needs to be corrected for the local gravity, the buoyancy of the weight stack on the hydraulic fluid, the local temperature and the thermal expansion of the instrument, expansion of the effective area due to the applied pressure, and any additional static head pressure caused by a height difference between the transducer and piston. These corrections then extend equation 3-3 to^{43,44}

$$p_{corr} = \frac{\sum_i m_i g_l}{A_p} \left(1 - \frac{\rho_{air}}{\rho_{mass}} \right) + g_l \rho_{fluid} (\Delta h), \quad (3-4)$$

where

$$A_p = A_e (1 + [\alpha_p + \alpha_c] [T - T_{ref}]), \quad (3-5)$$

and

$$A_e = a_0 (1 + b_d p). \quad (3-6)$$

a_0 represents the effective area of the piston at ambient pressure and the reference temperature, T_{ref} , at which the properties of the deadweight piston were initially measured. The pressure distortion coefficient, b_d , in equation 3-6 is used to calculate the constant temperature effective area, A_e , when a certain amount of pressure is loaded. A_e is then converted to the temperature-corrected true effective area, A_p , through equation 3-5 for the temperature at the time of calibration, T , using the coefficients of thermal expansion for the piston and cylinder, α_p and α_c , respectively. Once A_p has been determined, the buoyancy correction is applied to the pressure equation using the ratio of air density, ρ_{air} , to the density of the weights, ρ_{mass} . Furthermore, the static head pressure correction is also applied due to the height difference, Δh , between the transducer and the bottom of the piston assembly using the local acceleration due to gravity, g_l , and the density of the hydraulic fluid, ρ_{fluid} .

Following the completion of a primary calibration, it may be easier to calibrate future pressure measuring devices using a secondary calibration procedure instead of going through the deadweight procedure again. Provided that both pressure gauges are in hydrostatic communication and at the same elevation, the pressure measurement from the calibrated gauge can be correlated to those measured by the uncalibrated devices. Using a number of different pressures as reference points, a linear regression can then be used to obtain a secondary pressure calibration equation.

3.2.2 Experimental Methods

A Pressurements Limited T 3800/4 Deadweight Tester with a provided calibrated weight set was used to apply pressures to a Paroscientific Inc. Digiquartz 410KR-HT-101 Pressure Transducer. Isopropyl alcohol was used as the hydraulic fluid instead of the provided oil so it could be easily removed from the transducer's chamber. Any air was removed from the hydraulic fluid transfer lines by opening the pressure-release valve (see Figure 20F) on the system and using the handpump (Figure 20A) to de-aerate while the fine-pressurization capstan (Figure 20D), controlling the total volume of the hydraulic fluid lines, was fully closed. The calibrated weights were cleaned and re-weighed to check if the certificate of calibration, provided with the tester, was still valid due to the age of the instrument. Pressures were then applied to the piston assembly by mounting the appropriate mass on the weight holder base (Figure 20H), closing the pressure-release valve, fully opening the capstan, and then using the pre-pressurization handpump (Figure 20B) to pressurize the system to just below the pressure of interest.

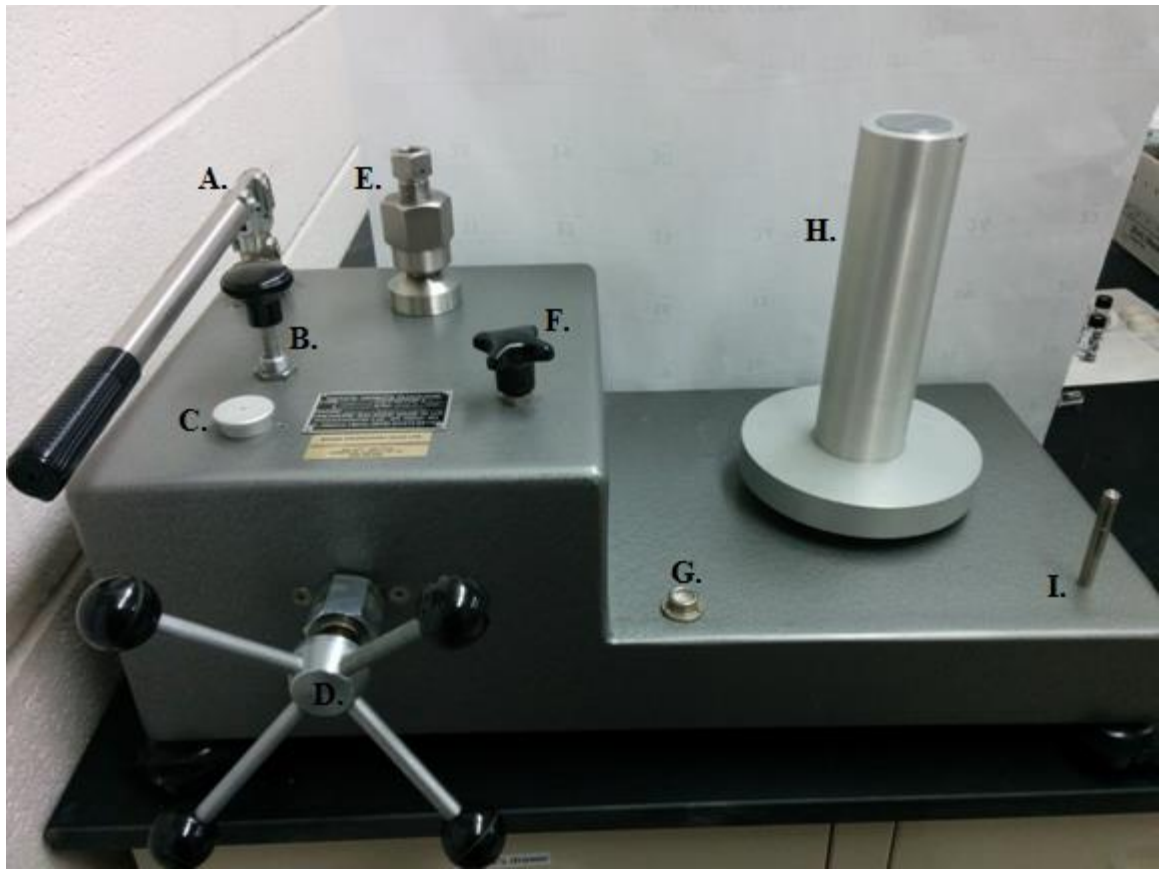


Figure 20. Pressurements deadweight tester used for pressure calibration: A, de-aeration handpump; B, pre-pressurization handpump; C, hydraulic fluid reservoir; D, fine-pressurization capstan; E, connection fitting for pressure device to be calibrated; F, pressure-release valve; G, bubble level; H, weight stack holder with base plate; I, base plate indication rod.

Next, the capstan was slowly closed resulting in a reduction of the fluid volume inside the tester, thus increasing the pressure, until the weight stack began floating and the upper side of the bottom of the base weight was between the two reference marks on the indication rod (Figure 20I). The weight stack was then spun in a clockwise direction between 40 to 100 rpm so a consistent pressure value can be obtained. Spinning of the weights helps reduce the frictional force between the cylinder and the piston, thereby minimizing the error normally associated static friction.⁴⁵ It should be noted that there

was only a short window for data collection when lighter mass was used because the weight stack and holder would not rotate under their own angular momentum for very long. Also, heavier weight stack and holder initially tended to float up and down on the piston upon spinning; therefore, more time was allowed for equilibrium to be reached before the pressure was recorded. Finally, the reference pressure was applied to the transducer for *ca.* two minutes before spinning the weight stack and obtaining the pressure measurement to allow enough time for the piezoelectric sensing element to come into equilibrium with the environment and read the correct value.

3.2.3 Results and Discussion

A number of parameters are required to calculate the theoretical pressure applied by the mounted mass. These parameters, listed in section 3.2.1, equations 3-4 through 3-6, were provided by the manufacturer and are summarized in Table 5 with the mounted mass and resulting applied pressures being given in Table 6. Furthermore, separate correction factors unique to the instrument were supplied for gravity, buoyancy, and pressure head that were accordingly incorporated as part of equation 3-4 to correctly estimate the theoretical pressure. The pressure range of the transducer went up to $p = 69$ MPa (10000 psia); but the minimum pressure of the deadweight tester and the desire to keep the transducer under its maximum working limit resulted in a calibration range of $p = 3$ MPa to 68 MPa (435 to 9863 psia) using various combinations of the provided calibration weights.

Table 5. Relevant parameters for deadweight calibration.⁴⁴

Parameter	Value
g_l	$9.8082 \text{ m}\cdot\text{s}^{-2}$
a_0	$4.06115 \times 10^{-6} \text{ m}^2$
b_d	$1.043 \times 10^{-8} \text{ MPa}^{-1}$
$\alpha_p + \alpha_c$	$2 \times 10^{-5} \text{ }^\circ\text{C}^{-1}$
T	$21 \text{ }^\circ\text{C}$
T_{ref}	$20 \text{ }^\circ\text{C}$
ρ_{air}	$1.22 \text{ kg}\cdot\text{m}^{-3}$
ρ_{mass}	$7300 \text{ kg}\cdot\text{m}^{-3}$
ρ_{fluid}	$785 \text{ kg}\cdot\text{m}^{-3}$
Δh	0.0635 m
$p_{vac,21^\circ\text{C}}$	0.0121 MPa

Table 6. Relevant mass and pressures for the deadweight calibration.

$\frac{\sum m_i}{\text{kg}}$	$\frac{p_{corr}}{\text{MPa}}$	$\frac{p_{meas}}{\text{MPa}}$	$\frac{\delta p_{meas}}{\text{MPa}}$
1.263669	3.0640	3.0712	0.0008
1.677730	4.0679	4.0720	0.0004
2.091826	5.0718	5.0723	0.0005
2.505887	6.0756	6.0722	0.0003
2.919969	7.0795	7.0721	0.0006
3.333955	8.0831	8.0715	0.0005
3.748016	9.0870	9.0709	0.0007
4.162112	10.0909	10.0710	0.0006
4.576173	11.0947	11.0709	0.0008
4.990255	12.0986	12.0706	0.0007
5.404590	13.1031	13.0707	0.0004
7.474876	18.1224	18.0677	0.0009
9.546211	23.1442	23.0680	0.0010

Table 6. Continued

$\frac{\sum m_i}{\text{kg}}$	$\frac{p_{corr}}{\text{MPa}}$	$\frac{p_{meas}}{\text{MPa}}$	$\frac{\delta p_{meas}}{\text{MPa}}$
9.960272	24.1480	24.0670	0.0008
10.374368	25.1520	25.0669	0.0005
10.788429	26.1559	26.0664	0.0007
11.202511	27.1598	27.0662	0.0009
11.616497	28.1635	28.0658	0.0009
12.030558	29.1673	29.0652	0.0007
12.444654	30.1713	30.0649	0.0007
12.858715	31.1752	31.0644	0.0007
13.272797	32.1791	32.0638	0.0007
13.687132	33.1837	33.0644	0.0011
15.757418	38.2031	38.0615	0.0009
17.828109	43.2236	43.0600	0.0012
19.898395	48.2431	48.0556	0.0008
21.969030	53.2635	53.0545	0.0014
22.383091	54.2674	54.0538	0.0011
22.797187	55.2714	55.0538	0.0014
23.211248	56.2754	56.0530	0.0014
23.625330	57.2794	57.0525	0.0011
24.039316	58.2831	58.0518	0.0012
24.453377	59.2871	59.0503	0.0017
24.867473	60.2911	60.0504	0.0011
25.281534	61.2950	61.0504	0.0016
25.695616	62.2990	62.0494	0.0012
26.109618	63.3028	63.0417	0.0024
28.179904	68.3226	68.0462	0.0018

The measured pressure for each mass was then plotted against the calculated pressures as shown in Figure 21, and a linear regression analysis was performed to obtain the calibration coefficient. The linear regression was forced through the origin because the temperature dependant vacuum and the static pressure head corrections had already been applied to the measured pressures and the calculated pressures, respectively. The resulting regression gave a pressure calibration equation in the form of:

$$P_{corr} = (1.003799 \pm 0.000052) p_{meas} . \quad (3-7)$$

Taking into account the error associated with the calibration coefficient, 0.0052%, errors of $\delta p = \pm 0.0018$ and ± 0.0001 MPa arise at a pressure of $p = 35$ and 2.5 MPa, respectively. The error quoted with each pressure measurement will then be whichever is greater between $\pm 0.0052\%$ or the standard error (variance) over the course of the measurement. Comparison of the calibration error against the standard measurement errors listed in Table 6 shows that the two are very similar. During operation of the vibrating tube, the standard error is typically greater when the syringe pumps are used to maintain pressure within the densimeter, because these pumps cycle over a range on the order of $\delta p = \pm 0.005$ MPa while trying to keep a constant pressure within the system.

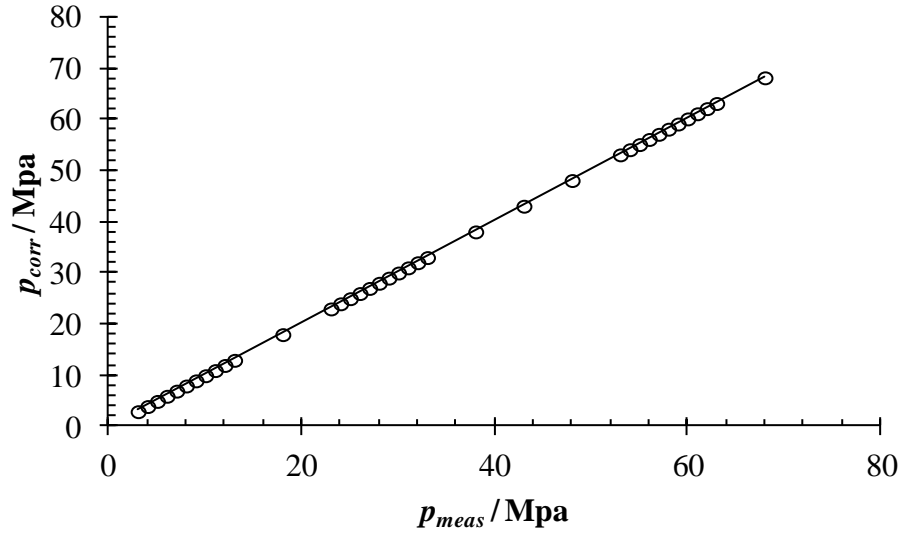


Figure 21. Deadweight primary calibration plot of the calculated applied reference pressures (p_{corr}) between $p = 3$ MPa and 68 MPa and their corresponding transducer measurements (p_{meas}).

3.3 Vibrating Tube Densimeter Calibration

Vibrating tube densimeters do not directly measure the density of a fluid, but provide a measurement relative to some reference fluid that must be chosen based on how accurately its density is known. The relationship between the density of the reference fluid, ρ_{ref} , and the density of the sample fluid, ρ , is then given by^{46,47,48}

$$\Delta\rho = \rho - \rho_{ref} = k_{T,p}(\tau^2 - \tau_{ref}^2), \quad (3-8)$$

where τ and τ_{ref} are the measured time period of the vibrating tube's mechanical oscillation when containing the reference fluid or the sample fluid, respectively. The difference between the square of the time period is transformed into a density difference through the temperature and pressure dependent calibration constant, $k_{T,p}$, which must be determined for each set of experimental conditions. Calibrations were carried out before

and after each batch of experiments at the same experimental temperature in order to negate any effects of long term drift that the vibrating tube might experience. This approach results in a calibration being performed every three to four days. The calibration procedure consisted of using two fluids whose densities were well known over the experimental temperature and pressure range. For this work, H₂O and a low-pressure nitrogen (N₂) were used, because their densities could be accurately calculated using the equations-of-state developed by Wagner and Pruß³⁶ and Span *et al.*,⁸ respectively. When the N₂ was at a low-pressure, typically 2 x10⁻⁶ bar using an Edwards RV12 rotary vane vacuum pump, the calculated densities⁴⁹ are on the order of 10⁻⁶ kg m⁻³, which is well below the expected sensitivity for the densimeter. Therefore, ρ_{ref} , or now, ρ_{N_2} , can be defined as 0 kg·m⁻³. After measuring the time period of the low-pressure N₂, equation 3-8 then becomes

$$\rho = k_{T,p} (\tau^2 - \tau_{N_2}^2), \quad (3-9)$$

leaving $k_{T,p}$ to be solved for each experimental temperature and pressure with the help of the second calibration fluid, H₂O. Water calibration constants were measured over the whole range of experimental pressures and a linear equation was fit to the data for each experimental temperature.

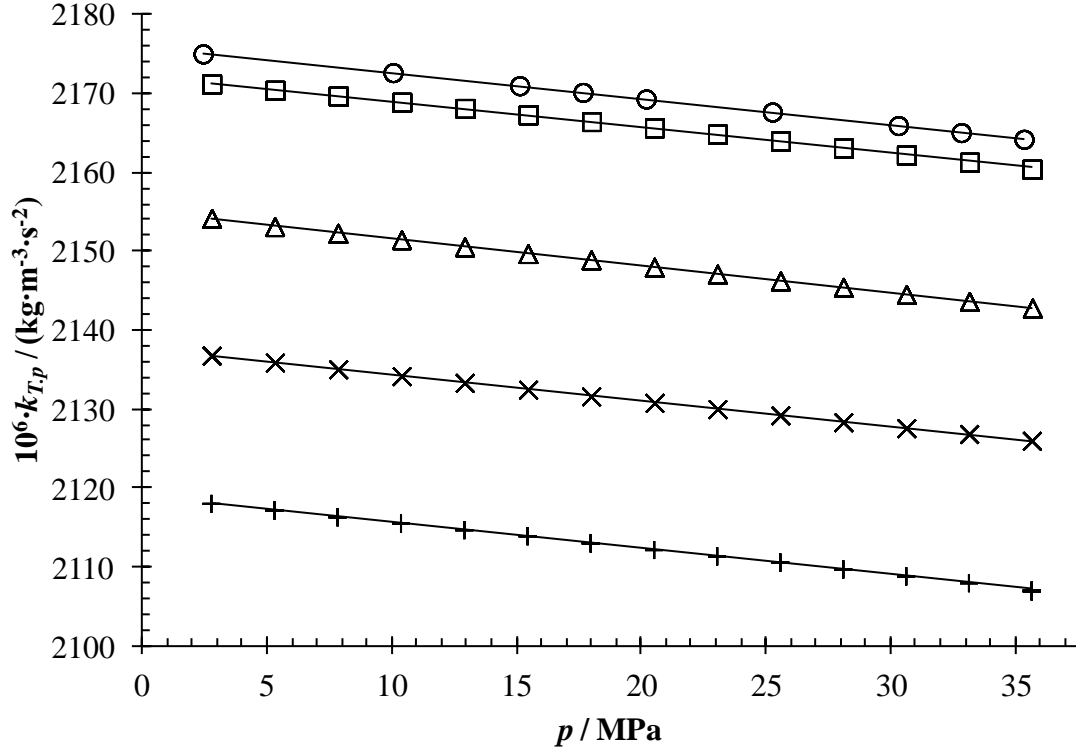


Figure 22. Pressure dependence of the calibration constant, $k_{T,p}$, with their respective linear regressions over the experimental pressure range up to $p = 35$ MPa using H₂O and N₂ as the calibration fluids at different temperatures: (○), 45.132 °C; (□), 49.747 °C; (Δ), 73.089 °C; (×), 96.253 °C; and (+), 119.850 °C.

The relative density equation can be expanded to give a linear equation often shown in the literature:^{32,50,51}

$$\rho = A_{T,p} \tau^2 - B_{T,p}, \quad (3-10)$$

where

$$A_{T,p} = k_{T,p}, \quad (3-11)$$

and

$$B_{T,p} = k_{T,p} \tau_{ref}^2 - \rho_{ref}. \quad (3-12)$$

May *et al.*³² have outlined an extensive calibration procedure to determine a model based on seven parameters describing the physical properties of the vibrating tube using

commercially available densimeters that was briefly discussed in chapter 2 of this work (equation 2-1). The model is again given by:

$$\rho = \frac{(\rho_m / S_{00})}{(1 + \alpha_v T + \beta_v p)} \left(\left(\frac{\tau}{\tau_{00}(1 + \varepsilon_{\tau 1} T + \varepsilon_{\tau 2} T^2)} \right)^2 (1 + \beta_\tau p) - 1 \right), \quad (3-13)$$

and when compared to the previous density equations, gives both

$$A_{T,p} = k_{T,p} = \frac{(\rho_m / S_{00})(1 + \alpha_v T + (\beta_v + \beta_\tau)p)}{\tau_{00}^2 (1 + \varepsilon_{\tau 1} T + \varepsilon_{\tau 2} T^2)}, \quad (3-14)$$

and

$$B_{T,p} = k_{T,p} \tau_{ref}^2 - \rho_{ref} = (\rho_m / S_{00})(1 + \alpha_v T + \beta_v p). \quad (3-15)$$

A , B , and $k_{T,p}$ are all linearly related to the pressure of the fluid inside the tube; thus, the pressure dependence of $k_{T,p}$ can be determined using a linear least squares regression even though commercial instruments typically recommend a power series expansion.^{32,52}

The initial time required for to complete the extended May et al. calibration is quite substantial because it requires many measurements over the entire pressure and temperature range from at least two reference fluids (see Figure 23). Also, a number of measurements must be made over the temperature range while the tube is evacuated in order to define the linear and quadratic temperature response coefficients. Although it would be time saving over the course of a large number of experimental measurements, the long-term drift of the densimeter may often require repeating calibrations in order to ensure the stability of the seven parameters. The drift for a custom-built densimeter would be instrument-dependant. Initially, the calibration procedure would have to be completed often, until confidence could be maintained that the equation parameters

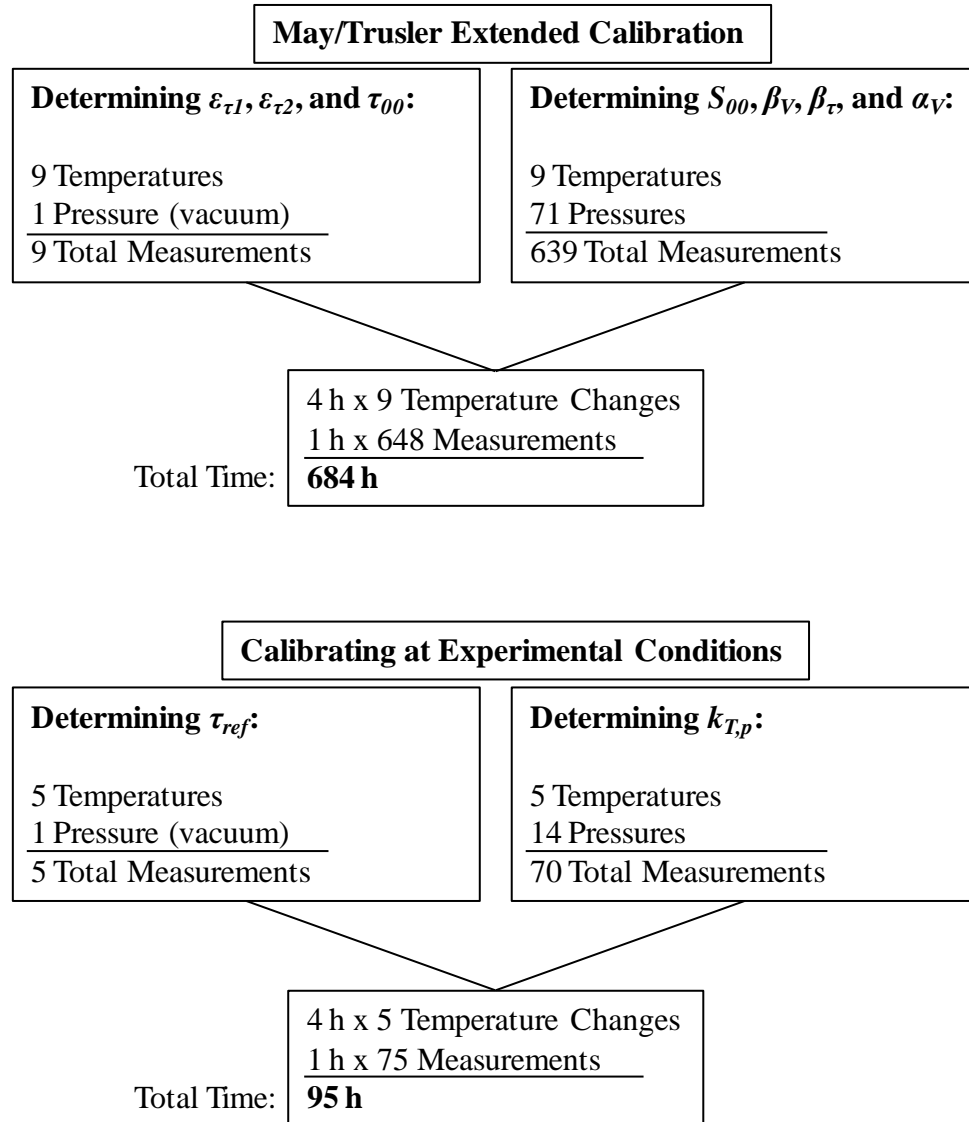


Figure 23. Comparison of the total calibration time required for completing density measurements at temperatures of $T = 45, 50, 75, 100,$ and $125 \text{ }^\circ\text{C}$ for the densimeter outlined in this work assuming one hour for pressure stabilization and measurement time and four hours for thermal equilibrium to be reached after a temperature change. The extended calibration (top) is given by equation 2-1 while calibrating at experimental conditions (bottom) gives equation 3-8.

would remain stable over a long enough period to make the procedure worthwhile. It was estimated that the entire extended calibration procedure would take approximately a month of continuous data collection to complete, in which time, the sample densities

could all have already been obtained for five temperatures in duplicate by calibrating at the experimental conditions. Finally, because the calibration is automated, outlined later in section 3.4, one can perform a calibration at an experimental temperature without the operator being present, *i.e.*, the calibration can be completed during the after-hours of the laboratory. This allows for sample density measurements to be conducted throughout the working-day hours for enhanced safety when working with high-pressure or toxic gases.

Finally, the extensive calibration requires that several of the parameters either be fitted using linear and nonlinear optimizations or estimated using the literature values of tube properties along with the tube dimensions.³² An isothermal calibration avoids the assumptions used in estimating the parameters and only requires the single least squares optimization for the pressure dependence, making for simple implementation.

3.4 Density Measurement

All densities were measured in an isothermal batches consisting of a calibration, four samples and then a final calibration (typically, calibration, mixture, mixture, solvent, solvent, calibration). The low-pressure N₂ reference time period was measured before and after the experimental batch to account for the instrument drift. Typically, pressures between $p = 2.5$ and 35 MPa (362 to 5076 psia) were measured at 2.5 MPa increments unless a two-phase region was being approached for a mixture. The syringe pump introduced the sample fluid into the well evacuated vibrating tube at the highest pressure to be measured (35 MPa), flushing through *ca.* 15 cm³ of the fluid before allowing one

hour of stabilization time. The automated measurement procedure, built into the custom LabVIEW software interfaced with the densimeter, was then initiated. The procedure consists of controlling the operation of the syringe pump, the protocol for data saving, and a list containing each of the targeted pressure set-points (in descending order) to be measured. Once the data for the initial pressure step has been saved, the data saving is turned off and the syringe pump is adjusted to the next target value in the pressure set-point list. This automated procedure was also used for both the H₂O calibration fluid to determine the $k_{T,p}$ and any sample fluids.

Pure CO₂ was delivered to the densimeter using a Chrom Tech SFC-24 liquid CO₂ pump. Unlike the syringe pumps, the supercritical CO₂ pump is unable to precisely control the pressure; therefore, the densimeter must be filled up to the highest pressure being measured and then reduced manually between measurements. The CO₂ is trapped inside the densimeter for measurements by having both the inlet and outlet valves closed, shown in Figure 8. Then, CO₂ is allowed to vent from the system by slightly opening the outlet valve, reducing the pressure. This manual control was also used for measurements where the internal syringe pump volume was fully extended.

Two of the four experimental runs per batch of experiments were targeted to measure the densities of the pure solvent with the remaining two measuring the sample mixtures. From these measurements, the apparent and partial molar volumes of the species can be calculated at each temperature and pressure. Measuring pure solvent, such as CO₂, also serves as a standard for testing the accuracy of the densimeter through comparison with

literature data using multi-parameter reduced Helmholtz equations-of-state such as the Span and Wagner equation-of-state for CO₂.⁸

3.5 Chemicals

Water used in making the mixtures and calibration procedure was obtained from an EMD Millipore model Milli-Q Type 1 Water Purification System that polishes H₂O to a resistance of 18 MΩ and was thoroughly degassed before each use. Oxygen-free N₂ (99.998%) and laser grade CO₂ (99.9995%) were purchased from Praxair Technologies Inc. and used as obtained after checking for impurities using gas chromatography. Mixtures were prepared gravimetrically inside 316L stainless steel Swagelok 500 cm³ vessels using a Mettler Toledo XP26003L mass comparator with 1 mg resolution.

Chapter Four: Volumetric Measurements of Water in Carbon Dioxide

4.1 Calculation of Volumetric Properties and the Krichevskii Parameter

The measurement of relative densities for calculation of apparent molar volumes for H₂O dissolved in CO₂ near infinite dilution is a novel use for this new vibrating tube densimeter, where these types of measurements have traditionally been confined to the aqueous phase. The densities of both the pure solvent, ρ^* , and the sample mixtures, ρ , were initially determined, as outlined in chapter three, using the relative density equation:

$$\rho^* - \rho_{ref} = k_{T,p} (\tau^2 - \tau_{ref}^2) \quad (4-1)$$

and

$$\rho - \rho_{ref} = k_{T,p} (\tau^2 - \tau_{ref}^2). \quad (4-2)$$

The apparent molar volumes were then calculated using the density difference, $\rho - \rho^*$, the molar mass of the solute (H₂O), M_2 , and the molality of the solution, m :

$$\bar{V}_{\phi,2} = \frac{M_2}{\rho} - \frac{1000(\rho - \rho^*)}{m\rho\rho^*}. \quad (4-3)$$

Ideally, one would like to measure apparent molar volumes at various concentrations and then extrapolate to infinite dilution; however, the saturation concentration for H₂O in CO₂ is small at these temperatures; therefore, we have assumed that the low concentration will approximate the infinite dilution case.

The density difference at undersaturated concentrations is expected to be very small, as shown in Figure 24, and thus provide a good demonstration for the utility of this sensitive densimeter. Also, the pure fluid densities can be compared to previously published literature data to assess the measurement accuracy; in this case, CO₂ density

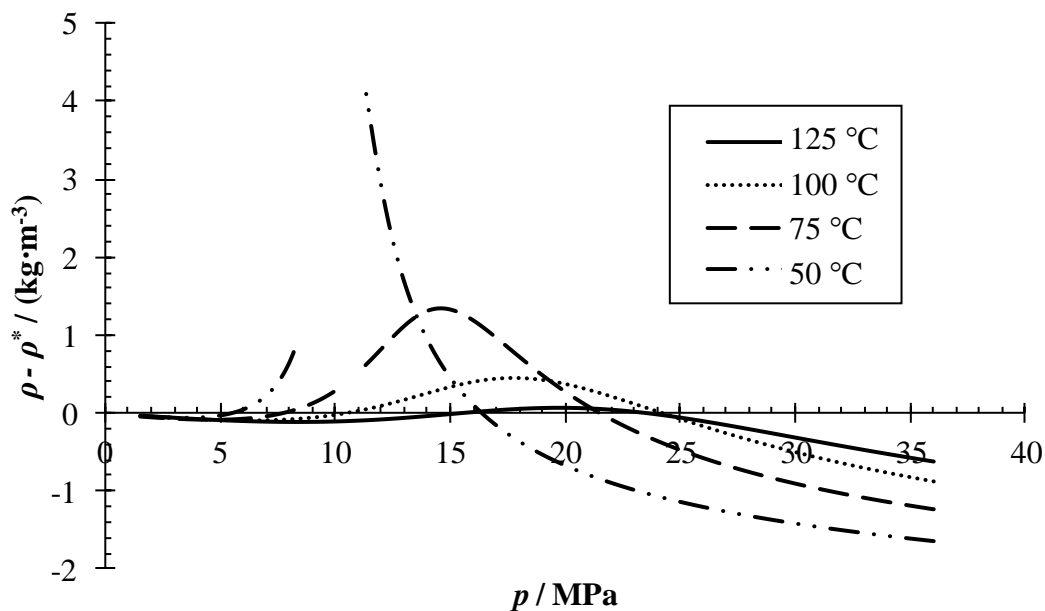


Figure 24. Calculated density difference between 0.2839% (0.06468 mol·kg⁻¹) H₂O in CO₂ and pure CO₂ at temperatures between $T = 50$ and 125 °C and pressures up to $p = 35$ MPa using the Span and Wagner,⁸ and Wagner and Pruß³⁶ equation-of-states with the Kunz and Wagner⁵³ mixing rules.

measurements can be compared to densities calculated by the semi-empirical reduced Helmholtz equation-of-state developed by Span and Wagner.⁸

Once the experimental apparent molar volumes at infinite dilution are obtained, the conversion to partial molar volumes at infinite dilution is straightforward. Writing the total volume, V , as a function of the pure solvent's molar volume, \bar{V}_1^* , and the solute's apparent molar volume, $\bar{V}_{\phi,2}$, gives

$$V = n_1 \bar{V}_1^* + n_2 \bar{V}_{\phi,2}. \quad (4-4)$$

The solute's partial molar volume is then the derivative of the volume with respect to the moles of solute, n_2 :

$$\left(\frac{\partial V}{\partial n_2}\right)_{T,p,n_1} = \bar{V}_2 = n_2 \left(\frac{\partial \bar{V}_{\phi,2}}{\partial n_2}\right)_{T,p,n_1} + \bar{V}_{\phi,2}. \quad (4-5)$$

As n_2 approaches zero at infinite dilution, the apparent molar volume becomes equivalent to the partial molar volume:

$$\bar{V}_2^\infty = \lim_{n_2 \rightarrow 0} \left(\frac{\partial V}{\partial n_2}\right)_{T,p,n_1} = \bar{V}_{\phi,2}. \quad (4-6)$$

Both the densities and partial molar volumes measured are used in the calculation of numerous other practical thermodynamic properties as outlined in the first chapter of this thesis.

Another property of interest that can be obtained from partial molar volumes is the Krichevskii parameter which represents the corresponding pressure change that occurs due to the addition of a small amount of solute at the critical point of the solvent (critical point parameters denoted with sub-script ‘‘c’’).^{54,55} The Krichevskii Parameter is defined as

$$A_{Kr} = \left(\frac{\partial p}{\partial x}\right)_{V_c, T_c, x=0}, \quad (4-7)$$

and can be calculated using a variety of methods, depending on available data, with one such method requiring partial molar volumes at infinite dilution.⁵⁵ The definition of a solute’s partial molar volume in a binary mixture is given by

$$\bar{V}_2 = \bar{V} - (1 - x_2) \left(\frac{\partial p}{\partial x_2}\right)_{T,V} \left(\frac{\partial \bar{V}}{\partial p}\right)_{T,x}. \quad (4-8)$$

At infinite dilution where x_2 approaches zero, the molar volume of the mixture, \bar{V} , approaches the pure solvent’s molar volume to produce equation 4-9:

$$\bar{V}_2^\infty = \bar{V}_1^* + \left(\frac{\partial p}{\partial x_2} \right)_{T,V} \left(\frac{\partial \bar{V}_1}{\partial p} \right)_{T,x}. \quad (4-9)$$

Equation 4-9 can then be further simplified using the pure solvent's isothermal compressibility, $\kappa_{T,1}$, and rearranged to

$$\left(\frac{\partial p}{\partial x_2} \right) = \frac{\bar{V}_2^\infty - \bar{V}_1^*}{\kappa_{T,1} \bar{V}_1^*}. \quad (4-10)$$

The values of $(\partial p / \partial x_2)$ at near-critical temperatures and pressures at low solute concentrations can then be plotted against the pure solvent density and fit with an empirical cubic function as was done previously in literature.⁵⁵ The value of the fitted function at the critical density of the solvent (467.6 kg·m⁻³ for CO₂)⁸ is then the A_{Kr} for the solute. The Krichevskii parameter can then be used in estimating the variation of several other properties in the near-critical region such as vapour-liquid distribution coefficients, Henry's constants, dew and bubble point curves, partial molar enthalpies, and partial molar heat capacities.^{55,56}

4.2 Results and Discussion

4.2.1 Relative Density Measurements

The relative density measurements obtained with the vibrating tube densimeter are outlined in Tables 7 and 8 for pure CO₂ and H₂O dissolved in CO₂, respectively.

Table 7. Relative density measurements for CO₂ at from $T = 45$ to 120 °C and $p = 2.5$ to 35 MPa.

$\frac{p}{\text{MPa}}$	$\frac{\rho}{(\text{kg}\cdot\text{m}^{-3})}$	$\frac{p}{\text{MPa}}$	$\frac{\rho}{(\text{kg}\cdot\text{m}^{-3})}$
$T = 45.125 \pm 0.005$ °C			
2.5076 ± 0.0001	46.79 ± 0.01	18.4100 ± 0.0010	793.67 ± 0.05
2.5105 ± 0.0002	46.85 ± 0.01	18.4595 ± 0.0010	794.37 ± 0.05
5.0206 ± 0.0003	109.19 ± 0.03	19.9602 ± 0.0016	811.60 ± 0.06
5.0512 ± 0.0004	110.15 ± 0.04	20.0101 ± 0.0010	812.21 ± 0.05
7.4730 ± 0.0008	205.98 ± 0.10	22.4668 ± 0.0017	835.94 ± 0.05
7.5129 ± 0.0005	208.24 ± 0.08	22.5073 ± 0.0015	836.37 ± 0.05
9.9719 ± 0.0005	489.84 ± 0.29	24.9232 ± 0.0027	856.01 ± 0.06
10.0057 ± 0.0005	495.36 ± 0.25	24.9781 ± 0.0017	856.44 ± 0.05
12.4704 ± 0.0007	674.85 ± 0.10	27.4656 ± 0.0020	873.99 ± 0.05
12.5061 ± 0.0007	676.30 ± 0.09	27.4814 ± 0.0023	874.08 ± 0.05
14.9733 ± 0.0008	740.57 ± 0.06	29.9712 ± 0.0017	889.67 ± 0.04
15.0109 ± 0.0008	741.41 ± 0.06	29.9933 ± 0.0016	889.75 ± 0.04
16.8599 ± 0.0013	772.70 ± 0.07	32.4735 ± 0.0017	903.72 ± 0.04
16.9004 ± 0.0009	773.39 ± 0.05	32.4756 ± 0.0017	903.70 ± 0.04
17.4611 ± 0.0012	781.27 ± 0.06	34.9834 ± 0.0018	916.52 ± 0.04
17.5108 ± 0.0009	782.05 ± 0.05	35.0130 ± 0.0018	916.69 ± 0.04
$T = 49.756 \pm 0.005$ °C			
2.5034 ± 0.0001	45.78 ± 0.01	12.5353 ± 0.0007	618.49 ± 0.11
2.5078 ± 0.0001	45.86 ± 0.01	12.5427 ± 0.0007	618.70 ± 0.10
4.9994 ± 0.0003	105.14 ± 0.02	15.0103 ± 0.0008	702.58 ± 0.07
5.0111 ± 0.0003	105.44 ± 0.02	15.0200 ± 0.0008	702.81 ± 0.07
7.5174 ± 0.0004	194.44 ± 0.03	17.5154 ± 0.0009	751.39 ± 0.06
7.5286 ± 0.0004	195.02 ± 0.04	17.5222 ± 0.0010	751.48 ± 0.06
10.0313 ± 0.0005	391.31 ± 0.15	20.0085 ± 0.0010	786.01 ± 0.05
10.0537 ± 0.0005	393.99 ± 0.16	20.0256 ± 0.0010	786.21 ± 0.06
12.5219 ± 0.0007	617.72 ± 0.11	22.4850 ± 0.0012	812.93 ± 0.05

Table 7. Continued

$\frac{p}{\text{MPa}}$	$\frac{\rho}{(\text{kg}\cdot\text{m}^{-3})}$	$\frac{p}{\text{MPa}}$	$\frac{\rho}{(\text{kg}\cdot\text{m}^{-3})}$
$T = 49.756 \pm 0.005 \text{ }^\circ\text{C}$			
22.4995 ± 0.0012	813.07 ± 0.05	30.0194 ± 0.0016	871.76 ± 0.05
24.9982 ± 0.0013	835.51 ± 0.05	32.5125 ± 0.0017	886.75 ± 0.05
25.0143 ± 0.0013	835.65 ± 0.05	32.5186 ± 0.0017	886.79 ± 0.05
27.4861 ± 0.0014	854.66 ± 0.05	34.9865 ± 0.0038	900.28 ± 0.07
27.5333 ± 0.0014	855.00 ± 0.05	35.0114 ± 0.0018	900.40 ± 0.05
30.0128 ± 0.0016	871.66 ± 0.05		
$T = 73.080 \pm 0.005 \text{ }^\circ\text{C}$			
2.4944 ± 0.0001	41.36 ± 0.01	20.0145 ± 0.0010	639.09 ± 0.06
2.5052 ± 0.0001	41.60 ± 0.01	20.0373 ± 0.0010	639.86 ± 0.07
5.0029 ± 0.0003	91.57 ± 0.01	22.4984 ± 0.0012	685.45 ± 0.05
5.0033 ± 0.0003	91.50 ± 0.01	22.5158 ± 0.0012	685.90 ± 0.05
7.5116 ± 0.0008	153.25 ± 0.03	24.9054 ± 0.0013	720.32 ± 0.05
7.5335 ± 0.0011	153.58 ± 0.04	25.0271 ± 0.0013	721.75 ± 0.04
10.0102 ± 0.0011	239.49 ± 0.10	27.5243 ± 0.0014	750.78 ± 0.04
10.0294 ± 0.0005	240.42 ± 0.04	27.5274 ± 0.0014	750.98 ± 0.04
12.4883 ± 0.0006	352.52 ± 0.08	30.0071 ± 0.0016	775.07 ± 0.04
12.5153 ± 0.0007	353.71 ± 0.08	30.0413 ± 0.0016	775.52 ± 0.04
15.0084 ± 0.0008	479.12 ± 0.10	32.5023 ± 0.0017	796.29 ± 0.04
15.0199 ± 0.0008	479.36 ± 0.08	32.5259 ± 0.0024	796.37 ± 0.05
17.5361 ± 0.0009	574.98 ± 0.07	35.0054 ± 0.0018	814.97 ± 0.04
17.5382 ± 0.0009	575.40 ± 0.07	35.0081 ± 0.0018	814.89 ± 0.04
$T = 73.576 \pm 0.005 \text{ }^\circ\text{C}$			
2.3907 ± 0.0001	39.64 ± 0.01	7.5118 ± 0.0011	152.19 ± 0.05
2.5073 ± 0.0001	41.59 ± 0.01	9.9953 ± 0.0005	237.48 ± 0.04
4.8435 ± 0.0003	87.83 ± 0.01	10.0099 ± 0.0005	238.02 ± 0.04
4.9681 ± 0.0003	90.53 ± 0.01	12.5190 ± 0.0007	351.04 ± 0.07
7.5087 ± 0.0009	152.27 ± 0.03	12.5632 ± 0.0007	353.04 ± 0.07

Table 7. Continued

$\frac{p}{\text{MPa}}$	$\frac{\rho}{(\text{kg}\cdot\text{m}^{-3})}$	$\frac{p}{\text{MPa}}$	$\frac{\rho}{(\text{kg}\cdot\text{m}^{-3})}$
$T = 73.576 \pm 0.005 \text{ }^\circ\text{C}$			
14.9311 ± 0.0008	471.38 ± 0.09	25.0241 ± 0.0013	719.36 ± 0.06
15.0031 ± 0.0008	474.51 ± 0.09	27.4982 ± 0.0014	748.34 ± 0.06
16.8867 ± 0.0011	549.97 ± 0.11	27.5247 ± 0.0014	748.64 ± 0.06
17.4502 ± 0.0009	568.71 ± 0.08	29.9773 ± 0.0016	772.84 ± 0.06
19.8406 ± 0.0010	632.10 ± 0.08	29.9862 ± 0.0016	772.93 ± 0.06
20.0702 ± 0.0010	637.28 ± 0.07	32.4007 ± 0.0017	793.57 ± 0.06
22.4433 ± 0.0012	681.88 ± 0.07	32.4584 ± 0.0017	793.99 ± 0.07
22.5068 ± 0.0012	682.81 ± 0.07	35.0047 ± 0.0018	813.16 ± 0.06
25.0091 ± 0.0015	719.09 ± 0.07	35.3217 ± 0.0018	815.32 ± 0.07
$T = 73.624 \pm 0.005 \text{ }^\circ\text{C}$			
2.4667 ± 0.0001	40.80 ± 0.02	17.5263 ± 0.0009	570.87 ± 0.08
2.4908 ± 0.0002	41.19 ± 0.03	19.9122 ± 0.0010	633.49 ± 0.08
4.9911 ± 0.0007	90.92 ± 0.02	20.0438 ± 0.0010	636.33 ± 0.08
4.9959 ± 0.0003	90.96 ± 0.02	22.3099 ± 0.0012	679.31 ± 0.07
7.5111 ± 0.0009	152.10 ± 0.04	22.5201 ± 0.0012	682.75 ± 0.07
7.5144 ± 0.0009	152.21 ± 0.04	24.9882 ± 0.0013	718.52 ± 0.07
9.9976 ± 0.0005	237.37 ± 0.04	25.0212 ± 0.0013	718.98 ± 0.07
9.9994 ± 0.0005	237.54 ± 0.04	27.4946 ± 0.0014	748.01 ± 0.06
12.4916 ± 0.0006	349.28 ± 0.07	30.0175 ± 0.0016	772.91 ± 0.06
12.5115 ± 0.0007	350.41 ± 0.08	32.4157 ± 0.0017	793.36 ± 0.06
15.0228 ± 0.0008	475.32 ± 0.09	34.6118 ± 0.0018	809.92 ± 0.07
15.0332 ± 0.0008	475.82 ± 0.10	34.9953 ± 0.0018	812.73 ± 0.07
17.3640 ± 0.0009	565.70 ± 0.08		
$T = 96.257 \pm 0.005 \text{ }^\circ\text{C}$			
2.2843 ± 0.0001	34.74 ± 0.01	5.1363 ± 0.0007	84.90 ± 0.03
2.5126 ± 0.0002	38.73 ± 0.01	7.4456 ± 0.0004	132.15 ± 0.02
5.0195 ± 0.0004	82.81 ± 0.03	7.8032 ± 0.0019	140.31 ± 0.10

Table 7. Continued

$\frac{p}{\text{MPa}}$	$\frac{\rho}{(\text{kg}\cdot\text{m}^{-3})}$	$\frac{p}{\text{MPa}}$	$\frac{\rho}{(\text{kg}\cdot\text{m}^{-3})}$
$T = 96.257 \pm 0.005 \text{ }^\circ\text{C}$			
10.0385 ± 0.0039	194.57 ± 0.24	22.5182 ± 0.0012	558.61 ± 0.06
10.1635 ± 0.0013	197.01 ± 0.07	25.0108 ± 0.0013	606.10 ± 0.05
12.5207 ± 0.0007	266.28 ± 0.04	25.3242 ± 0.0018	611.48 ± 0.08
12.5718 ± 0.0038	267.72 ± 0.27	27.4035 ± 0.0107	643.57 ± 0.33
15.0676 ± 0.0008	347.78 ± 0.06	27.5028 ± 0.0014	644.87 ± 0.05
15.3967 ± 0.0008	358.59 ± 0.07	30.0029 ± 0.0016	677.33 ± 0.05
17.5078 ± 0.0009	426.97 ± 0.06	30.1199 ± 0.0058	678.84 ± 0.17
17.7279 ± 0.0041	433.76 ± 0.28	32.3392 ± 0.0248	703.39 ± 0.59
20.0036 ± 0.0010	499.02 ± 0.06	32.6787 ± 0.0052	706.91 ± 0.14
20.0236 ± 0.0010	499.45 ± 0.07	35.0985 ± 0.0018	730.00 ± 0.04
22.5108 ± 0.0012	558.34 ± 0.06	35.4835 ± 0.0115	733.35 ± 0.22
$T = 119.891 \pm 0.005 \text{ }^\circ\text{C}$			
1.9596 ± 0.0001	27.33 ± 0.01	15.3396 ± 0.0008	288.92 ± 0.11
2.4858 ± 0.0002	35.27 ± 0.03	17.4253 ± 0.0009	339.78 ± 0.13
5.0146 ± 0.0003	74.80 ± 0.03	20.3809 ± 0.0011	410.12 ± 0.15
5.0278 ± 0.0003	75.31 ± 0.03	22.6272 ± 0.0012	459.27 ± 0.17
7.4700 ± 0.0004	117.88 ± 0.04	25.3893 ± 0.0013	512.82 ± 0.19
7.6455 ± 0.0004	121.51 ± 0.05	27.8856 ± 0.0015	554.61 ± 0.21
10.0411 ± 0.0005	166.71 ± 0.06	27.8904 ± 0.0015	554.73 ± 0.21
10.0642 ± 0.0005	169.07 ± 0.06	30.4400 ± 0.0016	591.56 ± 0.22
12.4873 ± 0.0006	221.26 ± 0.08	32.9258 ± 0.0021	622.87 ± 0.23
12.5940 ± 0.0007	224.10 ± 0.09	35.5611 ± 0.0018	651.90 ± 0.24
15.0568 ± 0.0008	282.41 ± 0.11		

Table 8. Relative density measurements and partial molar volumes of H₂O in CO₂ from $T = 45$ to 120 °C and $p = 2.5$ to 35 MPa.

$\frac{p}{\text{MPa}}$	$\frac{\rho}{(\text{kg}\cdot\text{m}^{-3})}$	$\frac{\Delta\rho}{(\text{kg}\cdot\text{m}^{-3})}$	$\frac{\bar{V}_2^\infty}{(\text{cm}^3\cdot\text{mol}^{-1})}$
$T = 45.129 \pm 0.005$ °C			
$m = 0.05325 \pm 0.00092$ mol·kg ⁻¹			
9.9890 ± 0.0008	498.45 ± 0.35	5.78	-406.01 ± 49.35
9.9927 ± 0.0009	499.44 ± 0.39	6.17	-434.51 ± 52.82
12.5109 ± 0.0009	678.80 ± 0.11	2.42	-72.51 ± 14.24
12.5137 ± 0.0016	679.01 ± 0.15	2.53	-77.01 ± 16.11
15.0130 ± 0.0017	742.96 ± 0.09	1.48	-26.09 ± 10.89
15.0156 ± 0.0024	743.08 ± 0.12	1.55	-28.67 ± 11.86
17.5046 ± 0.0009	783.08 ± 0.05	1.20	-13.72 ± 8.39
17.5058 ± 0.0027	783.21 ± 0.10	1.32	-17.37 ± 9.85
20.0023 ± 0.0014	813.13 ± 0.06	1.08	-8.49 ± 7.79
20.0063 ± 0.0010	813.07 ± 0.05	0.97	-5.38 ± 7.51
22.4685 ± 0.0012	836.88 ± 0.04	0.85	-1.25 ± 6.93
22.4883 ± 0.0028	836.95 ± 0.07	0.74	1.59 ± 7.60
24.9507 ± 0.0013	856.98 ± 0.04	0.69	3.35 ± 6.46
24.9695 ± 0.0017	857.06 ± 0.05	0.63	4.86 ± 6.62
27.4914 ± 0.0019	874.81 ± 0.05	0.63	5.02 ± 6.38
27.5087 ± 0.0034	874.88 ± 0.07	0.60	5.96 ± 6.77
30.0001 ± 0.0025	890.43 ± 0.05	0.66	4.47 ± 6.22
30.0053 ± 0.0016	890.38 ± 0.04	0.58	6.38 ± 5.88
32.4902 ± 0.0031	904.36 ± 0.05	0.63	5.52 ± 6.05
32.4933 ± 0.0024	904.28 ± 0.05	0.53	7.65 ± 5.88
35.0308 ± 0.0018	917.30 ± 0.04	0.49	8.80 ± 5.47
35.0344 ± 0.0018	917.22 ± 0.04	0.39	10.96 ± 5.48

Table 8. Continued

$\frac{p}{\text{MPa}}$	$\frac{\rho}{(\text{kg}\cdot\text{m}^{-3})}$	$\frac{\Delta\rho}{(\text{kg}\cdot\text{m}^{-3})}$	$\frac{\bar{V}_2^\infty}{(\text{cm}^3\cdot\text{mol}^{-1})}$
$T = 49.754 \pm 0.005 \text{ }^\circ\text{C}$			
$m = 0.06468 \pm 0.00057 \text{ mol}\cdot\text{kg}^{-1}$			
10.0233 ± 0.0005	394.72 ± 0.15	4.37	-393.16 ± 39.09
10.0560 ± 0.0005	398.16 ± 0.16	3.90	-338.69 ± 38.73
12.5055 ± 0.0007	620.56 ± 0.11	3.86	-126.71 ± 13.77
12.5364 ± 0.0007	621.74 ± 0.11	3.48	-110.79 ± 13.59
15.0054 ± 0.0008	704.42 ± 0.07	2.18	-42.63 ± 9.11
15.0114 ± 0.0008	704.76 ± 0.07	2.38	-48.69 ± 9.16
17.4990 ± 0.0009	752.63 ± 0.06	1.27	-10.77 ± 7.38
17.5334 ± 0.0009	753.35 ± 0.06	1.44	-15.43 ± 7.41
20.0156 ± 0.0010	787.31 ± 0.06	1.19	-6.90 ± 6.70
20.0191 ± 0.0010	787.47 ± 0.05	1.31	-9.77 ± 6.62
22.5316 ± 0.0012	814.42 ± 0.05	1.14	-4.46 ± 6.11
22.5321 ± 0.0012	814.49 ± 0.05	1.20	-5.89 ± 6.15
25.0263 ± 0.0013	836.65 ± 0.05	0.99	-0.27 ± 5.69
25.0439 ± 0.0019	836.81 ± 0.06	1.00	-0.65 ± 5.92
27.5315 ± 0.0014	855.80 ± 0.05	0.82	3.75 ± 5.39
27.5498 ± 0.0014	855.87 ± 0.05	0.75	5.14 ± 5.38
30.0530 ± 0.0016	872.70 ± 0.05	0.66	7.20 ± 5.13
30.0700 ± 0.0016	872.77 ± 0.05	0.63	7.79 ± 5.13
32.5282 ± 0.0017	887.50 ± 0.05	0.58	8.87 ± 5.01
32.5693 ± 0.0017	887.74 ± 0.05	0.59	8.68 ± 4.93
35.0004 ± 0.0018	900.90 ± 0.05	0.63	7.96 ± 4.81
35.0462 ± 0.0018	901.14 ± 0.05	0.64	7.86 ± 4.79
$T = 73.086 \pm 0.005 \text{ }^\circ\text{C}$			
$m = 0.06468 \pm 0.00057 \text{ mol}\cdot\text{kg}^{-1}$			
2.5004 ± 0.0002	41.49 ± 0.01	0.00	461.15 ± 1854.05
2.5046 ± 0.0002	41.54 ± 0.01	-0.06	1000.22 ± 1848.00

Table 8. Continued

$\frac{p}{\text{MPa}}$	$\frac{\rho}{(\text{kg}\cdot\text{m}^{-3})}$	$\frac{\Delta\rho}{(\text{kg}\cdot\text{m}^{-3})}$	$\frac{\bar{V}_2^\infty}{(\text{cm}^3\cdot\text{mol}^{-1})}$
$T = 73.086 \pm 0.005 \text{ }^\circ\text{C}$			
$m = 0.06468 \pm 0.00057 \text{ mol}\cdot\text{kg}^{-1}$			
5.0091 ± 0.0009	91.61 ± 0.04	-0.06	307.18 ± 450.01
5.0210 ± 0.0003	91.91 ± 0.01	0.00	198.91 ± 382.98
7.5124 ± 0.0005	153.20 ± 0.02	-0.05	152.94 ± 146.24
10.0220 ± 0.0005	240.20 ± 0.04	0.23	13.73 ± 64.21
10.0234 ± 0.0005	240.16 ± 0.05	0.13	40.23 ± 66.11
12.4277 ± 0.0006	350.16 ± 0.06	0.58	-21.68 ± 34.13
12.4325 ± 0.0006	350.39 ± 0.07	0.57	-20.76 ± 34.71
12.4365 ± 0.0006	350.58 ± 0.07	0.57	-20.10 ± 34.16
12.4557 ± 0.0009	351.50 ± 0.11	0.55	-18.10 ± 40.08
12.5022 ± 0.0007	353.96 ± 0.08	0.73	-39.77 ± 35.19
14.9990 ± 0.0008	479.98 ± 0.09	1.41	-57.04 ± 20.20
15.0124 ± 0.0008	480.38 ± 0.11	1.20	-42.80 ± 21.26
17.4967 ± 0.0009	575.26 ± 0.07	1.35	-31.69 ± 13.11
17.5111 ± 0.0009	575.61 ± 0.08	1.25	-27.14 ± 13.50
20.0057 ± 0.0010	640.02 ± 0.06	1.03	-10.75 ± 10.11
20.0191 ± 0.0010	640.33 ± 0.07	1.05	-11.42 ± 10.46
22.5032 ± 0.0012	686.44 ± 0.06	0.80	-0.17 ± 8.62
22.5147 ± 0.0012	686.68 ± 0.05	0.86	-1.94 ± 8.59
25.0083 ± 0.0013	722.35 ± 0.05	0.74	2.88 ± 7.53
25.0192 ± 0.0014	722.55 ± 0.06	0.80	1.26 ± 7.81
27.5053 ± 0.0014	751.33 ± 0.05	0.68	5.42 ± 6.98
27.5128 ± 0.0014	751.48 ± 0.04	0.75	3.31 ± 6.86
30.0061 ± 0.0016	775.71 ± 0.04	0.59	7.94 ± 6.34
30.0128 ± 0.0024	775.84 ± 0.06	0.66	6.26 ± 6.89
32.4997 ± 0.0017	796.76 ± 0.04	0.53	9.60 ± 6.03
32.5013 ± 0.0017	796.72 ± 0.04	0.49	10.73 ± 5.90
35.0236 ± 0.0035	815.51 ± 0.06	0.47	11.27 ± 6.24

Table 8. Continued

$\frac{p}{\text{MPa}}$	$\frac{\rho}{(\text{kg}\cdot\text{m}^{-3})}$	$\frac{\Delta\rho}{(\text{kg}\cdot\text{m}^{-3})}$	$\frac{\bar{V}_2^\infty}{(\text{cm}^3\cdot\text{mol}^{-1})}$
$T = 73.086 \pm 0.005 \text{ }^\circ\text{C}$			
$m = 0.06468 \pm 0.00057 \text{ mol}\cdot\text{kg}^{-1}$			
35.0249 ± 0.0018	815.42 ± 0.04	0.36	13.68 ± 5.55
$T = 73.570 \pm 0.005 \text{ }^\circ\text{C}$			
$m = 0.06597 \pm 0.00068 \text{ mol}\cdot\text{kg}^{-1}$			
2.1084 ± 0.0001	34.53 ± 0.01	-0.24	3533.47 ± 2605.22
4.9583 ± 0.0003	90.32 ± 0.01	-0.18	531.57 ± 393.44
5.0038 ± 0.0003	91.34 ± 0.02	-0.19	540.82 ± 408.24
7.5519 ± 0.0013	153.23 ± 0.04	-0.05	150.75 ± 158.31
7.6132 ± 0.0010	154.71 ± 0.04	-0.26	278.90 ± 151.14
10.0063 ± 0.0010	238.25 ± 0.10	0.42	-36.37 ± 81.67
10.0148 ± 0.0005	238.62 ± 0.05	0.45	-45.71 ± 67.11
12.5067 ± 0.0007	351.57 ± 0.08	1.10	-83.70 ± 35.75
12.5239 ± 0.0007	352.45 ± 0.09	1.12	-86.34 ± 36.73
14.9911 ± 0.0008	476.26 ± 0.09	2.15	-106.63 ± 21.03
15.0185 ± 0.0008	477.40 ± 0.09	2.05	-99.01 ± 20.54
17.4817 ± 0.0009	571.70 ± 0.11	2.16	-69.03 ± 15.57
17.5347 ± 0.0016	573.30 ± 0.14	2.10	-65.56 ± 16.62
20.0271 ± 0.0011	638.01 ± 0.09	1.65	-33.37 ± 11.35
22.3949 ± 0.0012	682.42 ± 0.07	1.31	-16.21 ± 9.16
25.0048 ± 0.0013	720.26 ± 0.07	1.26	-11.98 ± 8.17
25.0075 ± 0.0028	720.35 ± 0.11	1.32	-13.59 ± 9.33
27.5129 ± 0.0014	749.60 ± 0.06	1.17	-7.68 ± 7.45
27.5313 ± 0.0014	749.73 ± 0.06	1.11	-5.88 ± 7.46
30.0008 ± 0.0016	773.97 ± 0.06	0.89	0.80 ± 6.89
30.0016 ± 0.0016	774.03 ± 0.06	0.94	-0.59 ± 6.91
32.4891 ± 0.0017	795.06 ± 0.06	0.70	5.94 ± 6.48
32.4957 ± 0.0018	795.17 ± 0.07	0.76	4.36 ± 6.68

Table 8. Continued

$\frac{p}{\text{MPa}}$	$\frac{\rho}{(\text{kg}\cdot\text{m}^{-3})}$	$\frac{\Delta\rho}{(\text{kg}\cdot\text{m}^{-3})}$	$\frac{\bar{V}_2^\infty}{(\text{cm}^3\cdot\text{mol}^{-1})}$
$T = 73.570 \pm 0.005 \text{ }^\circ\text{C}$			
$m = 0.06597 \pm 0.00068 \text{ mol}\cdot\text{kg}^{-1}$			
35.0199 ± 0.0018	813.96 ± 0.06	0.75	4.84 ± 6.20
35.0217 ± 0.0018	814.05 ± 0.06	0.83	3.02 ± 6.24
$T = 73.626 \pm 0.005 \text{ }^\circ\text{C}$			
$m = 0.06597 \pm 0.00068 \text{ mol}\cdot\text{kg}^{-1}$			
2.4798 ± 0.0001	41.06 ± 0.02	-0.24	2571.72 ± 1944.13
2.4956 ± 0.0001	41.27 ± 0.02	-0.07	1093.11 ± 1923.23
4.9721 ± 0.0003	90.54 ± 0.02	-0.07	330.75 ± 412.18
7.5098 ± 0.0012	152.16 ± 0.04	0.12	41.93 ± 161.19
7.6110 ± 0.0013	154.54 ± 0.05	-0.44	392.61 ± 160.67
9.9953 ± 0.0005	237.78 ± 0.04	0.42	-36.03 ± 66.32
10.0004 ± 0.0005	237.94 ± 0.05	0.40	-31.71 ± 69.30
15.0217 ± 0.0008	477.42 ± 0.10	1.91	-90.12 ± 21.33
17.3701 ± 0.0009	568.06 ± 0.08	2.07	-66.11 ± 14.24
17.5048 ± 0.0009	571.92 ± 0.08	1.65	-45.40 ± 13.85
20.0438 ± 0.0010	638.21 ± 0.07	1.49	-27.25 ± 10.72
22.3094 ± 0.0012	680.92 ± 0.07	1.22	-13.56 ± 9.36
22.4649 ± 0.0012	683.45 ± 0.07	1.19	-12.35 ± 9.10
25.0240 ± 0.0013	720.41 ± 0.07	1.17	-9.18 ± 8.15
25.0518 ± 0.0013	720.76 ± 0.07	1.15	-8.69 ± 8.13
27.4670 ± 0.0014	748.97 ± 0.07	1.04	-4.00 ± 7.58
27.5064 ± 0.0014	749.37 ± 0.06	1.02	-3.44 ± 7.44
29.1721 ± 0.0015	766.16 ± 0.07	0.87	0.91 ± 7.14
29.9936 ± 0.0016	773.81 ± 0.06	0.79	3.21 ± 6.91
32.3593 ± 0.0017	793.94 ± 0.06	0.62	7.69 ± 6.51
32.4365 ± 0.0017	794.55 ± 0.07	0.61	8.01 ± 6.53
34.8809 ± 0.0018	812.93 ± 0.06	0.70	6.17 ± 6.24

Table 8. Continued

$\frac{p}{\text{MPa}}$	$\frac{\rho}{(\text{kg}\cdot\text{m}^{-3})}$	$\frac{\Delta\rho}{(\text{kg}\cdot\text{m}^{-3})}$	$\frac{\bar{V}_2^\infty}{(\text{cm}^3\cdot\text{mol}^{-1})}$
$T = 73.626 \pm 0.005 \text{ }^\circ\text{C}$			
$m = 0.06597 \pm 0.00068 \text{ mol}\cdot\text{kg}^{-1}$			
35.0654 ± 0.0023	814.20 ± 0.07	0.68	6.45 ± 6.38
$T = 96.256 \pm 0.005 \text{ }^\circ\text{C}$			
$m = 0.06468 \pm 0.00057 \text{ mol}\cdot\text{kg}^{-1}$			
2.5057 ± 0.0001	38.26 ± 0.01	-0.13	1792.80 ± 2196.22
2.5079 ± 0.0001	38.40 ± 0.01	-0.02	667.48 ± 2210.29
5.0085 ± 0.0003	82.15 ± 0.02	-0.39	1098.34 ± 497.67
5.0093 ± 0.0004	82.28 ± 0.02	-0.27	838.34 ± 500.10
7.4458 ± 0.0004	131.89 ± 0.01	-0.26	367.52 ± 190.91
7.4996 ± 0.0004	132.75 ± 0.01	-0.67	720.71 ± 190.86
10.0150 ± 0.0005	193.18 ± 0.02	-0.32	224.83 ± 93.36
10.0256 ± 0.0022	194.28 ± 0.14	0.50	-112.59 ± 140.60
10.6745 ± 0.0006	211.90 ± 0.03	0.38	-47.63 ± 81.57
12.4020 ± 0.0006	262.47 ± 0.04	-0.05	80.67 ± 54.76
12.4482 ± 0.0006	263.93 ± 0.05	-0.02	71.86 ± 56.10
14.9373 ± 0.0008	343.84 ± 0.06	0.29	14.39 ± 34.40
14.9801 ± 0.0008	345.18 ± 0.05	0.23	22.71 ± 32.54
17.4549 ± 0.0009	426.01 ± 0.07	0.78	-23.86 ± 23.94
17.4929 ± 0.0009	427.15 ± 0.07	0.71	-18.34 ± 23.15
19.9818 ± 0.0010	499.25 ± 0.07	0.81	-14.28 ± 17.00
19.9961 ± 0.0010	499.57 ± 0.07	0.77	-11.81 ± 17.11
22.4875 ± 0.0012	558.75 ± 0.06	0.79	-7.04 ± 13.39
22.5108 ± 0.0012	559.20 ± 0.06	0.75	-4.69 ± 13.35
24.9987 ± 0.0013	606.67 ± 0.06	0.83	-5.01 ± 11.34
24.9992 ± 0.0016	606.66 ± 0.08	0.80	-3.99 ± 11.88
27.5073 ± 0.0016	645.63 ± 0.07	0.67	3.16 ± 10.15
27.5112 ± 0.0014	645.69 ± 0.06	0.68	2.69 ± 9.78

Table 8. Continued

$\frac{p}{\text{MPa}}$	$\frac{\rho}{(\text{kg}\cdot\text{m}^{-3})}$	$\frac{\Delta\rho}{(\text{kg}\cdot\text{m}^{-3})}$	$\frac{\bar{V}_2^\infty}{(\text{cm}^3\cdot\text{mol}^{-1})}$
$T = 96.256 \pm 0.005 \text{ }^\circ\text{C}$			
$m = 0.06468 \pm 0.00057 \text{ mol}\cdot\text{kg}^{-1}$			
30.0118 ± 0.0019	678.12 ± 0.07	0.58	7.19 ± 9.34
30.0136 ± 0.0030	678.08 ± 0.09	0.51	9.28 ± 10.01
32.5101 ± 0.0022	705.66 ± 0.06	0.47	11.05 ± 8.31
32.5187 ± 0.0022	705.69 ± 0.07	0.42	12.63 ± 8.41
35.0171 ± 0.0022	729.64 ± 0.06	0.45	11.48 ± 7.61
35.0247 ± 0.0020	729.77 ± 0.05	0.52	9.57 ± 7.53
$T = 96.263 \pm 0.005 \text{ }^\circ\text{C}$			
$m = 0.13384 \pm 0.00104 \text{ mol}\cdot\text{kg}^{-1}$			
2.5120 ± 0.0001	38.46 ± 0.01	-0.27	1825.39 ± 1049.11
2.7040 ± 0.0001	41.60 ± 0.01	-0.19	1267.49 ± 897.93
5.0079 ± 0.0003	82.13 ± 0.01	-0.47	736.25 ± 232.65
5.2008 ± 0.0003	85.81 ± 0.01	-0.25	461.11 ± 211.74
7.4396 ± 0.0006	131.36 ± 0.03	-0.65	415.53 ± 102.39
7.6313 ± 0.0004	135.41 ± 0.03	-1.03	549.46 ± 95.45
9.9371 ± 0.0005	191.98 ± 0.03	0.54	-16.73 ± 46.74
10.1256 ± 0.0005	197.12 ± 0.03	0.66	-36.81 ± 44.62
12.4451 ± 0.0006	263.64 ± 0.04	-0.20	90.29 ± 26.14
12.6517 ± 0.0007	269.89 ± 0.04	-0.36	103.72 ± 24.63
14.9651 ± 0.0008	344.79 ± 0.06	0.33	31.41 ± 16.39
15.1868 ± 0.0008	351.86 ± 0.07	0.15	42.44 ± 16.25
17.4785 ± 0.0009	426.84 ± 0.07	0.86	6.76 ± 11.24
17.7144 ± 0.0009	434.02 ± 0.06	0.63	16.29 ± 10.59
19.9886 ± 0.0010	499.44 ± 0.06	0.83	11.24 ± 8.06
20.2423 ± 0.0011	506.20 ± 0.06	0.98	6.87 ± 7.86
22.4989 ± 0.0012	559.01 ± 0.06	0.81	12.87 ± 6.44
22.7649 ± 0.0012	564.92 ± 0.06	1.16	4.78 ± 6.27

Table 8. Continued

$\frac{p}{\text{MPa}}$	$\frac{\rho}{(\text{kg}\cdot\text{m}^{-3})}$	$\frac{\Delta\rho}{(\text{kg}\cdot\text{m}^{-3})}$	$\frac{\bar{V}_2^\infty}{(\text{cm}^3\cdot\text{mol}^{-1})}$
$T = 96.263 \pm 0.005 \text{ }^\circ\text{C}$			
$m = 0.13384 \pm 0.00104 \text{ mol}\cdot\text{kg}^{-1}$			
25.0045 ± 0.0014	606.76 ± 0.07	0.81	13.13 ± 5.53
25.2847 ± 0.0013	611.94 ± 0.06	1.24	4.60 ± 5.30
27.5110 ± 0.0014	645.70 ± 0.06	0.69	15.52 ± 4.70
27.8030 ± 0.0014	650.21 ± 0.05	1.10	8.27 ± 4.66
30.0156 ± 0.0016	678.14 ± 0.06	0.55	17.62 ± 4.22
30.3218 ± 0.0018	682.20 ± 0.06	1.00	10.41 ± 4.28
32.5079 ± 0.0028	705.68 ± 0.08	0.52	17.79 ± 4.19
32.5094 ± 0.0032	705.69 ± 0.08	0.51	17.88 ± 4.30
32.8346 ± 0.0029	709.41 ± 0.08	0.92	11.69 ± 4.23
35.0076 ± 0.0032	730.05 ± 0.08	0.96	11.26 ± 3.97
35.0109 ± 0.0025	729.66 ± 0.06	0.53	17.29 ± 3.73
$T = 119.874 \pm 0.005 \text{ }^\circ\text{C}$			
$m = 0.13384 \pm 0.00104 \text{ mol}\cdot\text{kg}^{-1}$			
2.3636 ± 0.0001	33.54 ± 0.02	-0.36	2898.10 ± 1443.04
2.3651 ± 0.0005	33.37 ± 0.02	-0.55	4145.56 ± 1479.40
5.2823 ± 0.0003	79.34 ± 0.03	-0.29	574.62 ± 277.93
5.2826 ± 0.0003	79.47 ± 0.03	-0.17	429.46 ± 276.86
7.5128 ± 0.0004	118.91 ± 0.05	0.10	96.64 ± 131.10
7.5136 ± 0.0004	118.55 ± 0.05	-0.28	298.40 ± 131.68
10.2814 ± 0.0005	172.35 ± 0.07	-0.34	190.43 ± 142.84
10.3375 ± 0.0005	172.98 ± 0.07	-0.89	325.39 ± 142.24
12.6537 ± 0.0007	226.13 ± 0.09	0.91	-53.33 ± 58.11
12.7271 ± 0.0007	227.67 ± 0.09	0.74	-27.67 ± 57.58
15.2004 ± 0.0008	286.02 ± 0.11	0.22	43.17 ± 28.68
15.2348 ± 0.0008	286.88 ± 0.12	0.25	40.50 ± 28.80
16.8228 ± 0.0009	325.80 ± 0.13	0.69	6.59 ± 23.58

Table 8. Continued

$\frac{p}{\text{MPa}}$	$\frac{\rho}{(\text{kg}\cdot\text{m}^{-3})}$	$\frac{\Delta\rho}{(\text{kg}\cdot\text{m}^{-3})}$	$\frac{\bar{V}_2^\infty}{(\text{cm}^3\cdot\text{mol}^{-1})}$
$T = 119.874 \pm 0.005 \text{ }^\circ\text{C}$			
$m = 0.13384 \pm 0.00104 \text{ mol}\cdot\text{kg}^{-1}$			
17.7266 ± 0.0009	348.00 ± 0.14	1.03	-11.98 ± 21.66
20.2068 ± 0.0011	407.28 ± 0.16	1.23	-11.20 ± 16.65
20.2108 ± 0.0011	407.44 ± 0.16	1.29	-13.88 ± 16.88
22.1726 ± 0.0014	451.11 ± 0.19	1.20	-4.25 ± 14.67
22.6947 ± 0.0012	462.16 ± 0.18	1.30	-6.55 ± 13.73
25.1685 ± 0.0013	510.51 ± 0.20	1.67	-12.61 ± 11.88
27.6487 ± 0.0014	552.61 ± 0.21	1.73	-9.92 ± 10.43
30.1239 ± 0.0018	588.98 ± 0.23	1.56	-3.04 ± 9.47
32.5939 ± 0.0017	620.59 ± 0.24	1.39	1.91 ± 8.67
35.0656 ± 0.0018	648.42 ± 0.24	1.48	1.50 ± 8.09
35.0794 ± 0.0025	648.37 ± 0.25	1.29	4.86 ± 8.19

Errors for the relative densities, $\delta\rho$, were estimated by combining the direct measurement error, δ_m , with the error caused by temperature and pressure deviations, δ_{TP} ,

$$\delta\rho = \sqrt{\delta_m^2 + \delta_{TP}^2}. \quad (4-11)$$

The measurement error was calculated using a propagation of error for the relative density equation (equation 3-8):

$$\delta_m = \sqrt{[\delta k_{T,p} (\tau^2 - \tau_{ref}^2)]^2 + [2k_{T,p} \delta\tau]^2 + [2k_{T,p} \delta\tau_{ref}]^2}, \quad (4-12)$$

while the error in density caused by pressure and temperature deviations at each experimental condition was estimated using multi-parameter reduced-Helmholtz equations-of-state, $\rho_{EOS}(T,p)$:^{8,36,53}

$$\delta_{TP} = \frac{\rho_{EOS}(T - \delta T, p + \delta p) - \rho_{EOS}(T + \delta T, p - \delta p)}{2}. \quad (4-13)$$

As is shown in Tables 7 and 8 (as well as Figure 27), the errors are predictably larger in the near-critical region where small changes in temperature or pressure cause large changes in density and also at higher pressures due to increasing error in the pressure measurement from the deadweight calibration (see section 3.2). In general, the errors in the density measurements were an order of magnitude smaller than what is typical of a commercial high-pressure vibrating tube densimeter.⁵²

The general behaviour of the densities, over the pressure and temperature range studied, appear to agree with predictions using existing literature data from reduced Helmholtz multi-parameter equations of state as shown in Figures 25 and 26; however, relative deviation plots must be used in order to properly evaluate the accuracy of the densimeter. Comparison of the measured CO₂ densities to calculated Span and Wagner⁸ values (used as the baseline) in Figure 27 shows that the densities measured with the newly constructed vibrating tube densimeter are in good agreement with the predicted literature values with some larger deviations being observed in the near-critical region, caused by temperature and pressure deviations having an increased affect on the densities.

Repeated measurements carried out around $T = 73.6$ °C in two separate blocks of experiments were within experimental errors and also in agreement with measurements completed months earlier at $T = 73.086$ °C when compared on a relative deviation plot. Thus, the densimeter is stable over time with the measurement and calibration procedures in place (described in sub-sections 3.3 and 3.4) and the data obtained are reliable.

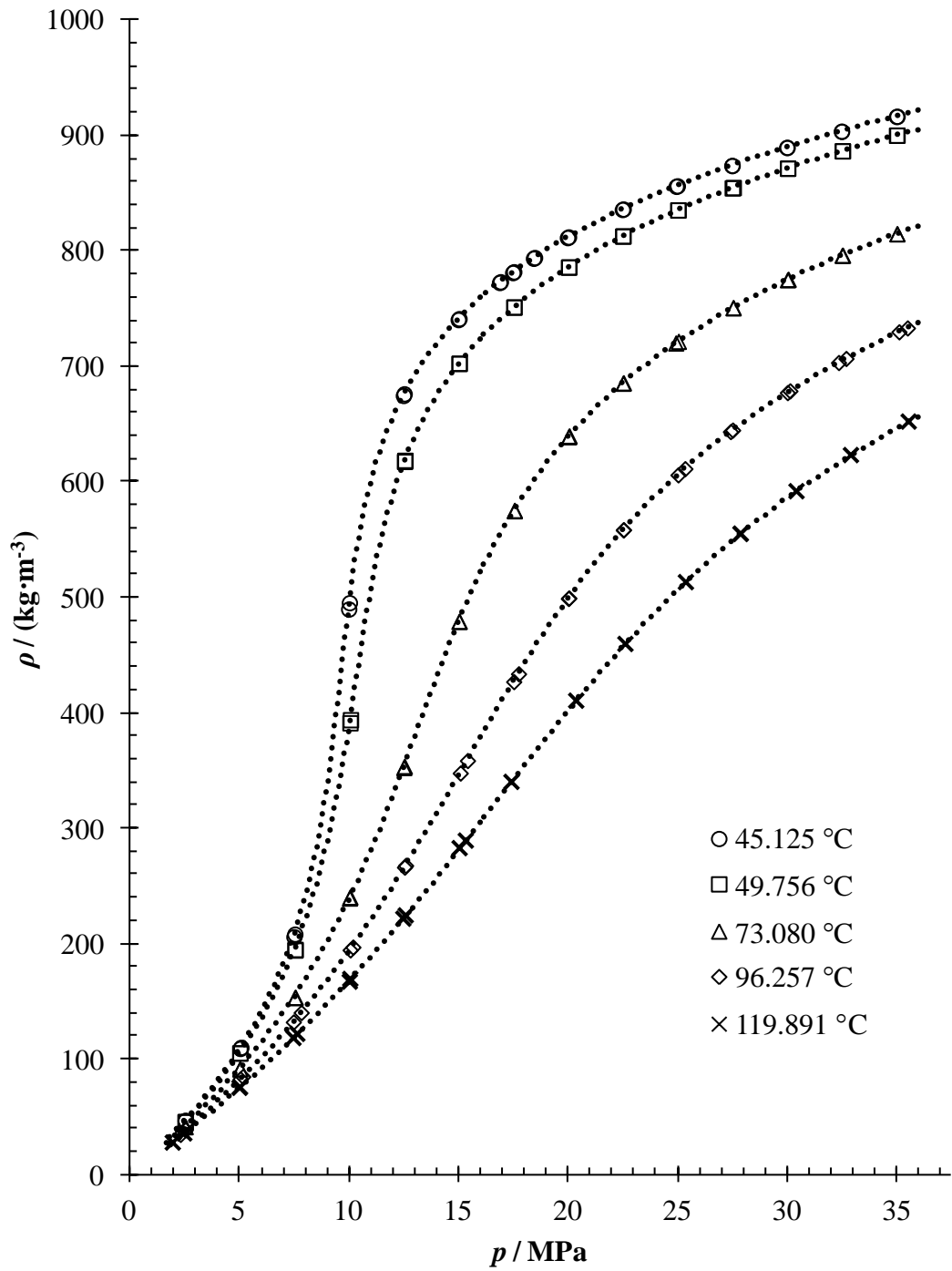


Figure 25. Measured CO₂ densities at experimental temperatures and pressures. Calculated densities from the Span and Wagner equation-of-state⁸ represented by dotted lines.

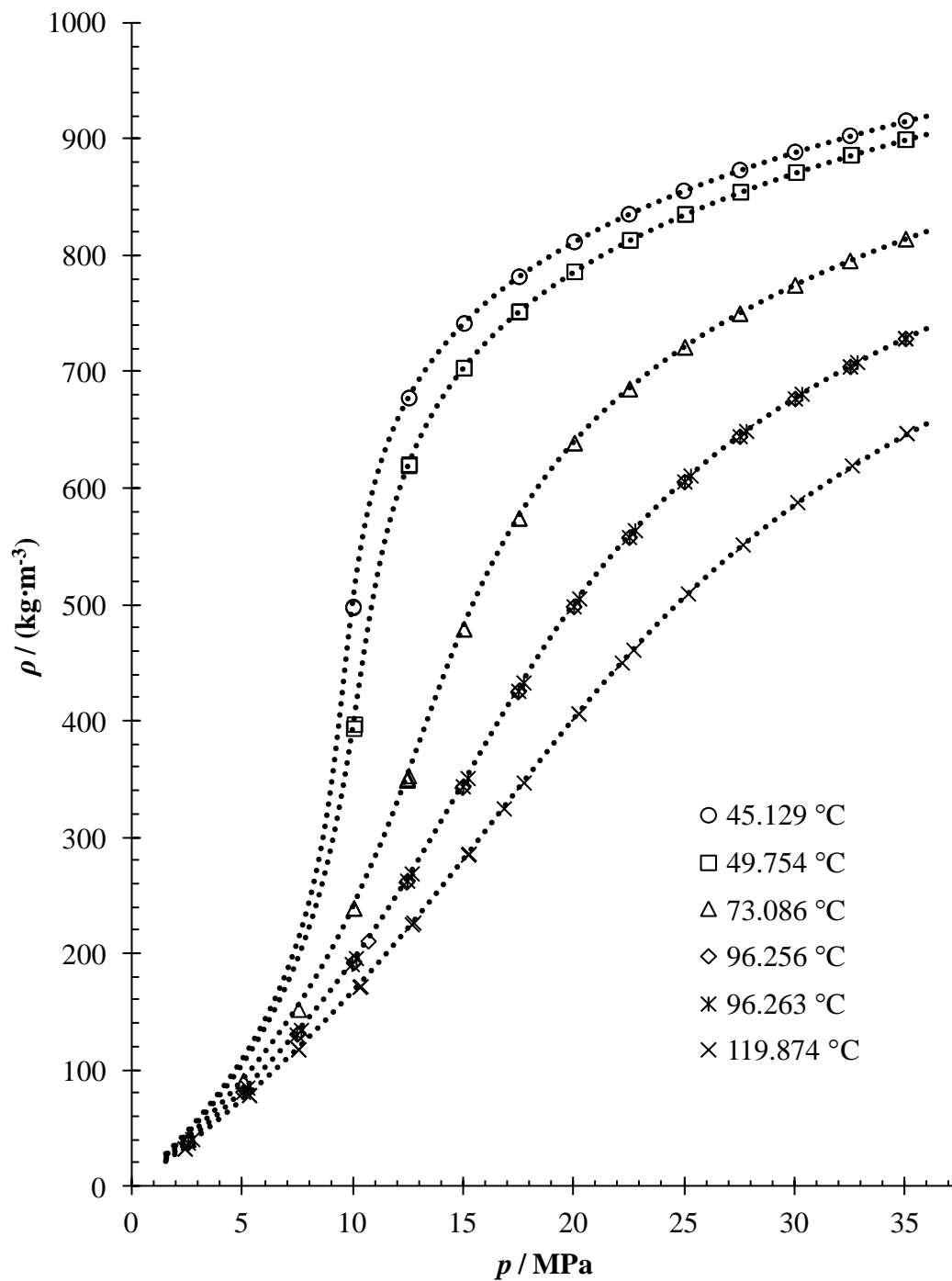


Figure 26. Measured densities for H₂O dissolved in CO₂ at experimental temperatures and pressures. Experimental concentrations were: ○, 0.05325 mol·kg⁻¹; □, △, ◇, 0.06468 mol·kg⁻¹; *, ×, 0.13384 mol·kg⁻¹. Calculated densities from the Span and Wagner,⁸ and Wagner and Pruß³⁶ equation-of-states with the Kunz and Wagner⁵³ mixing rules are represented by dotted lines.

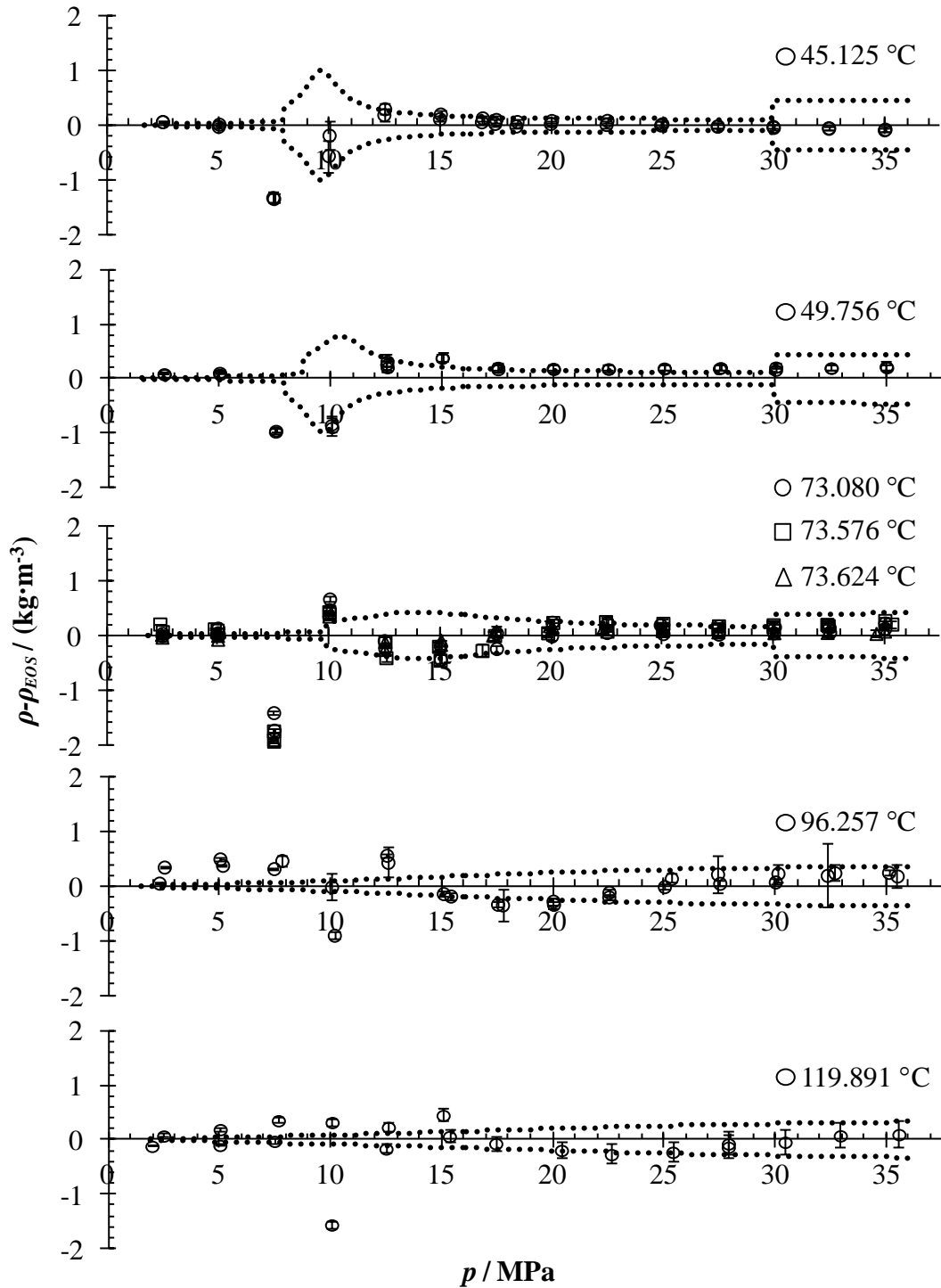


Figure 27. Relative deviation plot comparing measured densities against calculated equation-of-state densities at experimental temperatures and pressures. Listed density error for the Span and Wagner8 equation-of-state at each temperature represented by the dotted lines.

4.2.2 Partial Molar Volumes of Water in Carbon Dioxide

The density differences were used to calculate apparent and partial molar volumes for the H₂O at infinite dilution as outlined in section 4.1, with the partial molar volumes being reported in Table 8 within sub-section 4.2.1. Errors for the partial molar volumes were calculated using standard propagation of error:

$$\delta\bar{V}_2 = \sqrt{\left[\left(M_2 - \frac{1000}{b}\right)\left(\frac{\delta\rho}{\rho^2}\right)\right]^2 + \left[\left(\frac{1000}{b}\right)\left(\frac{\delta\rho^*}{\rho^{*2}}\right)\right]^2 + \left[\left(\frac{1000(\rho - \rho^*)}{\rho\rho^*}\right)\left(\frac{\delta m}{m^2}\right)\right]^2} \quad (4-14)$$

The error increased from less than 10 cm³·mol⁻¹ at higher pressures up to a few thousand cm³·mol⁻¹ at low densities due to each of the error terms being inversely proportional to some form of ρ^2 meaning small changes in density result in large volume changes. Partial molar volumes are plotted for each temperature in Figures 28 to 31.

In order to check the infinite dilution assumption in calculating the partial molar volumes with equation 4-6, the partial molar volumes of H₂O dissolved into CO₂ at two different concentrations were measured across similar temperatures and pressures. Figure 31, compares the partial molar volumes of $m = 0.06468$ mol·kg⁻¹ and 0.13384 mol·kg⁻¹ H₂O mixtures at $T = 96.26$ °C. The two data show very good overlap, within the experimental errors over all pressures measured, *i.e.*, there is no observable concentration dependence. Thus, the assumption that the mixtures measured are approximating an infinite dilution appears robust.

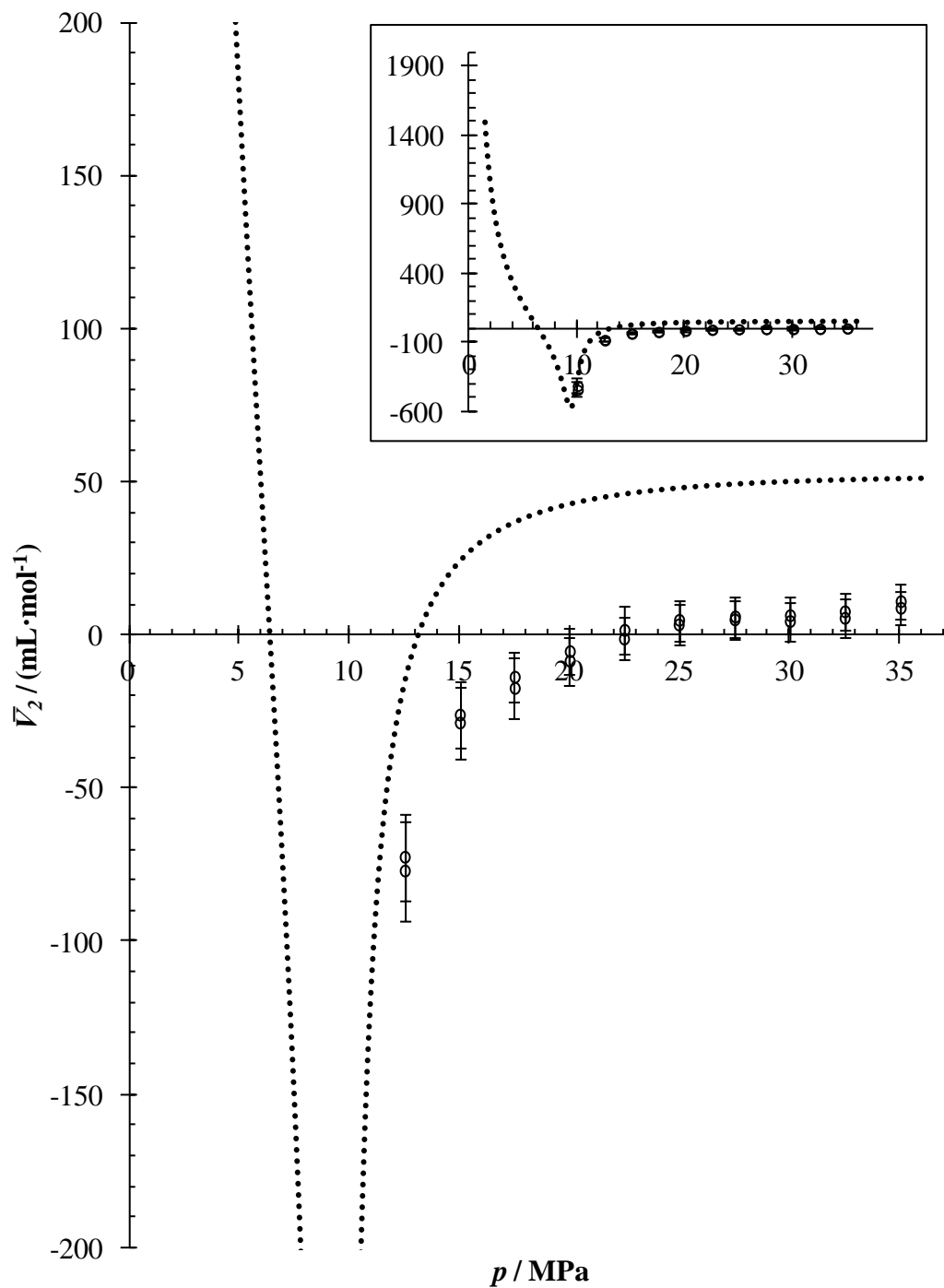


Figure 28. Partial molar volumes of H₂O in CO₂, with figure inset showing the full plot, at $T = 45.130\text{ °C}$ and $m = 0.05325\text{ mol}\cdot\text{kg}^{-1}$. Partial molar volumes calculated using the Span and Wagner,⁸ and Wagner and Pruß³⁶ equation-of-states with the Kunz and Wagner⁵³ mixing rules being represented by the dotted lines.

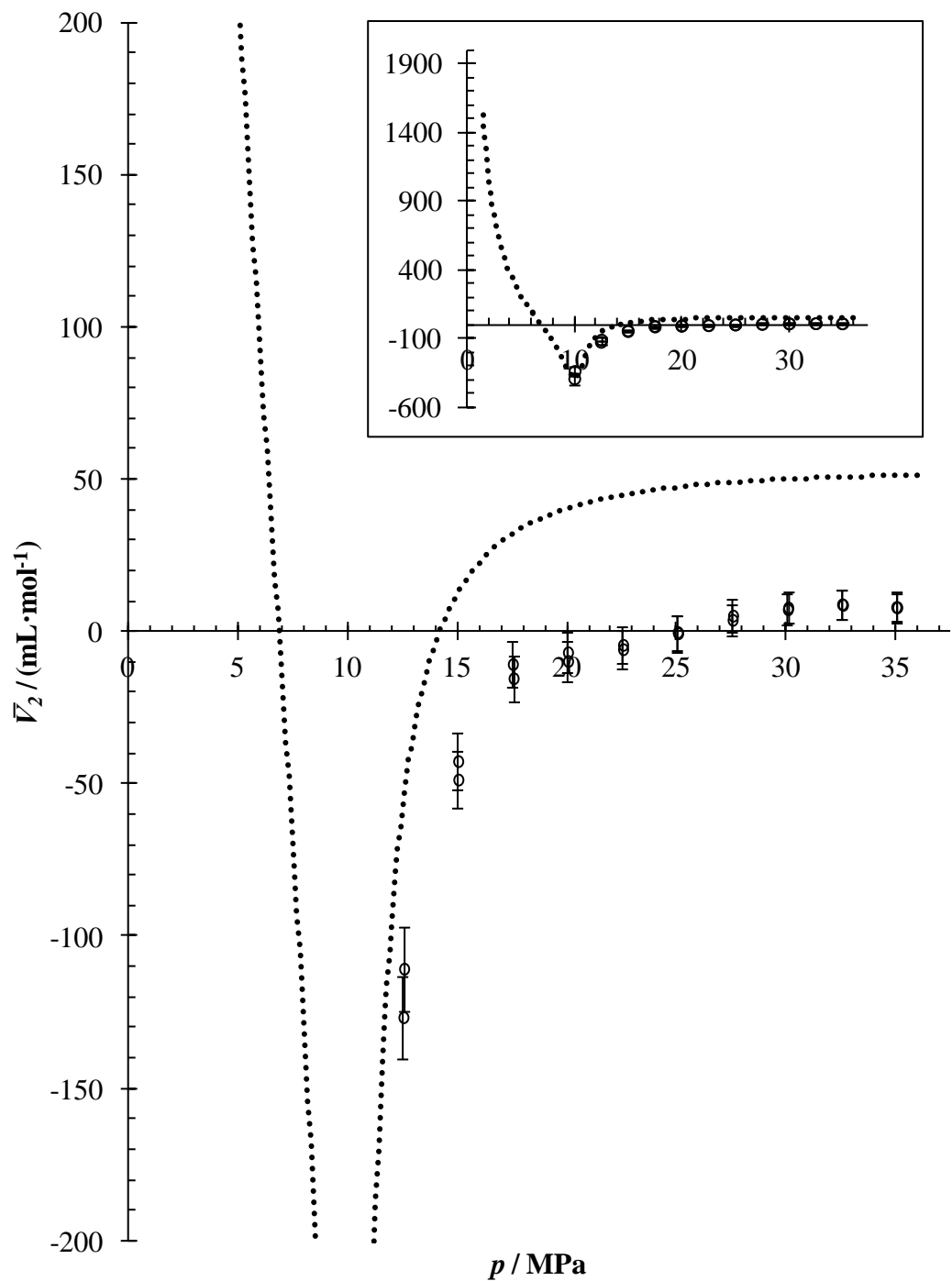


Figure 29. Partial molar volumes of H₂O in CO₂, with figure inset showing the full plot, at $T = 49.754$ °C and $m = 0.06468$ mol·kg⁻¹. Partial molar volumes calculated using the Span and Wagner,⁸ and Wagner and Pruß³⁶ equation-of-states with the Kunz and Wagner⁵³ mixing rules being represented by the dotted line.

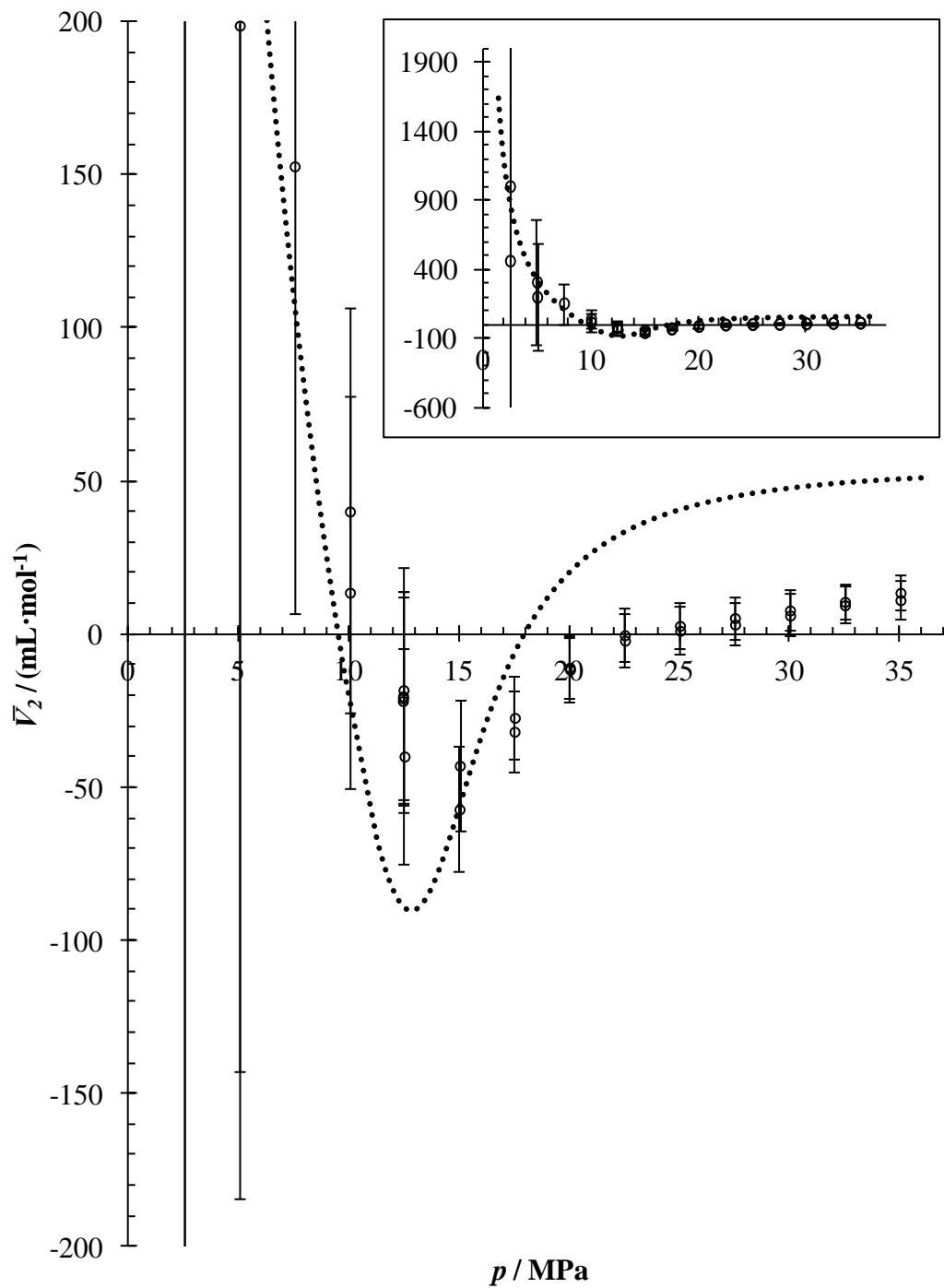


Figure 30. Partial molar volumes of H₂O in CO₂, with figure inset showing the full plot, at $T = 73.086$ °C and $m = 0.06468$ mol·kg⁻¹. Partial molar volumes calculated using the Span and Wagner,⁸ and Wagner and Pruß³⁶ equation-of-states with the Kunz and Wagner⁵³ mixing rules being represented by the dotted line.

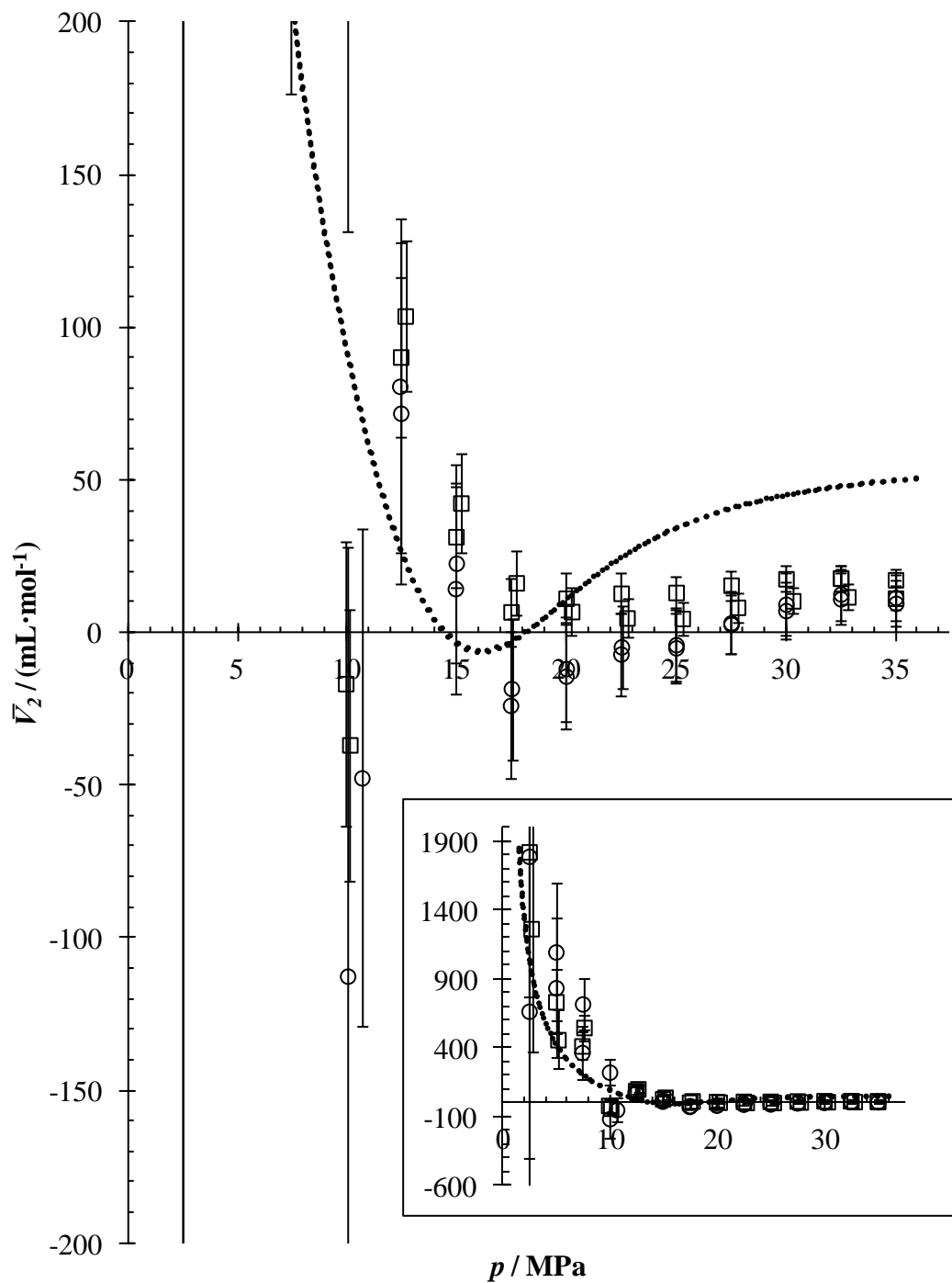


Figure 31. The effect of concentration on partial molar volumes of H₂O in CO₂ at: O, $T = 96.256 \text{ }^\circ\text{C}$ and $m = 0.06468 \text{ mol} \cdot \text{kg}^{-1}$; and \square , $T = 96.263 \text{ }^\circ\text{C}$ and $m = 0.13384 \text{ mol} \cdot \text{kg}^{-1}$. The calculated partial molar volumes by the Span and Wagner⁸, and Wagner and Prue³⁶ equation-of-states with the Kunz and Wagner⁵³ mixing rules are represented by the dotted lines.

Comparing the partial molar volumes of H₂O in Figures 28 through 32, some general trends can be identified: (1) at low-pressures and for each temperature, the partial molar volumes of H₂O trends towards infinity and becomes difficult to measure accurately as expected;⁵⁷ (2) at increasing pressures, the partial molar volumes of H₂O at each temperature appear to approach a similar value between 10 and 20 cm³·mol⁻¹; and, (3) the inflection in water's partial molar volume at near-critical pressures occurs at less-negative volumes and higher pressures as the temperature is increased. Smaller pressures could not be obtained for $T = 45\text{ °C}$ and 49 °C to demonstrate the full extent of the inflection as they fell below the predicted H₂O dew-point⁵⁸ pressures for both of these systems. It appears that the partial molar volume at $T = 45\text{ °C}$ is decreasing more significantly at pressures between $p = 12.5$ and 10 MPa , suggesting the inflection occurs at a more-negative value than the inflection at $T = 49\text{ °C}$.

Although the general shapes of the calculated partial molar volumes from the equations-of-state are comparable to the experimental data, the actual values are quite shifted: (1) the inflection in the partial molar volume, observed near the critical pressure of CO₂, occurs at different volumes and pressures, and (2) at increasing pressures, the partial molar volumes of H₂O appear to approach a significantly higher constant value at approximately 50 cm³·mol⁻¹. The mixing parameters for the Helmholtz equations-of-state used in predicting all previously mentioned densities and partial molar volumes are empirical functions that have not been calibrated for this system. Although there is an abundance of pure species data for both H₂O³⁶ and CO₂,⁸ there is very little data for the binary mixture at low H₂O concentrations (as discussed in section 1.2) leading to

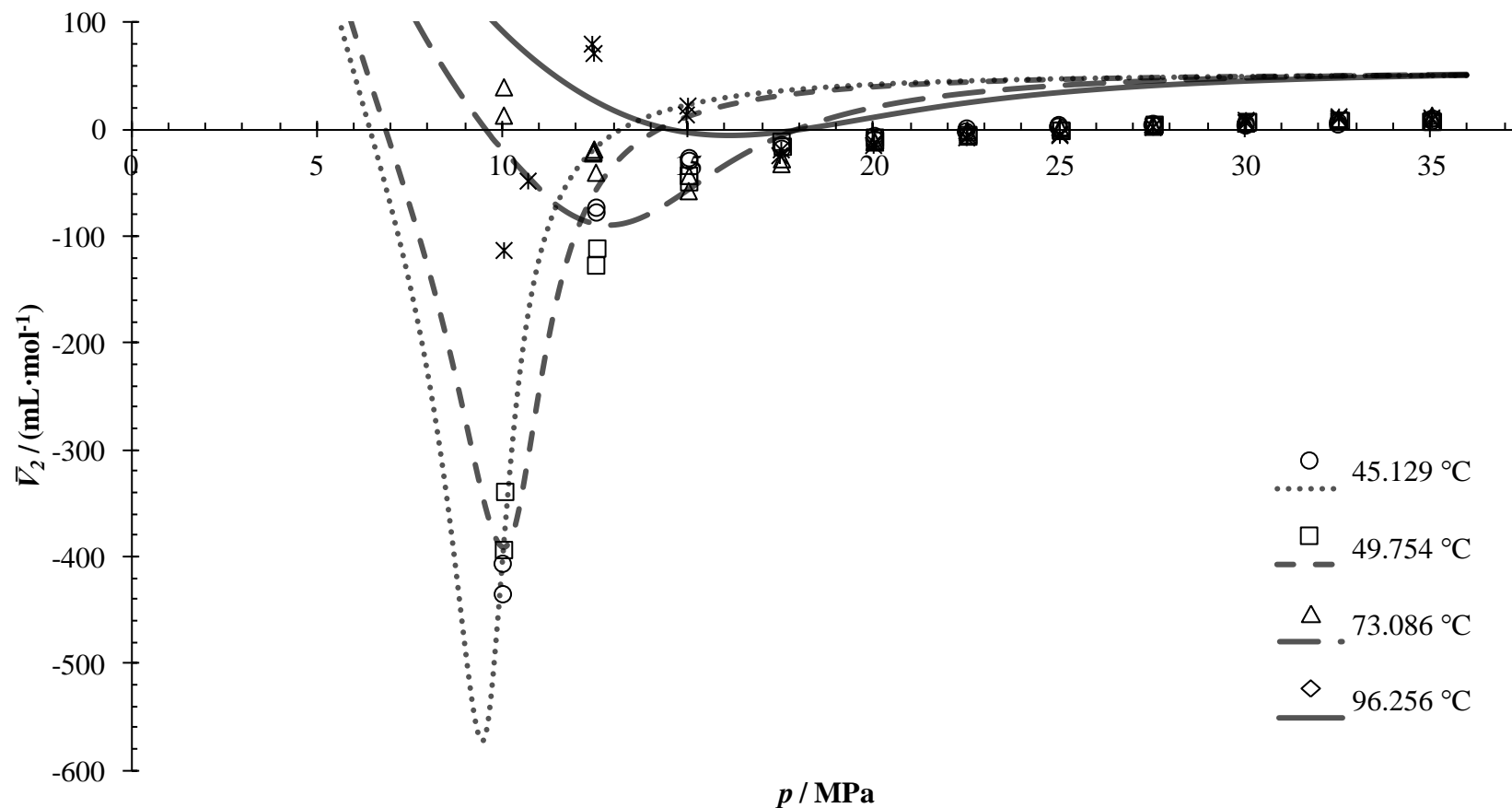


Figure 32. Overlaid partial molar volumes of H₂O in CO₂ for the experimental pressure range at different temperatures. Error bars and the lower-pressure measurements have been omitted for clarity (see Figures 28 to 30). Markers and continuous lines indicate experimental measurements and calculated Span and Wagner,⁸ and Wagner and Pruß³⁶ equation-of-states with the Kunz and Wagner⁵³ mixing rules values respectively.

inaccuracies in predicting the properties of such mixtures.

4.2.3 Krichevskii Parameter

The previously measured densities and partial molar volumes of H₂O in CO₂ allow for the evaluation of the Krichevskii parameter, A_{Kr} , in order to determine how the critical pressure of CO₂ changes when small amounts of H₂O are added at critical conditions.

In order to properly ascertain A_{Kr} , the effect of temperature on $(\partial p / \partial x_{H_2O})$ was determined to ensure the experimental data used were sufficiently close to the critical temperature of CO₂ (30.978 °C).⁸ A temperature dependence on $(\partial p / \partial x_2)$ was not observed for several solutes close to their solvent's critical point⁵⁵ and this was also found to be the case for H₂O in CO₂. Figure 33 shows that near the critical density of CO₂ (467.6 kg·m⁻³)⁸ only $(\partial p / \partial x_{H_2O})$ at $T = 119.874$ °C deviates to more negative values from the other $(\partial p / \partial x_{H_2O})$ data at lower temperatures (closer to the critical temperature of CO₂). This trend continues with higher temperatures as $(\partial p / \partial x_{H_2O})$ calculated from volumetric data at $T = 400$ °C obtained by Seitz and Blencoe²⁵ deviates to even more negative values. As a result, these two higher temperature data sets were not used in determining A_{Kr} .

The data obtained by Zhang *et al.*¹⁴ at $T = 35$ °C does not match the data from this work or the other literature data in Figure 34 and was also not used in determining A_{Kr} . As the data at lower densities are very close to the predicted water dew-point pressure for their

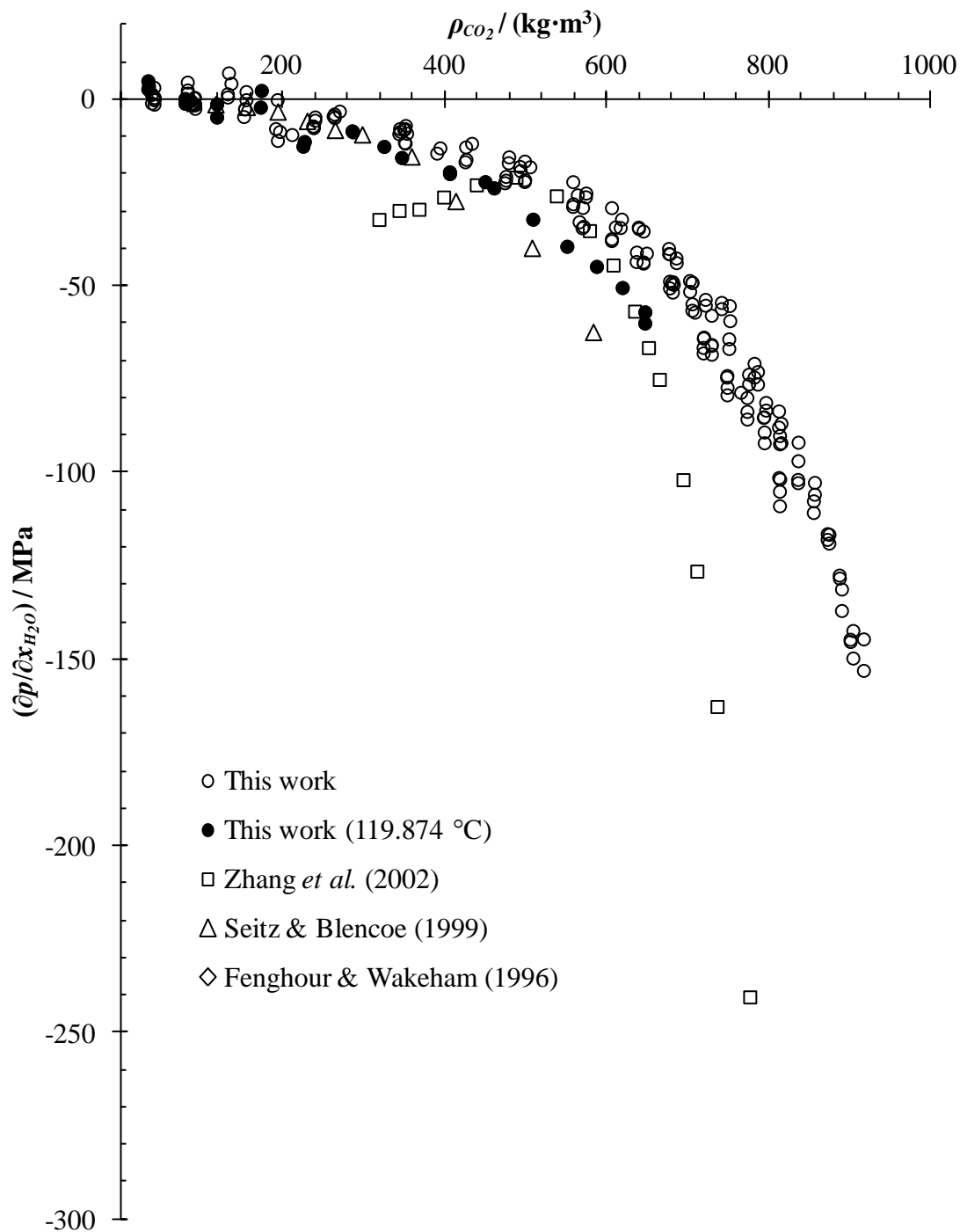


Figure 33. A plot of $(\partial p / \partial x_{H_2O})$ against the solvent density for H_2O in CO_2 using all of the data in this work and literature data below concentrations of $x_{H_2O} = 0.2$. Zhang *et al.*¹⁴ conducted their measurements at $T = 35$ °C, Fenghour and Wakeham²⁰ between $T = 142$ to 425 °C, and Seitz and Blencoe²⁵ at $T = 400$ °C. Densities were calculated by the Span and Wagner equation-of-state⁸ when experimental CO_2 density measurements were not provided by the authors.

system ($p = 7.61$ MPa),⁵⁸ it is possible that the inflection in $(\partial p / \partial x_{H_2O})$ observed just under $\rho_{CO_2} = 500$ kg·m⁻³ was caused by a change in the water content of their sample.

The differences observed at larger densities data can also be removed through the use of a small volume correction to the size of the author's isochoric measurement cell (the addition of 0.2 cm³ will completely overlap the data sets up to 700 kg·m⁻³). This could be a result of the authors not calibrating the cell volume for expansion at higher pressures and temperatures. Isochoric cell volumes are normally calibrated across all experimental conditions, in order to obtain accurate density measurements.

Table 9 includes all the data used in calculating the Krichevskii parameter as outlined in section 4.1. The isothermal compressibilities of the pure CO₂, $\kappa_{T,1}$, were calculated using the Span and Wagner equation-of-state.⁸ After excluding the data obtained at higher temperatures, data chosen also was within a range of approximately $\rho_{c,l} \pm 200$ kg·m⁻³ (250-650 kg·m⁻³). This is a commonly used range for near-critical data selection when determining A_{Kr} through volumetric measurements.⁵⁵

The $(\partial p / \partial x_{H_2O})$ derivatives and solvent densities of the selected data given in Table 9 were then plotted in Figure 34 and fit with a cubic equation. Solving the cubic equation at the critical density of the solvent, $\rho_{CO_2} = 467.6$ kg·m⁻³,⁸ yielded a Krichevskii parameter of $A_{Kr} = -17.7 \pm 3.0$ MPa. The stated error for A_{Kr} was the 95% standard error from the linest least squares analysis.

Table 9. Near-critical data (approximately within 200 kg·m⁻³ of the solvent's critical density) selected for Krichevskii parameter determination.⁸

ρ^* (kg·m ⁻³)	\bar{V}_2^∞ (cm ³ ·mol ⁻¹)	\bar{V}_1^* (cm ³ ·mol ⁻¹)	$\kappa_{T,1}$ (cm ³ ·mol ⁻¹)	$\frac{\partial p}{\partial \chi_{H_2O}}$ MPa
262.52	80.67	167.64	0.11672	-4.4
263.85	90.29	166.80	0.11639	-3.9
263.95	71.86	166.74	0.11638	-4.9
270.25	103.72	162.84	0.11482	-3.2
343.55	14.39	128.10	0.09643	-9.2
344.46	31.41	127.76	0.09618	-7.8
344.95	22.71	127.58	0.09605	-8.6
349.58	-21.68	125.89	0.14599	-8.0
349.82	-20.76	125.81	0.14593	-8.0
350.01	-20.10	125.74	0.14587	-8.0
350.47	-83.70	125.57	0.14408	-11.6
350.95	-18.10	125.40	0.14560	-7.9
351.33	-86.34	125.26	0.14384	-11.7
351.71	42.44	125.13	0.09424	-7.0
353.23	-39.77	124.59	0.14496	-9.1
390.35	-393.16	112.74	0.31130	-14.4
394.26	-338.69	111.62	0.31028	-13.0
425.24	-23.86	103.49	0.07353	-16.7
425.98	6.76	103.31	0.07331	-12.7
426.44	-18.34	103.20	0.07318	-16.1
433.39	16.29	101.55	0.07119	-11.8
474.11	-106.63	92.83	0.09615	-22.3
475.35	-99.01	92.58	0.09558	-21.7
475.50	-90.12	92.55	0.09558	-20.7
478.57	-57.04	91.96	0.09537	-17.0
479.19	-42.80	91.84	0.09508	-15.4
492.67	-406.01	89.33	0.30837	-18.0
493.27	-434.51	89.22	0.30719	-19.1
498.44	-14.28	88.29	0.05276	-22.0

Table 9. Continued.

ρ^* (kg·m ⁻³)	\bar{V}_2^∞ (cm ³ ·mol ⁻¹)	\bar{V}_1^* (cm ³ ·mol ⁻¹)	$\kappa_{T,1}$ (cm ³ ·mol ⁻¹)	$\frac{\partial p}{\partial \chi_{H_2O}}$ MPa
498.61	11.24	88.26	0.05271	-16.6
498.80	-11.81	88.23	0.05266	-21.5
505.22	6.87	87.11	0.05095	-18.1
557.96	-7.04	78.88	0.03797	-28.7
558.20	12.87	78.84	0.03792	-22.1
558.45	-4.69	78.81	0.03786	-28.0
563.77	4.78	78.06	0.03668	-25.6
565.99	-66.11	77.76	0.05643	-32.8
569.54	-69.03	77.27	0.05502	-34.4
570.26	-45.40	77.17	0.05484	-29.0
571.20	-65.56	77.05	0.05440	-34.0
573.92	-31.69	76.68	0.05411	-26.1
574.36	-27.14	76.62	0.05393	-25.1
605.85	-5.01	72.64	0.02825	-37.8
605.86	-3.99	72.64	0.02825	-37.3
605.95	13.13	72.63	0.02824	-29.0
610.70	4.60	72.06	0.02739	-34.2
616.71	-126.71	71.36	0.08080	-34.4
618.26	-110.79	71.18	0.07966	-32.1
636.36	-33.37	69.16	0.03411	-43.5
636.73	-27.25	69.12	0.03407	-40.9
638.99	-10.75	68.87	0.03376	-34.2
639.28	-11.42	68.84	0.03368	-34.6
644.96	3.16	68.24	0.02190	-43.6
645.01	15.52	68.23	0.02189	-35.3
645.01	2.69	68.23	0.02189	-43.9
649.11	8.27	67.80	0.02131	-41.2

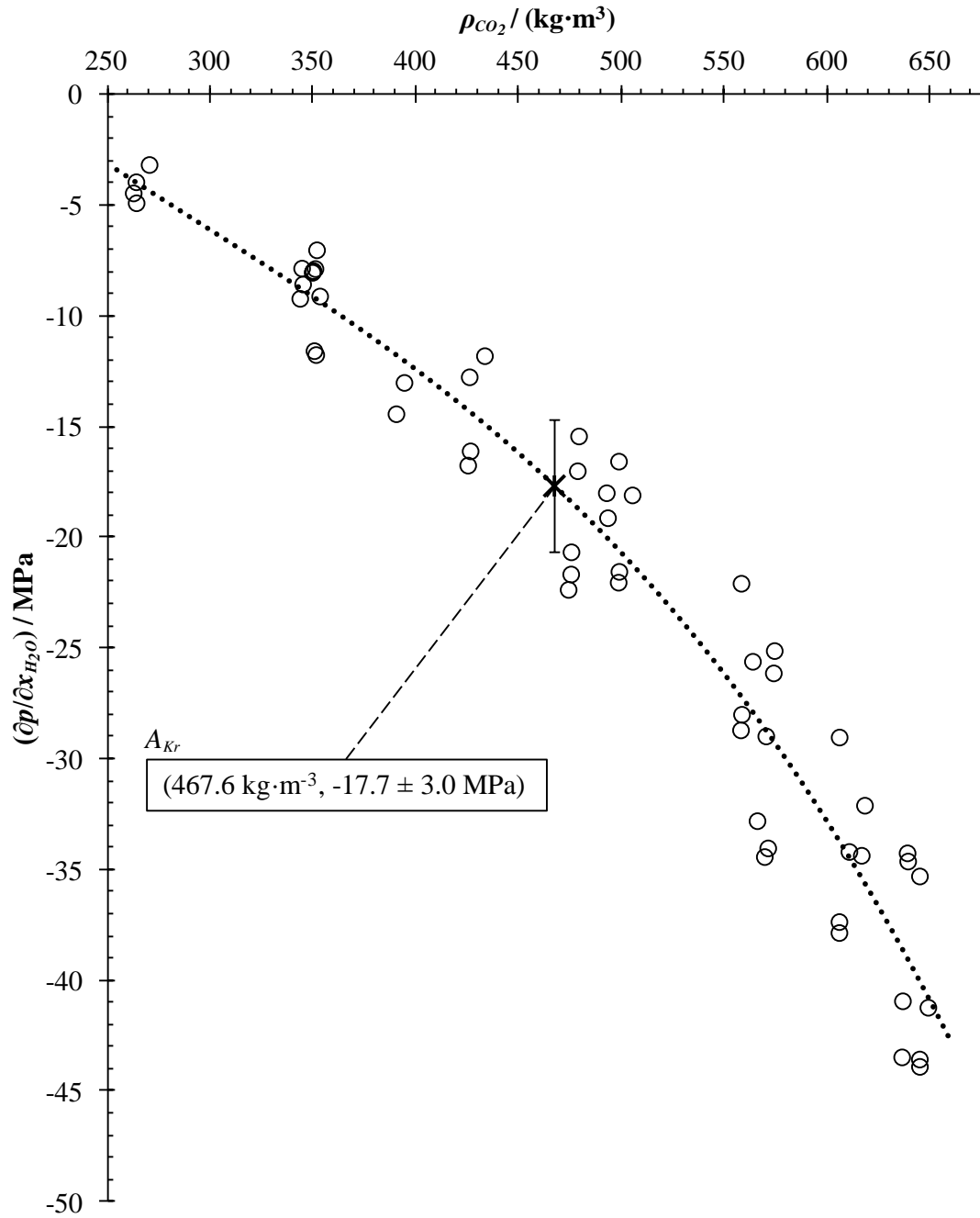


Figure 34. Plot of the $(\partial p / \partial x_{H_2O})$ derivatives against their corresponding pure CO_2 densities near the critical density to determine the Krichevskii parameter. Dotted line represents the cubic equation fit to the data where the Krichevskii parameter is its value at the critical density of CO_2 ($467.6 \text{ kg}\cdot\text{m}^{-3}$, $-17.7 \pm 3.0 \text{ MPa}$).

Both the Krichevskii parameter and the standard error obtained for H₂O dissolved in CO₂, are reasonable when compared to other solutes reported in the literature (see Table 10).⁶⁰ Abdulagatov *et al.* had previously estimated the Krichevskii parameter for H₂O in CO₂ to be $A_{Kr} = 471.7$ MPa by using the initial slopes of critical lines technique;^{59,60} however, this value does not match previously studied solutes in CO₂.⁶⁰ Not only is the value much larger than the other solutes, but larger positive values of A_{Kr} tend to indicate smaller, non-polar molecules. The calculation method used by Abdulagatov *et al.* is known to give larger errors in comparison to other methods of calculation,⁵⁶ and the authors note that some of the data sets they used were not in good enough agreement to give an accurate estimate of the A_{Kr} .⁵⁹ A Krichevskii parameter of -17.7 MPa is much more reasonable, particularly when compared to the A_{Kr} 's of the alcohol series listed in Table 10.

Looking at equation 4-10, a negative value should be expected for the Krichevskii parameter caused by mixing H₂O into CO₂ as the sign of A_{Kr} is controlled by the behaviour of the solute's partial molar volume in the critical region.⁶⁰ Both the isothermal compressibility and the molar volume of pure solvent are positive quantities, and with \bar{V}_2 experiencing sharp negative deviations in the near-critical region, $\bar{V}_2 - \bar{V}_1^*$ will also be negative making for $A_{Kr} < 0$.

Table 10. Comparison of Krichevskii parameters for several solutes dissolved in CO₂.⁶⁰ Superscript “a” denotes value calculated in this work.

Solute	$\frac{A_{Kr}}{\text{MPa}}$
1,1,1,2-Tetrafluroethane	-19.53
Water	-17.7 ^a
Butane	-15.55
Butanol	-15.34
Propanol	-15.12
Ethanol	-11.07
Difluoromethane	-9.2
Methanol	-6.4
Propane	-5.04
Fluoromethane	-2.499
Krypton	1.47
Nitrous Oxide	3.7
Ethane	4.31
Argon	19.27
Methane	22.21
Neon	29

Chapter Five: Conclusions and Future Directions

The design, construction and calibration of a vibrating tube densimeter was completed for obtaining volumetric measurements of acid gas fluids. A good measurement sensitivity was maintained for the densimeter while keeping the volume inside the vibrating tube to a minimum for safety considerations ($1.77 \pm 0.05 \text{ cm}^3$). The optically coupled feedback loop for detection of motion and conversion into a drive signal provides stable and accurate signal. Housing the vibrating tube inside an evacuated chamber also was found to enhance the measurement stability, allowing for density measurement errors down to $\delta\rho = \pm 0.01 \text{ kg}\cdot\text{m}^{-3}$ which is in general, an order of magnitude better than commercial vibrating tube densimeters. The pressure and temperature inside the densimeter can be controlled to better than $\delta p = \pm 0.005 \text{ MPa}$ and $\delta T = \pm 0.005 \text{ }^\circ\text{C}$ respectively.

Densities were obtained for CO_2 at temperatures between $T = 45$ to $120 \text{ }^\circ\text{C}$ and pressures up to $p = 35 \text{ MPa}$ and compared to the Span and Wagner equation-of-state,⁸ calibrated using previously measured literature values, through relative deviation plots (see Figure 27). The data obtained in this work was found to be in good agreement with the calculated values across all experimental conditions. The calculated errors for the density measurements were predictably larger in the near-critical region due to a larger change in density caused by deviations in the pressure and temperature measurement and also at higher pressures due to the nature of the pressure calibration. The agreement of repeated density measurements confirmed that the densimeter is stable over long periods of time using the procedures outlined in this work.

Densities were measured for H₂O dissolved in CO₂ at low concentrations and at the same experimental conditions as the pure CO₂ measurements. Using the mixtures' density difference from the pure solvent, the partial molar volumes of H₂O were calculated, assuming infinite dilution. This assumption was valid as partial molar volumes carried out using different water concentrations were not significantly different at similar temperatures and pressures. At lower temperatures, water's partial molar volume experienced an inflection as the critical pressure of CO₂ was approached.

The partial molar volumes were then used in determining the Krichevskii parameter ($A_{Kr} = -17.7 \pm 3.0$ MPa) for water's influence on the critical pressure of CO₂. This value did not agree with a previously reported literature value (471 MPa);⁶⁰ however, the A_{Kr} reported in this work is more consistent with the values and A_{Kr} trends, in both polarity and molecular size, of other solutes dissolved in CO₂.

The extension of this work to measuring other acid gas mixtures can be immediately undertaken after the addition of a N₂ or air purge towards the inlet of the instrument and caustic traps at the outlet in order to safely trap acid gas fluid species such as H₂S and COS for proper disposal. The volumetric properties of CO₂ mixtures with H₂S and COS solutes can be studied and together with liquid H₂S solvents containing CO₂, H₂O and COS solutes. These data will augment limited or non-existent data available in literature. Densities for COS-CO₂ mixtures have already been measured but were not included in this work due to time constraints.

The measurement of apparent molar heat capacities to give the temperature dependence of important thermodynamic properties could then be combined with the already determined pressure dependence from volumetric measurements to give a complete description of wet acid gas behaviour over the broad range of conditions and compositions. The potential would then exist for calibrating equation-of-states, specific to acid gas fluids, over a wide range of temperatures, pressures and compositions. Accurate thermodynamic prediction tools would be of particular interest to the natural gas processing industry in producing sour gas reserves when it comes to the transportation, conditioning or re-injection of an acid gas.

Some adjustments may be desired for future works with the vibrating tube densimeter. In the densimeter's current configuration, the PRT's are measuring the temperature against the surface of the vacuum cross housing the measurement cell. If the PRT's can be sealed inside the evacuated chamber, immediately next to the measurement cell, a more accurate temperature can be obtained.

The vibrating tube densimeter could be further automated through the addition of an air-actuated solenoid valve to the outlet of the instrument. After initially loading the sample into the densimeter, the valve could automatically release the pressure within the system to desired pressure set-points, so manual measurements would no longer be needed (as described in sub-section 3.4), saving the operator time. The valve would need to operate such that very small amounts of fluid are periodically released, so the drop in pressure is not too large for incompressible fluids (such as H₂O or dense-phase CO₂).

Appendix A: H₂S Synthesis

As discussed in chapter one of this thesis, H₂S is a major component of acid gas fluids and will likely be a part of future volumetric studies with the vibrating tube densimeter. In order to experimentally measure the thermodynamic properties accurately, all chemical species used should be of the highest purity. The purest, commercially available source of H₂S is listed at < 99.6%;⁶¹ however, the types of impurities present must also be considered.

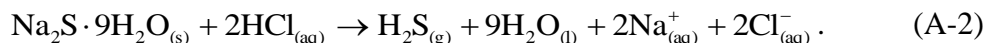
Analysis of the commercial gas through gas chromatography (GC) using a thermal conductivity detector (TCD) showed impurities of N₂, methane (CH₄), CO₂, and COS. The CO₂ and COS contaminants in the H₂S are particularly problematic when it comes to preparing mixtures of acid gas fluids due to the disturbance of the COS hydrolysis equilibrium:



When CO₂, H₂O, or COS are introduced to the H₂S, the concentration of the introduced species will then decrease by Le Châtelier's principle. Now the composition of the mixture is no longer known accurately and will cause problems when reporting any measured thermodynamic properties. Therefore, it is important that the H₂S used be of high-purity, and more specifically, with a minimum amount of contamination from the other species participating in the COS hydrolysis equilibrium reaction (CO₂, COS, and H₂O).

Two options for obtaining a higher purity H₂S are: (i) additional purification of the commercial H₂S, or (ii) in-house synthesis of H₂S. Further purification of the commercial H₂S was investigated by passing the gas through various combinations of molecular sieves (alumina and zeolites 3A, 4A, and 13X) and by liquid phase chemical reactions (ethylene diamine in ethanol and potassium hydroxide in ethanol). However, investigations using these methods were unable to selectively remove the impurities from the H₂S by any observable amount and will not be discussed further.

In-house H₂S generation was accomplished through the reaction of a sulfide salt with an acid because the reaction could be carried out at ambient conditions without the addition of a catalyst. Sodium sulfide nonahydrate (Na₂S·9H₂O) was chosen as the source of sulfide for its availability in high purity and its low cost (< 98.0%, Anachemia Lot 211010). A five normal solution (NIST standardized, J.T. Baker Batch 35782) of degassed hydrochloric acid (HCl) was used because its concentration was low enough to limit the rate of H₂S generation per volume of acid added while also keeping the reaction's end volume entirely within the reaction basin (4.5 L). The H₂S generation reaction is then given by



The waste sodium and chloride counter-ions will remain in the aqueous solution to minimize contamination of the desired gaseous product and make for easy disposal following the reaction. It should be noted in equation A-2 that a large amount of water is released from the hydrated sulfide upon reaction (approximately 81 mL per every mole of acid reacted) which must be accounted for when determining the final liquid volume due

to the limited size of the reaction basin. Also, the amounts of reactants used must limit the volume of the produced $\text{H}_2\text{S}_{(l)}$ to less than the volume of the collection vessel or else the vessel's pressure tolerance may be exceeded upon heating to room temperature.

A simplified schematic of the reaction apparatus is shown in Figure 35. The desired amount of $\text{Na}_2\text{S}\cdot 9\text{H}_2\text{O}$ was placed into the reaction basin (see B in Figure 35) with a magnetic stir bar before the reaction apparatus was then evacuated overnight through opening valves V2 and V3. V3 was then closed and commercial H_2S (H) was then flushed into the apparatus (open V7) to a pressure of approximately 1 bar (14 psia) to avoid breaking the glass reaction basin. This evacuation and flushing was repeated five times to remove as much remaining trace air from the apparatus as possible with a final evacuation being performed at the end before closing off V3.

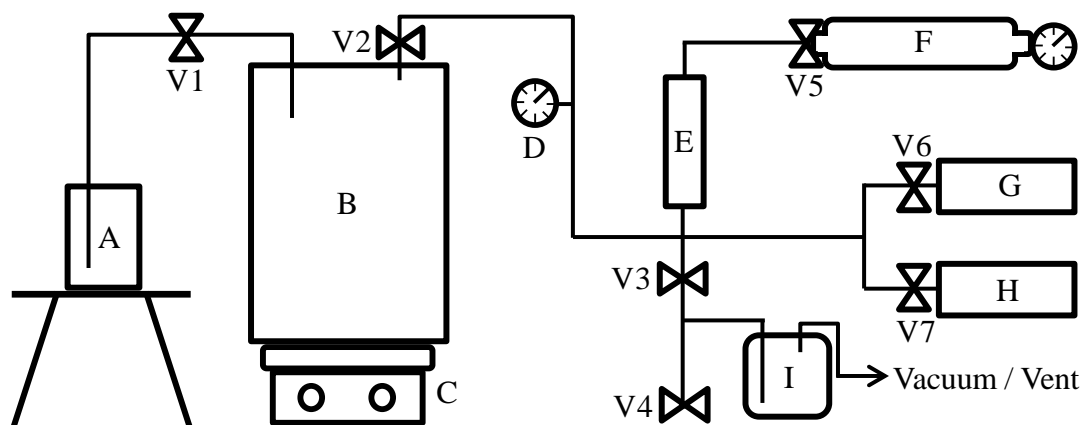


Figure 35. Simplified schematic of the reaction apparatus for the generation of H_2S : (A), 5N $\text{HCl}_{(aq)}$; (B), 4.5 L reaction basin containing $\text{Na}_2\text{S}\cdot 9\text{H}_2\text{O}$ and a magnetic stir-bar; (C), magnetic stir plate; (D), pressure gauge; (E), supported P_2O_5 dehydration column; (F), cooled H_2S collection vessel; (G), N_2 sweep gas; (H), H_2S purge gas; (I), series of caustic-scrubber and dry traps; (V#), valve.

The reaction was then initiated by introducing HCl through V1. This valve also provided flow-rate control over the acid and therefore, the reaction. Once the reaction had begun and some pressure had begun to build up in the apparatus, V5 was opened to allow gas condensation into the collection vessel being cooled using a combination of dry ice and liquid nitrogen. The H₂S was condensed within the vessel until the rate of gas evolution inside the basin visibly decreased, after which, V5 was closed and V3 was opened to vent any remaining H₂S in the apparatus into the caustic traps.

With V3 remaining open, acid was added until after gas evolution completely stopped to ensure the remaining aqueous solution was acidic to prevent further H₂S generation on disposal. V3 was then closed, and nitrogen (G) was swept through the apparatus at low-pressures (1.17 bar) to remove trace H₂S. Evacuation and nitrogen sweeping was repeated a total of five times to allow for safe opening of the apparatus for disposal of the remaining aqueous liquid.

A number of reaction rate controls are built-in to the apparatus besides V1 controlling the flow-rate of the acid. If pressure rises within the apparatus, the acid flow will automatically stop from the back-pressure; however, V1 must still be immediately closed if this occurs as H₂S will bubble back through the acid into the work space, posing a substantial safety risk. If V1 is closed, the pressure within the apparatus is reduced by the condensation of the H₂S in the cooled collection vessel. If needed, the H₂S vapour pressure can be decreased through a deeper cooling of the vessel *via* the addition of liquid nitrogen to the dry ice. Deeper cooling can also be used to increase the reaction rate while

V1 is open as a smaller pressure within the apparatus will pull the acid through at a faster rate.

As shown in Figure 36, the synthesized H₂S was purer overall than the commercial H₂S through analysis using GC-TCD with the concentrations of the impurities being given in Table 11. To further improve on the synthesized H₂S, it was passed through a bed of zeolite UOP 3A.

A water peak was not observed in the chromatogram for either the commercial or synthesized H₂S as it was easily removed through a phosphorus pentoxide (P₂O₅) dehydration.

The N₂ impurity was not significantly different between the samples tested and may be a result of the gas sampling technique.

CH₄ was not detected in the synthesized gas however it was present in the commercial gas suggesting that the H₂S was produced through reaction of sulfur and methane.⁶² Considering the combined CO₂ + COS content due to the equilibrium given in equation A-1, the synthesized H₂S had significantly less total carbon impurity. If the CH₄ being used in producing the commercial H₂S was a sales gas, there would have been small amounts of CO₂ present, leading to the larger carbon impurities that were observed in the GC analysis.

Although there was some carbon impurity in the synthesized H₂S, it was found that passing the gas through a bed of zeolite UOP 3A before sampling significantly reduced the CO₂ content, to give the most pure H₂S tested (99.95%). The effect of contact time between the gas and the zeolite may be worthwhile to study as CO₂ is the largest impurity present in the synthesized H₂S and longer contact times could potentially reduce the CO₂ even further.

Although the synthesized H₂S was not used in this work, it was used in the experimental determination of methane's hydrate phase equilibria in the presence of H₂S⁶³ and will be used in future volumetric studies with the vibrating tube densimeter.

Table 11. Concentrations of the impurities in the synthesized H₂S and commercial H₂S as measured by GC-TCD with their respective errors listed at 95% confidence.

Gas	Commercial H ₂ S (> 99.6%)	Synthesized H ₂ S	Synthesized + UOP 3A
% N ₂	0.0083 ± 0.0142	0.0142 ± 0.0055	0.0112 ± 0.0065
% CH ₄	0.0061 ± 0.0024	Undetected	Undetected
% CO ₂	0.0032 ± 0.0009	0.0999 ± 0.0059	0.0382 ± 0.0059
% COS	0.1897 ± 0.0135	Undetected	Undetected
% Total Impurity	0.2073 ± 0.0198	0.1140 ± 0.0081	0.0495 ± 0.0088

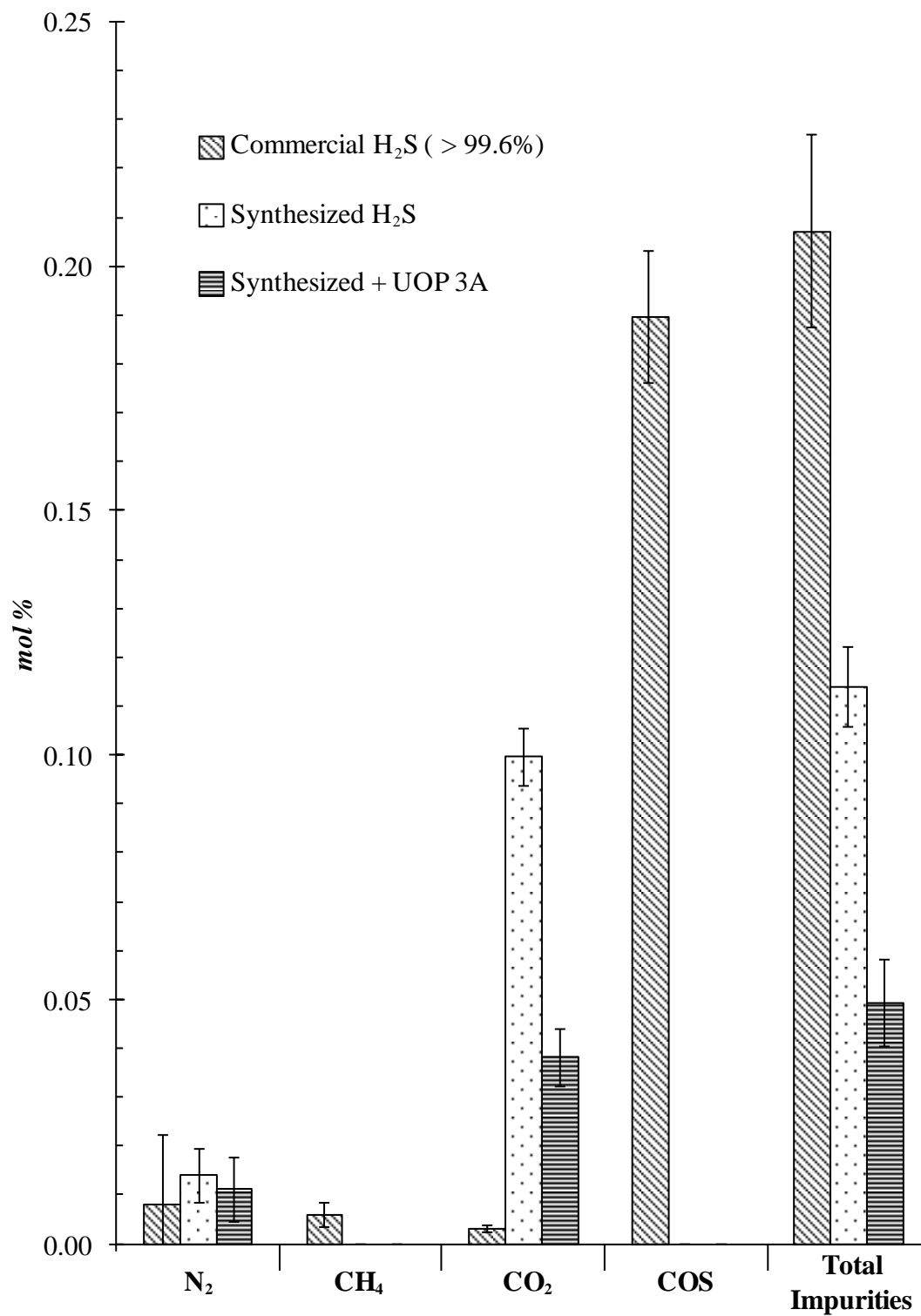


Figure 36. Comparison of contaminants in the synthesized H₂S and the commercial H₂S with their respective 95% confidence intervals as measured by GC-TCD.

References

1. International Energy Agency. *World Energy Outlook 2014*; OECD/IEA: Paris, France, 2014.
2. Gas Quality Specifications. TransCanada Pipelines. <http://transcanada.com/customerexpress/index.html> (accessed June 3, 2014).
3. Clark, P.D.; Davis, P.M.; Dowling, N.I.; Marriott, R.A.; Madekufamba, M.; Kirk, A.; Bhella, S. Claus Plant Chemistry and Technology. *ASRL Course: The Chemistry and Technology of Sour Gas Production and Processing, Sulfur Handling and Storage Options*. December 11-12, **2012**.
4. Taylor, K.M., Nichols, J.L., Johnson, J.E. *Acid Gas Disposal Options in an Emerging CO₂ Market*. 59th Laurance Reid Gas Conditioning Conference. Norman, OK, United States of America, February 22-25, **2009**.
5. Bachu, S. and Gunter, W.D. Acid gas injection in the Alberta basin, Canada: a CO₂-storage experience. *Geological Storage of Carbon Dioxide*. Geological Society of London; London, Special Publications. **2004**, 233, 225-234.
6. Digital Datasets. Alberta Geological Survey. <http://ags.gov.ab.ca/publications.aspx?series=dig> (accessed May 15, 2014).
7. Public Information Zone. BC Oil and Gas Commission. <http://bcogc.ca/public-zone> (accessed May 15, 2014).
8. Span, R. and Wagner, W. A New Equation of State for Carbon Dioxide Covering the Fluid Region from the Triple-Point Temperature to 1100 K at Pressures up to 800 MPa. *J. Phys. Chem. Ref. Data*. **1996**, 25, 1509-1596.
9. Lemmon, E.W. and Span, R. Short Fundamental Equations of State for 20 Industrial Fluids. *J. Chem. Eng. Data*. **2006**, 51, 785-850.
10. Ohsumi, T.; Nakashiki, N.; Shitashima, K.; Hirama, K. Density Change of Water Due to Dissolution of Carbon Dioxide and Near-Field Behavior of CO₂ from a Source on Deep-Sea Floor. *Energy Convers. Mgmt*. **1992**, 33, 5-8.
11. Song, Y.; Nishio, M.; Chen, B.; Someya, S.; Ohsumi, T. Measurement on CO₂ solution density by optical technology. *J. Vis*. **2003**, 6, 41-51.
12. Parkinson, W.J. and De Nevers, N. Partial molal volume of carbon dioxide in water solutions. *Ind. Eng. Chem. Fundam*. **1969**, 8, 709-713.

13. Zawisza, A. and Malesińska, B. Solubility of carbon dioxide in liquid water and of water in gaseous carbon dioxide in the range 0.2-5 MPa and at temperatures up to 473 K. *J. Chem. Eng. Data.* **1981**, 26, 388-391.
14. Zhang, J.; Zhang, X.; Buxing, H.; He, J.; Liu, Z.; Yang, G. Study on intermolecular interactions in supercritical fluids by partial molar volume and isothermal compressibility. *J. of Supercritical Fluids.* **2002**, 22, 15-19.
15. Stouffer, C.E.; Kllerman, S.J.; Hall, K.R.; Holste, J.C.; Gammon, B.E.; Marsh, K.N. Densities of carbon dioxide + hydrogen sulfide mixtures from 220 K to 450 K at Pressures up to 25 MPa. *J. Chem. Eng. Data.* **2001**, 46, 1309-1318.
16. Nighswander, J.A.; Kalogerakis, N.; Mehrotra, A.K. Solubilities of Carbon Dioxide in Water and 1 wt % NaCl Solution at Pressures up to 10 MPa and Temperatures from 80 to 200 °C. *J. Chem. Eng. Data.* **1989**, 34, 355-360.
17. Crovetto R.; Wood, R.H.; Majer V. Revised densities of $\{x\text{CO}_2+(1-x)\text{H}_2\text{O}\}$ with $x<0.014$ at supercritical conditions. Molar volumes, partial molar volumes of CO_2 at infinite dilution, and excess molar volumes. *J. Chem. Thermodynamics.* **1991**, 23, 1139-1146.
18. King, M.B.; Mubarak, A.; Kim, J.D.; Bott, T.R. The Mutual Solubilities of Water with Supercritical and Liquid Carbon Dioxide. *J. of Supercritical Fluids.* **1992**, 5, 296-302.
19. Hnědkovský, L; Wood. R.H.; Majer, V. Volumes of aqueous solutions of CH_4 , CO_2 , H_2S , and NH_3 at temperatures from 298.15 K to 705 K and pressures up to 35 MPa. *J. Chem. Thermodynamics.* **1996**, 28, 125-142.
20. Fenghour, A.; Wakeham, W.A. Densities of (water+carbon dioxide) in the temperature range 415 K to 700 K and pressures up to 35 MPa. *J. Chem. Thermodynamics,* **1996**, 28, 433-446.
21. Teng, H.; Yamasaki, A.; Chun, M.K.; Lee,H. Solubility of liquid CO_2 in water at temperatures from 278 K to 293 K and pressures from 6.44 MPa to 29.49 MPa and densities of the corresponding aqueous solutions. *J. Chem. Thermodynamics.* **1997**, 29, 1301-1310.
22. Li, Z.; Dong, M.; Shuliang, L.; Dai, L. Densities and solubilities for binary systems of $\text{CO}_2+\text{H}_2\text{O}$ and CO_2+brine at 59 °C and pressures up to 29 MPa. *J. Chem. Eng. Data.* **2004**, 49, 1026-1031.
23. Hebach, A.; Oberhof, A.; Dahmen, N. Density of Water+Carbon Dioxide at Elevated Pressures: Measurements and Correlation. *J. Chem. Eng. Data.* **2004**, 49, 950-953.

24. Song Y.; Jian, W.; Zhang, Y.; Yang, M.; Zhao, J.; Liu, Y.; Shen, Y. Density Measurement and PC-SAFT/tPC-PSAFT Modeling of the CO₂+H₂O System over a Wide Temperature Range. *J. Chem. Eng. Data.* **2014**, 59, 1400-1410.
25. Seitz, J.C. and Blencoe, J.G. The CO₂-H₂O system. I. Experimental determination of volumetric properties at 400 °C, 10-100 MPa. *Geochim. Cosmochim. Acta.* **1999**, 63, 1559-1569.
26. Wagner, W. and Kleinrahm, R. Densimeters for very accurate density measurements of fluids over large ranges of temperature, pressure and density. *Metrologia.* **2004**, 41, S24-S39.
27. Kratky, O.; Leopold, H.; Stabinger, H. Dichtemessungen an Flüssigkeiten und Gasen auf 10⁻⁶ g/cm³ bei 0.6 cm³ Präparatvolumen. *Z. angew. Phys.* **1969**, 27, 273-277.
28. Picker, P.; Tremblay, E.; Jolicoeur, C. A High-Precision Digital Readout Flow Densimeter for Liquids. *J. Solution Chem.* **1974**, 3, 377-384.
29. Hynek, V.; Hnědkovský, L.; Cibulka, I. A new design of a vibrating-tube densimeter and partial molar volumes of phenol(aq) at temperatures from 298 K to 573 K. *J. Chem. Thermodynamics.* **1997**, 29, 1237-1252.
30. Majer, V.; Crovetto, R.; Wood, R.H. A new version of vibrating-tube flow densitometer for measurements at temperatures up to 730 K. *J. Chem. Thermodynamics.* **1991**, 23, 333-344.
31. Blencoe, J.G.; Drummond, S.E.; Seitz, J.C.; Nesbitt, B.E. A Vibrating-Tube Densimeter for Fluids at High Pressures and Temperatures. *Int. J. Thermophys.* **1996**, 17, 179-190.
32. May, E.F.; Tay, W.J.; Nania, M.; Aleji, A.; Al-Ghafri, S.; Trusler, J.P.M. Physical apparatus parameters and model for vibrating tube densimeters at pressures to 140 MPa and temperatures to 473 K. *Rev. Sci. Instrum.* **2014**, 85, 095111/1-095111/12.
33. Swagelok. Tubing and Tube Accessories.
[http:// http://swagelok.com/products/tubing-tube-accessories.aspx](http://http://swagelok.com/products/tubing-tube-accessories.aspx) (accessed September 23, 2014).
34. Clifford, C. A. and Seah, M. P. Quantification issues in the identification of nanoscale regions of homopolymers using modulus measurement via AFM nanoindentation. *Nanotechnology.* **2005**, 16, 1666-1680.
35. Finot, E., Passian, A., and Thundat, T. Measurement of Mechanical Properties of Cantilever Shaped Materials. *Sensors.* **2008**, 8, 3947-3541.

36. Wagner, W. and Pruß, A. The IAPWS Formulation 1995 for the Thermodynamic Properties of Ordinary Water Substance for General and Scientific Use. *J. Phys. Chem. Ref. Data.* **2002**, 31, 387-535.
37. Ortiz-Vega, D.O.; Hall, K.R.; Arp, V.D.; Lemmon, E.W. Helmholtz equation (intern equation) of state for helium. To be published in *Int. J. Thermophys.* **2010**.
38. NIST Standard Reference Database 23: Reference Fluid Thermodynamic and Transport Properties (REFPROP), Version 9.1. National Institute of Standards and Technology, Standard Reference Data Program: Gaithersburg, MD, 2010.
39. U.S. Department of Energy. Using Light-Emitting Diodes: Measuring Light Source Life. https://web.archive.org/web/20090410171009/http://www1.eere.energy.gov/buildings/ssl/life_measuring.html (accessed November 19, 2012).
40. Serway, R.A., Jewett, J.W. *Physics for Scientists and Engineers*, 3rd ed.; Brooks/Cole: Belmont, 2004.
41. Preston-Thomas, H. The International Temperature Scale of 1990 (ITS-90). *Metrologia.* **1990**, 27, 3-10.
42. Bedford, R.E.; Bonnier, G.; Maas, H.; Pavese, F. Recommended values of temperature on the International Temperature Scale of 1990 for a selected set of secondary reference points. *Metrologia.* **1990**, 33, 133-154.
43. Tilford, C.R. Pressure and Vacuum Measurements. In *Physical Methods of Chemistry*; Rossiter, B.W., Baetzold, R.C., Eds.; John Wiley & Sons, Inc. Vol. 6; pp 101-173.
44. Pressurements Limited, User Manual for T3800 Deadweight Tester.
45. Miks, C.E.; Linton, L.H.; Wilson, G. Deadweight Gauge. US 3272014, September 13, 1966.
46. Hynek, V.; Hnědkovský, L; Cibulka, I. A new design of a vibrating-tube densimeter and partial molar volumes of phenol(aq) at temperatures from 298 K to 573 K. *J. Chem. Thermodynamics.* **1997**, 29, 1237-1252.
47. Aida, T.; Yamazaki, A.; Akutsu, M.; Ono, T.; Kanno, A.; Hoshina, T.; Ota, M.; Watanabe, M.; Sato, Y.; Smith Jr., R.L.; Inomata, H. Laser-Doppler vibrating tube densimeter for measurements at high temperatures and pressures. *Rev. Sci. Instrum.* **2007**, 78, 115111/1-115111/3.

48. Hakin, A.W.; Daisley, D.C.; Delgado, L.; Liu, J.L.; Marriott, R.A.; Marty, J.L.; Tompkins, G. Volumetric properties of glycine in water at elevated temperatures and pressures measured with a new optically driven vibrating-tube densimeter. *J. Chem. Thermodynamics*. **1998**, 30, 583-606.
49. Span, R.; Lemmon, E.W.; Jacobsen, R.T.; Wagner, W.; Yokozeki, A. A Reference Equation of State for the Thermodynamic Properties of Nitrogen for Temperatures from 63.151 to 1000 K and Pressures to 2200 MPa. *J. Phys. Chem. Ref. Data*. **2000**, 29, 1361-1433.
50. Sanmamed, Y.A.; Dopazo-Paz, A.; González-Salgado, D.; Troncoso, J.; Romani, L. An accurate calibration method for high pressure vibrating tube densimeters in the density interval (700 to 1600) kg·m⁻³. *J. Chem. Thermodynamics*. **2009**, 41, 1060-1068.
51. Lampreia, I.M.S and de Castro, C.A.N. A new and reliable calibration method for vibrating tube densimeters over wide ranges of temperature and pressure. *J. Chem. Thermodynamics*. **2011**, 43, 537-546.
52. Density Meter. Anton Paar. <http://anton-paar.com/ca> (accessed September 15, 2014).
53. Kunz, O.; Klimeck, R.; Wagner, W.; Manfred, J. The GERG-2004 Wide-Range Equation of State for Natural Gases and Other Mixtures. *GERG Technical Monograph 15*. Fortschr.-Ber. VDI, VDI-Verlag, Düsseldorf, 2007.
54. Furuya, F. and Teja, A.S. Krichevskii Parameters and the Solubility of Heavy n-Alkanes in Supercritical Carbon Dioxide. *Ind. Eng. Chem. Res.* **2000**, 39, 4828-4830.
55. Plyasunov, A.V. Values of the Krichevskii Parameter, A_{KR} , of Aqueous Nonelectrolytes Evaluated from Relevant Experimental Data. *J. Phys. Chem. Ref. Data*. **2012**. 41, 033104-1-033104-30.
56. Plyasunov, A.V. and Shock, E.L. Estimation of the Krichevskii parameter for aqueous nonelectrolytes. *J. of Supercritical Fluids*. **2001**. 20, 91-103.
57. Anderson, G.M. and Crerar, D.A. *Thermodynamics in Geochemistry: The Equilibrium Model*. Oxford University Press: New York, 1993.
58. AQUAlibrium, Version 3.0. FlowPhase Software Inc: Calgary, AB, 2004.
59. Abdulagatov, A.I., Stepanov, G.V., Abdulagatov, I.M. The Critical Properties of Binary Mixtures Containing Carbon Dioxide: Experimental Data. *High Temperature*. **2007**. 45, 85-126.

60. Abdulagatov, A.I., Stepanov, G.V., Abdulagatov, I.M. The Critical Properties of Binary Mixtures Containing Carbon Dioxide: Krichevskii Parameter and Related Thermodynamic Properties. *High Temperature*. **2007**. 45, 408-424.
61. Specialty Gases and Equipment. Praxair Direct: Praxair Inc.
<http://catalogs.praxairdirect.com/issue/25778> (accessed June 14, 2012)
62. de Simó, M. Production of Carbon Disulphide. US2187393, January 16, 1940.
63. Ward, Z.T.; Deering, C.E.; Marriott, R.A.; Sum, A.K.; Sloan, D.; Koh, C.A. Phase Equilibrium Data and Model Comparisons for H₂S Hydrates. *J. Chem. Eng. Data*. [Online early access]. DOI: 10.1021/je500657f. Published Online: Sept 19, 2014.
<http://pubs.acs.org/doi/full/10.1021/je500657f> (accessed September 22, 2014).